Investigation of Metallic Foams for Aero-Engine Sealing

Allan Yu Liu

Department of Mechanical Engineering

University of Sheffield

This dissertation is submitted for the degree of

Doctor of Philosophy

June 2024

Acknowledgements

I would like to thank Rolls-Royce for funding this doctoral study and providing me with the opportunity to work on this research project. I would in particular like to acknowledge the help and guidance of Glen Pattinson, Lloyd Pallet, Matthew Hancock and Dan Everington for their expertise and knowledge contributed to this research.

I am indebted to my supervisor Matthew Marshall who has taken me on to participate in this research project. I have thoroughly enjoyed the research and all the guidance and contributions that he has made, this research could not have been achieved without his constant support and guidance.

Additionally I would like to thank my friends and colleagues Eldar and Aaron for making my time during my PhD more pleasurable, working in collaboration with them has been a great pleasure and hope to stay in contact throughout the years to come.

My good friends John, Klau, Anya and Alex who have supported me throughout this process through all the good and bad times, I have been able to count on them when it really matters which has pushed me to complete this piece of work to the best of my ability.

I would also like to dedicate this thesis to my parents and family Changqing Liu, Qiuxiang Bi, Ben Liu and Grace Liu, as without their full support this could not have happened. I would like to appreciate their full encouragement and comfort whenever I have needed it throughout my studies. Without them this thesis could not have been completed and I have been so lucky to have such a caring family in my life.

Last but not least I would like to appreciate my girlfriend Sopita Ngarmskullert who has helped me in my stressful times showing her constant support. I have been so lucky to have you in my life showing your full encouragement which has meant so much to me.

Abstract

Aero-engine sealing is a large concern using current material solutions for providing longer service life and better performance. For even optimum conditions current materials have inconsistencies in performance. A new novel set of materials is proposed to provide consistencies in performance and to accommodate for any spontaneous scenarios which occur such as harsh manoeuvres or environmental conditions.

Metallic foams were thought to have suitable mechanical and thermal properties for abradable linings. This report outlines the methodologies of how metallic foams were tested as well as an outline of how metallic foams behaved under certain loading conditions. Alantum foam is industrially available and comprised of a Nickel-Chromium (NiCr) alloy. The effects of filler material within the open cellular structure is also evaluated to understand the effects on the wear mechanisms and material behaviours. Additionally, as thermal limitations arise conventional thermal abradable material in combination with metallic foams is tested to investigate material compliance to understand whether sealing can be achieved.

These tests were achieved through use of the low-speed rig available at the University of Sheffield. This set-up includes front-on stroboscopic imaging of the blade and the abradable sample, the stroboscopic imaging for the blade helps to identify the material transfer, adhesion and damage during the test. The stroboscopic imaging allows for digital image correlation (DIC) post processing to identify areas of weakness, stress and strain accumulation and the fracture mechanics. Vacuum impregnation techniques are adopted to assess and analyse internal structure without breaking any of the metal foam in the sectioning process.

This project focuses on the interaction of an Inconel 718 blade (Rotatory - 100m/s) with a metallic foam abradable (stationary), a consistent incursion rate of 2 μm/pass is used for a suitable comparison of the different wear behaviours for the impact of filler and effects of pore size in open cellular structures. Furthermore, with consistent filler material different incursion rates of 2, 0.2 and 0.02 μm/pass are tested to identify the impact filler has on the wear mechanisms and behaviours during interaction with the blade. Thermal ageing of the samples is carried out to investigate the thermal capabilities. For capped metal foam substrates failure is evident at the lower incursion rates and so incursion rate is used as a cut off criteria where tests are not carried out at the lower incursion rates if they failed at the faster incursion events.

Filled foams rub tests established that filler density and thermally aged samples have a big impact on the rub tests where increases in filler density showed positive results. However, with increased thermal ageing temperatures of + 300 °C failures within the rub tests started to appear such as cracking and thermal smearing.

Finally for capped metallic foams factors such as cap hardness, pore size and incursion rates strongly determine the outcome of tests where softer caps and larger pore size combinations showed the best results at the fast incursion rate conditions. Additionally, patterned coatings have been tested and results have shown that cutting mechanisms are controlled and located along fault lines within the top surface pattern.

Contents

List of Figures

List of Tables

Chapter 1

Introduction

1.1 Aero-Engine Sealing

Aero-engines provide a propulsion force for aircraft which can allow them to fly at incredible speeds. Power is generated through the expansion of gas which is a result of the combustion reaction, which requires high-pressure air to mix with fuel for ignition. The compressor stage is responsible for providing sufficient compressed air to satisfy the requirements of combustion. The pressure of the mass of air from the inlet is increased and provided for combustion at the required pressure, another purpose it is commonly used for is to provide bleed air for various systems. Figure 1 shows a schematic of the separate stages within an aero-engine and where the compressor stages are located. There are two basic types of compressors, these are known as axial and centrifugal. Flow through a centrifugal compressor is turned perpendicular to the axis at which rotation occurs, however, air in an axial compressor flows parallel to the axis at which rotation occurs [1].

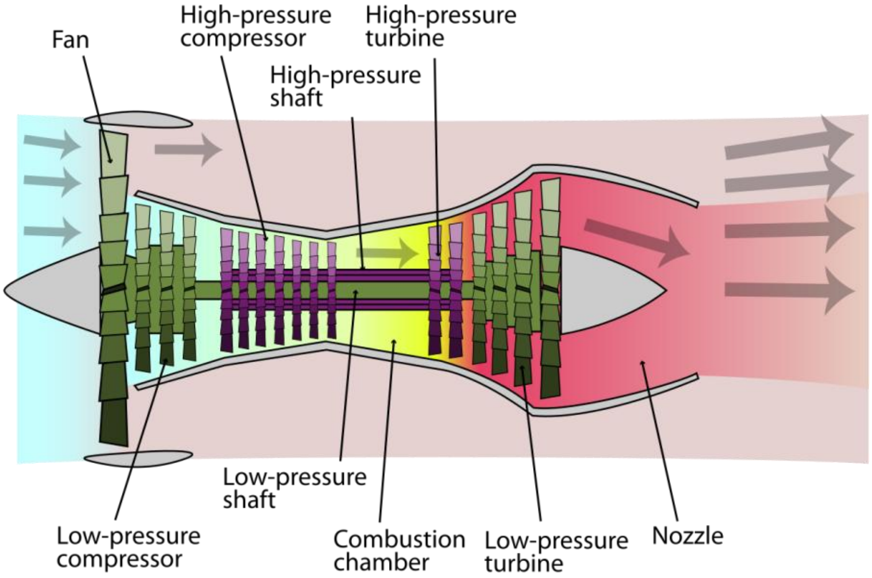

Figure 1. Aero-engine stages [2]

Aero-engine sealing is not only critical from an economic stand point, but is also important for the aircraft’s performance and efficiency. Sealing usually consists of an abradable layer which breaks down and wears away when in contact with the blade tips. Without the presence of this sealing liner, severe wear can occur between the blade and outer casing causing damage to both components. Damage to both components will limit the service life, furthermore debris or broken fragments can cause failures and further damage downstream limiting performance. Economically sealing can provide cost reductions due to prolonged service life and ultimately better performance saving a large amount of fuel costs.

Ideally compressor statics are concentric to the disc, where the static parts move radially in coherence with the rotating parts under all mechanical and thermal conditions which arise. To best reflect this behaviour, liners are also used to cope with the tip interactions that occur. A liner is cut by the blade to provide and maintain a suitable tip clearance for system operation. The role of the liner is to break down upon contact with the blade, if the blade is worn out by the liner this opens up the clearances around lightly rubbing and non-rubbing areas of the circumference [2].

1.2 Rolls- Royce Research

Rolls-Royce have been investigating suitable materials in the form of abradables to provide improved compressor lining, such materials must enable an axial compressor to perform more efficiently, effectively and reliably. Compressor sealing is very important to support the aerodynamic design, this ultimately influences the performance and operability of the gas turbine. Current systems up to 450°C for Ti aerofoils tend to be based on Al-Si alloys with secondary phase additives included. Systems for use up to 700°C for Ni aerofoils tend to be based on Ni-Cr-Al alloys with secondary phase additives [2][3][4][5].

1.3 Current Challenges

Current challenges include the formation of the wrong types of debris, this can cause damage to seals and blades (for example cracking or thermal damage) resulting in the sealing to open up and exhibit air leakage. Furthermore, due to the debris formation and generation when the abradable comes into contact with the blade, further on downstream this can cause blockages in the combustor. Turnaround time (TAT) for aircraft maintenance, repair and overhaul (MRO) services and inefficiencies in supply chain can be a major challenge. Time delays in MRO arise due to inefficiencies and waste in the process flow which can be as a result of breakdown and debris build up from abradable seals. Lowering the TAT could result in a much more improved framework and efficiency, resulting in longer service lifetime and cost-effectiveness [6]. Often some of the abradable seals are broken and tip blade material adhesion occurs, this can cause over cutting of the seal increasing the blade tip clearance and reducing overall efficiency of the system. Environmental conditions also require a limited variety of material properties to withstand various anticipated and sudden changes in loading conditions mechanically and thermally. Even when optimum conditions are achieved due to how abradables are manufactured they still have localities of material properties from the thermal spraying process, this means the above problems can still persist.

1.4 Aims and Objectives

This project aims to provide a novel approach to aero-engine sealing, proposing a new material structure and formation. Metallic foams have many suitable mechanical properties and thermal properties. Fundamentally due to how they are manufactured, there is also the opportunity to engineer these properties to produce homogenous materials. This means that when an optimised situation is reached it can be applied across all engines.

The main objectives are to understand and provide experimental and potential modelling work on how foams behave and what factors affect the performance under reproduced loading conditions. These novel materials need to be investigated to further understand how they breakdown and behave under a wide range of loading conditions which is a major milestone to this project. This project will investigate metallic foams with polymeric fillers as well as foams with Metco 320 applied to see if these combinations can make any improvements.

Further modifications can provide an optimised approach of how this family of materials can be implemented, to make use of the desired mechanical and thermal properties required for engine sealing of the compressor stage. Metallic foams in combination with current sealing techniques and materials could potentially prove to satisfy all the requirements that make a good engine seal.

1.5 Thesis Layout

Proceeding from this initial introduction Chapter, literature related to the scope of the project is presented in Chapter 2. This highlights the current issues and challenges that may occur in current flight operation assessing the conventional materials used as well as the new materials proposed to be tested in this thesis.

In order to assess and analyse how the new material performs, a testing procedure and methodology to study these abradable foam substrates is set in place and presented in Chapter 3. This outlines all the instrumentation and flexibility in testing which can be carried out as part of this doctoral thesis. Chapter 4 encompasses the data processing procedures after the raw data is collected.

In the first experimental chapter, Chapter 5, open-cell foam samples and filled foam samples are compared. Both types of samples are compared against their performance regarding compliance and blade and sample damage.

In continuation of the polymeric-filled foams tested in the previous chapter, Chapter 6 is focused on an in-depth analysis of how polymeric-filled foams perform under a range of loading conditions, studying the effects of filler density, tip speeds, incursion rate, and thermal ageing.

After highlighting the operable temperature limitations of polymeric-filled foams, Chapter 7 addresses a combination of Metco 320 and metallic foams as a capped metallic foam substrate.

Chapter 8 explores how to optimise the use of Metco 320 capped foams by creating patterns in the spraying process.

Chapter 9 highlights the conclusions of the work, with further work necessary to understand the ideal foam structure and properties for use in applications.

Chapter 2

Literature Review

A literature review has been constructed to identify and find gaps within current abradable research and materials, mainly focused on context and background around abradables and their functions within the engine. Identifying the research gap around currently traditionally used materials, testing methods and data on such materials will help when comparing against the results seen later on in the experimental Chapters.

Sealing performance is primarily the biggest problem within the compressor stages of the engine. The sealing performance of aero-engine air pathways heavily influence the efficiency and fuel consumption within the aircraft engine. Various research highlights the importance of sealing technology to improve the efficiency and reduce fuel consumption with one ultimate aim, to minimalize and reduce air leakage loss between rotating and stationary components. Abradables known as rub-tolerant materials are introduced to help minimize engine operating clearances to optimize efficiency through limiting gas leakage between engine stages [7].

Clearance control is of paramount importance to meet current day power output, efficiency and operational lifetime goals. Excessive clearances lead to a series of undesirable outcomes such as loss in efficiency, flow instabilities, and hot gas ingestion into disk cavities. However, insufficient clearances can cause limitation of coolant flow and heavy interfacial rubbing. This will overheat components downstream and damage other interfaces it comes into contact with, thus limiting the life of such components. Clearance control is a critical attention point to designers as it is often the most cost-effective method to enhance system performance and operation. Proper material selection continues to play an important role in being able to maintain interface clearance goals [8][9]–[11].

2.1 Sealing in Aero-Engines

2.1.1 Importance of Sealing

Abradable linings are positioned between the rotary and stationary components present within compressor casings, turbine casings and shaft seals. Seals control turbomachinery leakages, as well as coolant flows which contribute to overall system stability. Sealing coatings are sacrificial which give their structural integrity for the benefit of the component, these coatings are subject to abrasion, erosion, oxidation, incursive rubs, foreign object damage (FOD), material deposits and extreme thermal, mechanical and impact loading conditions [8]. The clearance between the blade tips and surrounding casing (shroud) tends to vary accordingly with respect to changes in mechanical and thermal loading conditions on the rotary and stationary structures [1]. Figure 2 clearly indicates the position of the abradable lining (outlined in blue) with respect to the turbine and outer casing, this is present for the compressor and turbine stages of an aero-engine.

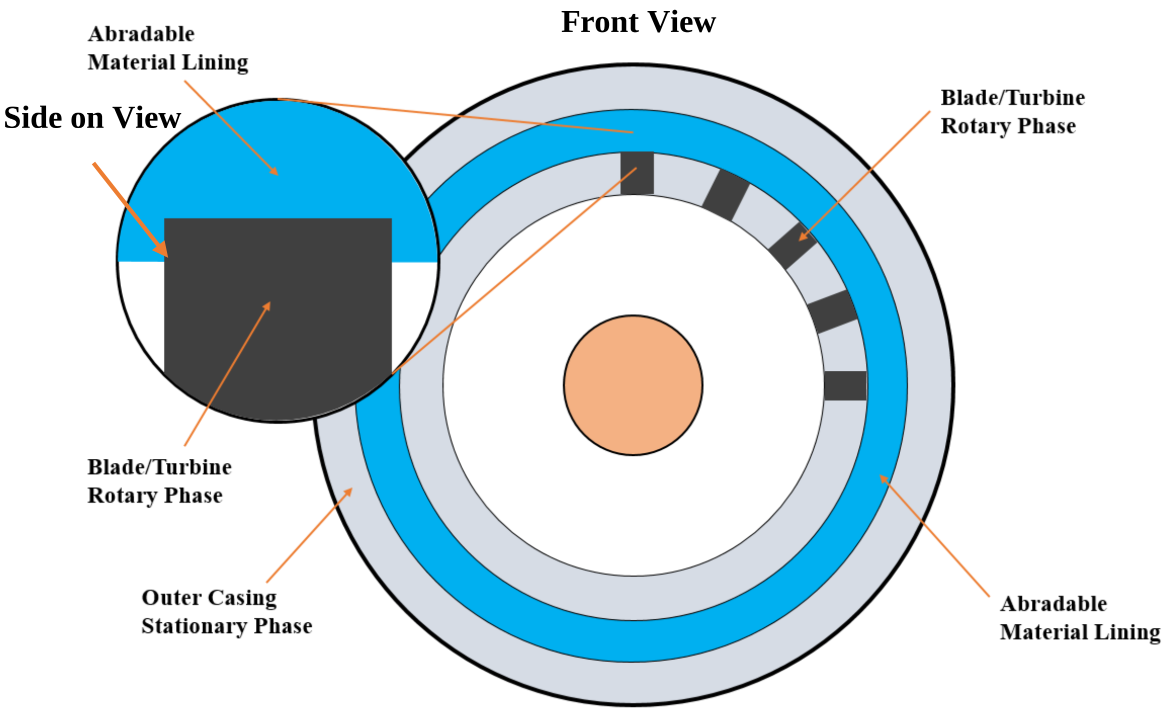

Figure 2. Engine compressor stage to show the location and position of the abradable lining

It is desired to have the blade sat within the abradable liner as shown in Figure 2, this is achieved by cutting and wear of the abradable material when in contact with the blade creating a seal between the two components.

2.1.2 Current Sealing Technologies

Initially there is clearance between the stationary and rotary phase, most of the rubbing of the abradable sacrificial layer happens during running and handling procedures which take place before engines are distributed to the customers. Blade rubs are expected to occur during the service life of the engine, these clearances are specifically chosen to achieve a certain amount of blade incursion for extreme conditions such as take-off and re-acceleration. This is critically important such that the tip seals will be honed to operate line-to-line under repeated conditions after the engine has been run-in. Rubs can also contribute towards accelerating the rates of erosion and thermal fatigue through wearing of the protective coatings [8].

Axisymmetric clearance changes are a result of uniform loading on the rotary and stationary components, this will generate a uniform radial displacement as shown in Figure 3. These clearance changes create a need for seals. Centrifugal and thermal loads are responsible for many of the largest radial variations that occur in tip clearance. Centrifugal loading conditions mainly cause axisymmetric clearance changes through expansion and contraction of the rotor during engine acceleration. Thermal loads produce both axisymmetric and asymmetric clearance changes between rotary and stationary structures. The thermal expansion and contraction of these structures and the uniformity of how they are heated and cooled will directly influence the homogeneity of the blade tip clearance. For large diameter bladed discs and corresponding shrouds the extreme variations within the rotational speeds along with temperature conditions create large displacements in the rotary and stationary structures [8][9], [12].

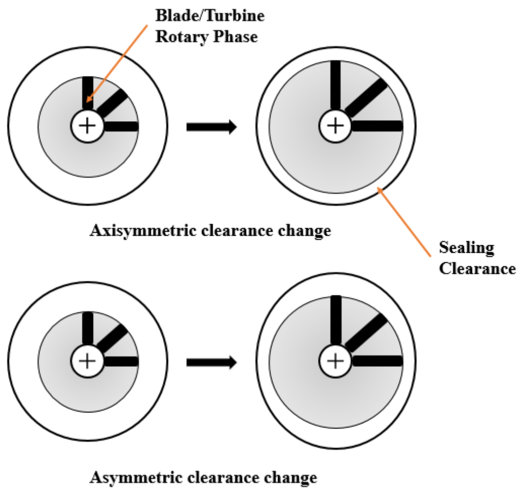

Figure 3. Schematic to show difference between axisymmetric and asymmetric clearance changes

Blade tip clearance should be able to accommodate the worst case scenario so that in any circumstance there will be no danger to the parts or reliability and performance. Figure 4 shows the tip clearance profile and speed as a function of time for axisymmetric loading conditions. As a cold engine is started it can be identified that a set amount of clearance already exists between the shroud and blade tip, the clearance is quickly diminished as the engine speed increases for take-off. This is a result of the centrifugal load and rapid heating the turbine blades experience, this causes radial expansion outwards. The case will also expand due to heating however this will be at a much slower rate in comparison to the blades, this phenomenon can create a minimum gap know as a "pinch point". As the case expands further due to heating, the clearance will start to increase until the rotor begins to heat up and close this clearance again.

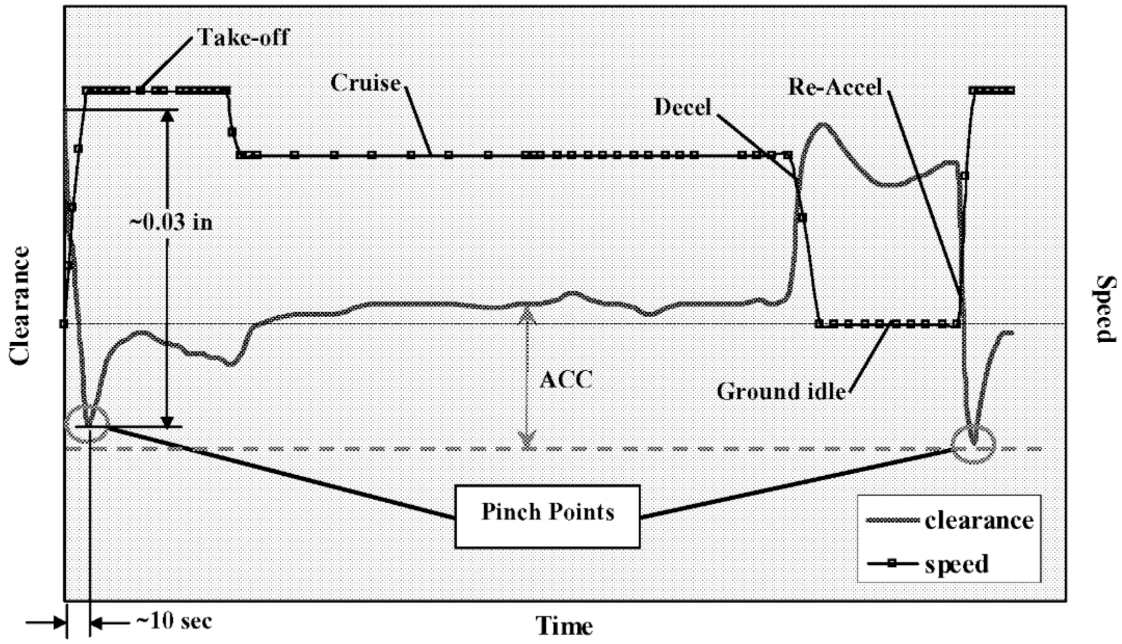

Figure 4. Clearance and speed profile as a function of time in the compressor stages of an engine [8]

When the engine approaches cruise condition the tip clearance remains reasonably constant as the rotor and case have both reached a state of thermal equilibrium. However, there are circumstances such as a step change in altitude which can change the tip clearance and must be accounted for when considering the damage if the blade starts to wear into the casing. During deceleration the clearance is quickly increased as the mechanical loading of the rotor and blades is released and the thermal lag of the case as it cools. Often a second pinch point can occur, this can be due to conditions such as an aborted landing or an evasive manoeuvre, this scenario is known as re-acceleration.

Two key concepts can be distinguished about clearance control within aero-engines. It is desirable to lower the operating clearance during cruise as this will result in the greatest reduction in fuel consumption and increase performance and efficiency. Furthermore, it would be desirable to open the clearance spacing during the pinch point conditions to avoid any potential rubs or wear of the blades with the outer casing. This is where abradables have been used to help improve efficiency and performance during both the cruise and pinch point conditions [8]. Figure 5 shows the significant differences that an abradable lining provides in the compressor stage of the aero-engine. At first the engine is running with stability and the clearance for both with and without an abradable lining is the same and constant. Due to unexpected events such as bending of the main shaft, rubbing interactions between the blades and the outer surface can occur. It can be clearly seen that the overall clearance gap opens up a lot without a lining compared to using a lining when this happens. Other consequences include damage and wear to both stationary and rotary components as well as a large loss in efficiency and performance [13].

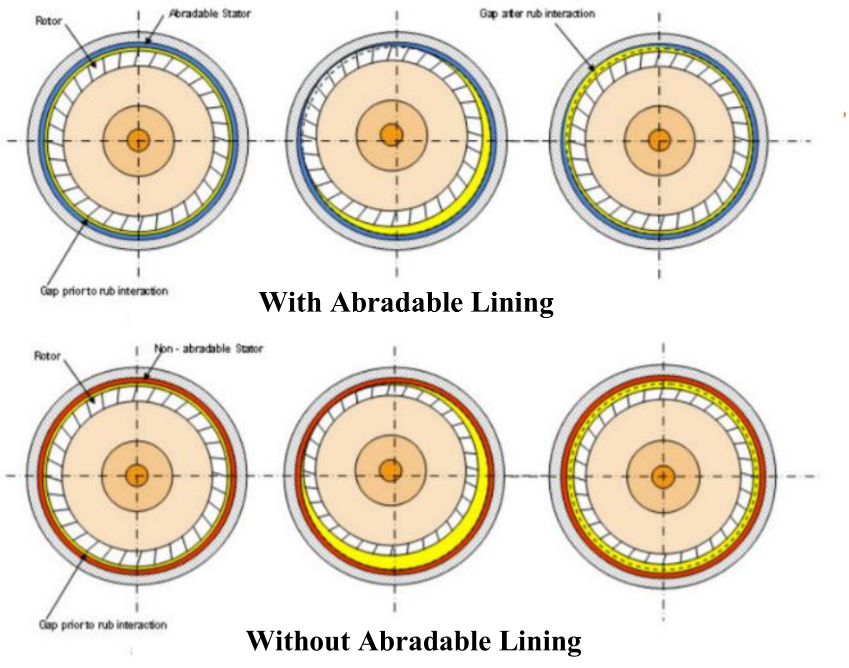

Figure 5. Evolution of rub interaction with and without presence of abradable seal [9]

Rolls Royce do not always manage to manufacture their engine casing concentric to the shape of the blade path, this in turn means tip clearance is a variable that creates a need for liners to be cut and sealing achieved on first use of the engine. This means that abradables must work in two scenarios, first use of the engine and in service as the engine deploys thermally. Before entering service all aero-engines go through pre-service pass-off also known as running-in and handling in factory. Even if round casings are not manufactured and a different shape is adopted, due to unexpected circumstances and harsh manoeuvres, variations in clearance can occur during flight, this ultimately requires a need to manage the sealing within aero-engines. An abradable seal manages to fulfil the requirements for running and handling along with general flight to help reduce the clearance and prevent damage to aero-engine components. Figure 6 represents the evolution of running and handling procedures with abradable linings present and how they protect the components as well as providing a seal, this includes the front view of the blade passing on the left followed by the rotational view of the cut on the right.

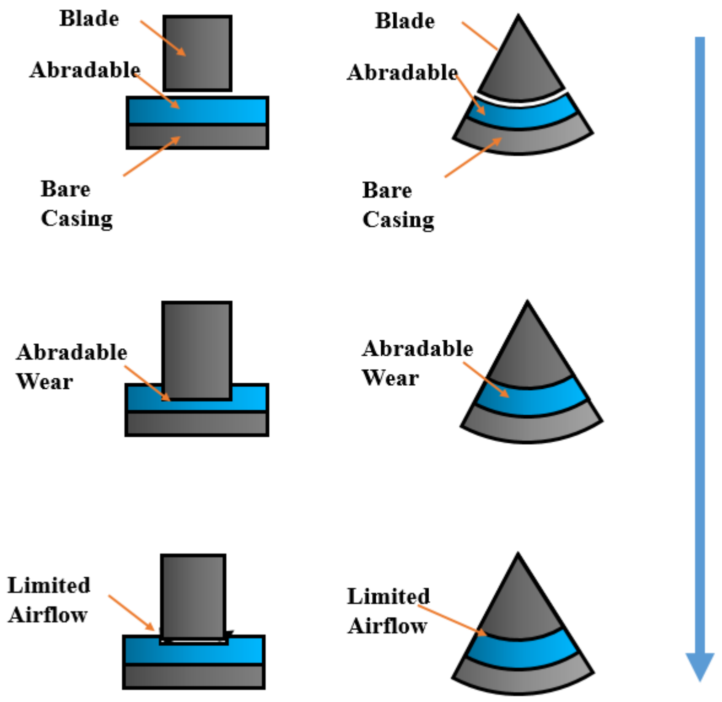

Figure 6. Evolution of stages that occur in running and handling to create a seal – front view on the left followed by the rotational view of the cut on the right

Running and handling procedures provide the engine manufacturer with confidence that the engine will perform as expected under various flight conditions such as a full-thrust acceleration or harsh manoeuvres. This is representative of the take-off and landing parts of a normal flight cycle. Within this region the blades will be rotating at maximum velocities, these blades extend due to a combination of thermal expansion and elastic deformation as a result of centrifugal forces acting upon them. These will come into contact with the abradable liner acting as a machine tool tip, cutting a path in the softer abradable layer, this will ensure that the blade tips sit nicely within the shroud and any lack of concentricity is removed. The mechanics by which the abradable material is cut is dependent on the type of abradable liner and the conditions it is run at. The depth of this path created will be dependent on the in-built clearance tolerance of the compressor stage and the extension of the blade during maximum thrust conditions. As the engine decelerates the blades will elastically contract to their original length. The resulting path cut into the abradable will mean that, essentially, there will be a zero clearance between the blade tips and abradable during normal operating conditions and manoeuvres such as take-off and landing, a liner material also remains to accommodate any unplanned incursions. In some aero-engines the casing is circular and fully concentric to the path made by the blades, for these running and handling procedures are not necessary. Considering Rolls Royce engines which are oval shaped there must be enough abradable to cut on every side, this phenomenon is called a kiss and a cut. This is where on the wide part of the oval the blade just kisses into and sits in the abradables lining relatively shallow to provide substantial sealing. However, on the narrow part a lot of material is removed and so a running and handling procedure is required so that engine clean out can be carried out due to the large amounts of debris formation. On a concentric casing a kiss is achieved uniformly into the abradable lining and sufficient sealing is achieved, during this little debris formation occurs and so running and handling procedures are unnecessary.

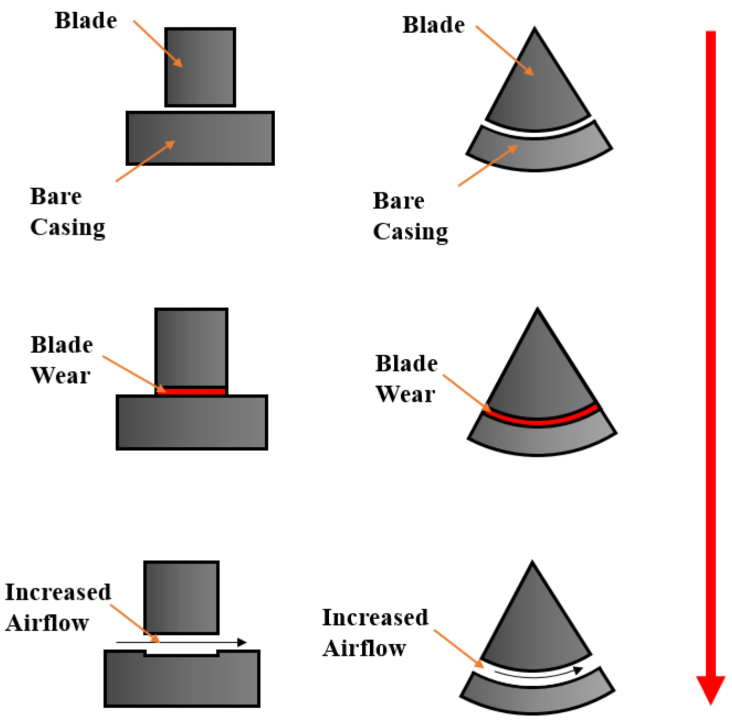

Figure 7. Wear behaviour and opening of clearance when no sealing management present in compressor stage - front view on the left followed by the rotational view of the cut on the right

If no abradable lining exists, Figure 7 shows the evolution of what occurs, thermal expansion of the blades causes dilation outwards, this cuts into the outer casing causing blade wear and damage to the engine casing. This open up the clearance to allow increased air leakage over the side of the blade tips which can reduce the efficiency and performance of the engine.

If Rolls Royce engines do not meet the performance requirements stated to the customer, the company are inclined to pay a penalty fee to cover the extra costs of fuel and maintenance required. Engine specific fuel consumption (SFC) and exhaust gas temperature correlate with the blade tip clearances seen in aero-engines. Wiseman et al. investigated the effects of tip clearance increase with respect to specific fuel consumption and exhaust gas temperature. During cruise conditions 1 mm of clearance is worth as much as 0.l% SFC, therefore 10 mm of reduced clearance is worth approximately 1% SFC which can be critically a large amount of fuel savings and cost for the service lifetime [14].

2.2 Current Sealing Materials

Materials selection is critically important for any part or component to meet the needs and functions of its application. Various materials can provide different approaches to achieve the desired outcome, these can be optimised to obtain the full potential of a material dependant on the materials mechanical and thermal performances.

The materials themselves must be able to withstand erosion and oxidation resistance from presence of airflow and should be able to bond well to the substrate/casing surface. They must be able to tolerate high temperature conditions and extensive thermal shock and cycling where the material will experience heavy thermal loading conditions. Good abradability upon contact with the blade is very important, it should break easily to not damage the blade however, it should also compress to the desired shape. Often seen in current engines, abradable coatings show signs of compression where the surface and near subsurface of the coating becomes denser. As a result of this densification more violent abrasive wear is likely to occur damaging both the abradable lining as well as the blade. This ideal combination of properties is difficult to achieve through a single material, and often a composite material with a metal matrix which also includes a solid lubricant phase for better abrasive wear and easier breakdown when in contact with the blade used [15].

2.2.1 Desired Material Properties

Abradable seals should have relatively low structural strength in comparison to the blade thus to minimize damage to the mating blade tips, material transfer and blade wear are two common results of unsuitable material structural strength. Structural strength and integrity is an important factor to consider, abradable materials should compress and fracture when a force is exerted however when in contact with a blade must also breakdown, this creates the seal through reduction of the blade tip clearance. If the incursion or temperature is too high, the microstructure is crushed as a result of the materials elastic and plastic properties, crushing is mainly due to the porosity present within coating layers.

Xiao et al. investigated how to accurately measure the elastic moduli of different commercially available coatings [16]. The results implied that many of the coatings had extremely low elastic moduli in comparison to the substrate they were adhered to. This indicates that for a given strain the force applied to deform is lower. Some of the coatings, including graphite and polyester phase, deformed plastically. Hardness was also investigated, Metco 308NS Ni-Graphite powders had the highest microhardness readings. Metco 308NS has interesting properties, it showed decreased hardness under higher loading conditions, the graphite phase helps to promote load transfer and elastic recovery of the coating upon impact. It is important to consider these since if the properties are not chosen sensibly this can cause damage to the blade and hence the service life.

Erosion resistance is very important for abradable coatings due to the harsh environments it must withstand. Sporer investigated erosion resistance of coatings according to GE E50TF121CL-A specifications, where 600 g of alumina particles (50 μm) impinge onto a coated surface with a standoff distance of 100 mm [17]. A micrometer is used to measure the deepest point of erosion, this is used to determine the GE erosion number. The GE erosion number is equivalent to the test time divided by the depth of erosion (inches) multiplied by a thousand. The units for GE number are expressed as s/mil which represents the time necessary in order to erode 25.4 μm of the coating. The higher the GE erosion number the better the erosion resistance for the coating. Sporer’s main findings were that by producing finer ceramic phase particles for the spraying process, the erosion resistance improves at the expense of thermal shock life. Erosion performance is of great importance since this determines the durability and effectiveness of these abradable coatings.

A coating's resistance to thermal shock and thermal cycling is a major requirement for seals in turbine engines. Many abradable coatings can be exposed to severe thermal cycling conditions. For modern civil aircraft engines this can range from -50°C to 650°C at the latter stage of the HPC during take-off. Novinski et al. investigated temperature cycling by alternate heating and cooling the coating surface with an oxygen-acetylene flame and a cold air jet [18]. The cycling conditions consisted of a temperature range of 1150°C - 130°C, heated to 1150°C for 5.0s and cooled to 130°C for 5.0s. The test criterion to see the coating performance was the total number of thermal cycles the substrate can endure before cracking and delamination. The cycled zirconia coating cycled 35 times before cracking and delamination was initiated, Novinski compared current commercially available thermal barrier coating which exhibited delamination after 15 cycles under equivalent conditions.

Mumm examined the thermal cycling for two commercial abradable seals [19]. The first was dysprosia stabilized zirconia hBN polymer, the second was a yttria-stabilised zirconia polymer. The furnace program exposed the substrates to 1100°C with a 10°C/min ramp rate for 10 – 145 hours. Aging studies showed that both coatings under the same conditions displayed microstructure evolution which affects the deformation behaviour of the abradable coatings. Typically both materials show cracking and expansion of pores with thermal aging, this is a result of the instability of the materials when exposed to temperature for extensive amounts of time.

2.2.2 Current Materials and Manufacture

Aluminium based composite materials are commonly used within abradable coatings, these materials are very desirable due to the soft shearable property of the materials with the higher strength shearable metal alloys. Many polyester phases are present, these burn out during operation acting as a dislocator phase leaving a porous structure which can breakdown more easily. Aluminium is combined with many constituents to produce many abradable coatings. One coating concept combines Al-Si with hexagonal Boron Nitride (hBN). The hBN phase acts to boost the lubricity and furthermore the temperature resistance, these coatings are most suited to rub incursions of steel, nickel alloy or titanium alloy blades. Common aluminium matrix abradables used are Metco 313NS (Al-Si/Graphite), Metco 320NS (Al-Si alloy/hBN) and Metco 601NS (Al-Si/polyester). Figure 8 shows the microstructural composition of each of these three thermally sprayed coatings, the lighter phase is the aluminium due to the lighter colour, aluminium is a heavier element so it backscatters electron more easily in comparison to lighter elements. The darker phase shows the respective graphite, hBN and polyester fillers, these promote material removal through shear localisation.

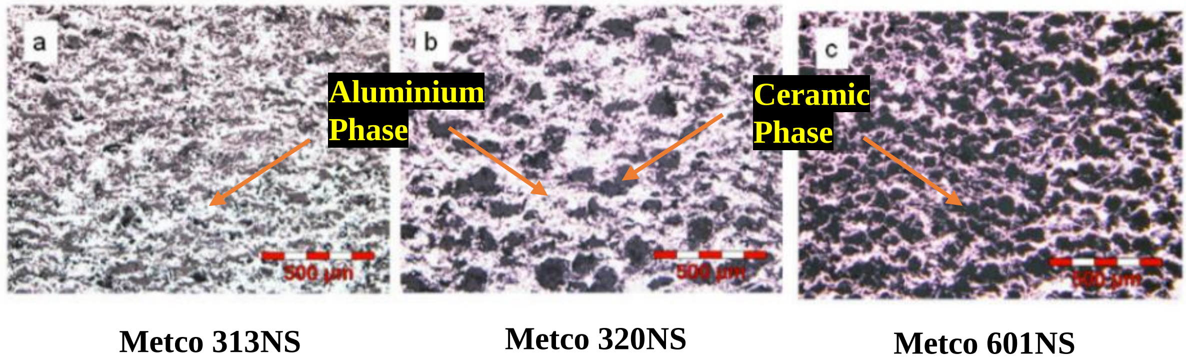

Figure 8. Microstructure of different aluminium based abradables: a) Metco 313, b) Metco 320, c) Metco 601 [8]

Furthermore, Nickel-Graphite (Ni-Gr) are composite powders which are manufactured using a hydrometallurgy autoclave process, this process allows the encapsulation of the graphite core within a nickel shell to form and continuous cladding. The hardness of the coating can be varied through a different ratio of nickel and graphite and also by adjusting various spray parameters. Ni-Gr coatings are classically suited for rub incursions against steel and nickel alloy blades, knives or labyrinth seal strips, also titanium blades. However the titanium blades must be sprayed to the correct hardness for optimum performance.

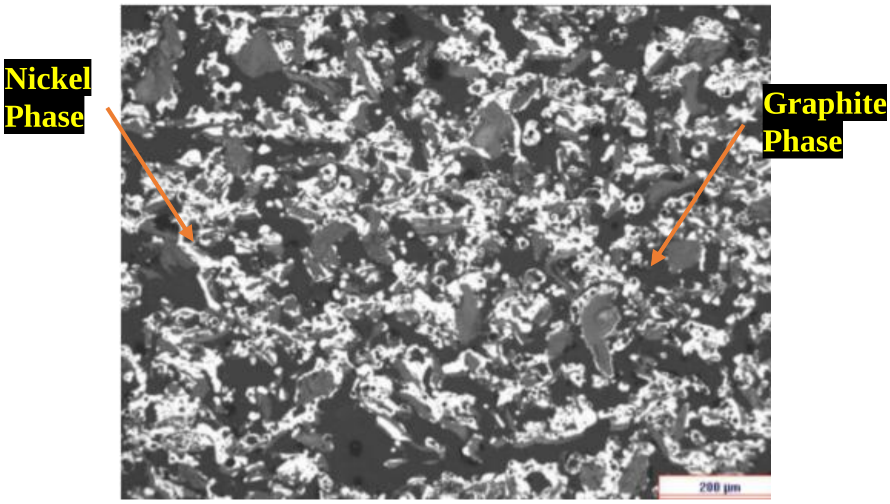

Figure 9. Ni-Gr abradable material microstructure and separate phases [8]

An example of commercially used Ni-Gr is Metco 307Ns-2 Durabrade 2223. Figure 9 shows the microstructural composition and separate phases, there is a need for porosity to help encourage particle removal during operation.

NiCrAl composites are also manufactured using a hydrometallurgy autoclave process of Bentonite clay with a thin layer of alloyed NiCrAl. The hydrometallurgy autoclave process is a chemical leaching method that extract metals from their ores or concentrates using aqueous solutions at high pressure and temperature. This metal matrix-dislocator coating consisting of a bulk metallic phase with a dislocator phase (a microstructural region of defects within the crystal lattice often formed through mismatches in thermal expansion) is designed for a maximum temperature of 900°C. Bentonite is a clay-rich material, the main constituent is smectite which is a hydroxyl-aluminoscilicate containing alternate layers of a structure of one octahedral alumina sheet which is sandwiched between two tetrahedral silica sheets. The main function of bentonite particles is as a dislocator phase to disjoint the metallic lamella (thin, plate layers of metal often formed due to phase separation, deformation or specific metallurgical processes) making it sufficiently friable (how easily a material crumbles due to weak bonding or structural integrity) so that there is optimal abradability during the rub process [19]. Figure 10 shows the microstructure and composition of NiCrAl and separate phases. The lighter regions are NiCrAl whereas the grey regions indicate the bentonite phase, the darker black regions are pores within the microstructure.

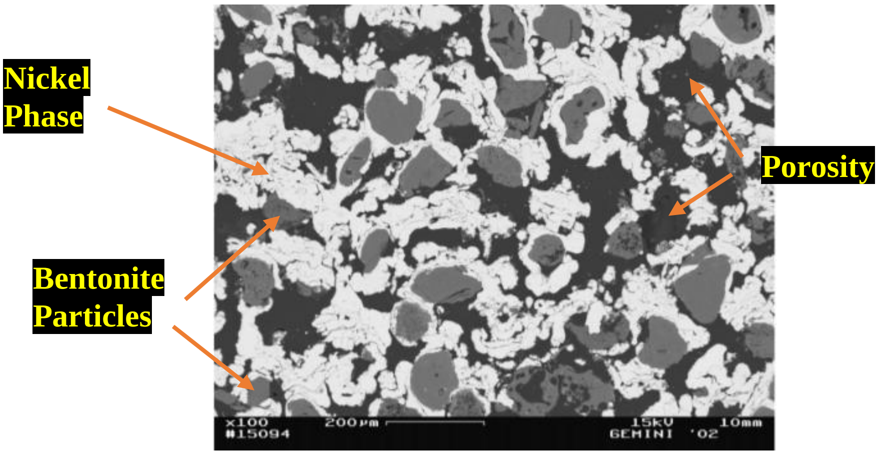

Figure 10. NiCrAl microstructure and phase distribution [8]

NiCrAl powders tend to be more spherical, mainly consisting of large bentonite particles trapped within an open network of lamellar metallic splats. Faraoun investigated and found that this particular coating presented a large percentage of porosity estimated to around 31% and furthermore that the particles are distributed without any preferred orientation [20]. Common commercially used NiCrAl abradable coatings are Metco 314 and Metco 312. Porosity is present to help assist the abradability of the material when in contact with the blade.

HVOF (high velocity oxygen fuel) spraying and APS (atmospheric plasma spraying) are common techniques which have been used across a wide range of industries for a long time, these techniques are both viable for applying abradable coatings onto engine casing lining to provide good sealing. The HVOF thermal spraying process that uses a mixture of oxygen and fuel to create a high temperature and high speed flame. Fine metal/ceramic powders are injected into this flame where the particles become semi molten and soften, after which are propelled at supersonic speeds onto a surface. The high velocity at which particles are propelled ensures a strong bond which creates a dense, hard and wear-resistant layer. Figure 11 shows a schematic that illustrates the thermal spraying process [21]. Temperatures reached are sufficient to melt nickel and lower alloy content nickel alloys. The deposition velocities and temperatures tend to be lower than those for high energy plasma deposition. The oxygen-fuel ratios and pressure likewise are adjusted when necessary to produce porous coatings onto the substrate. Typically the powder size is relatively coarse (10-50 μm) to allow sufficiently less heat transfer to the particles [22].

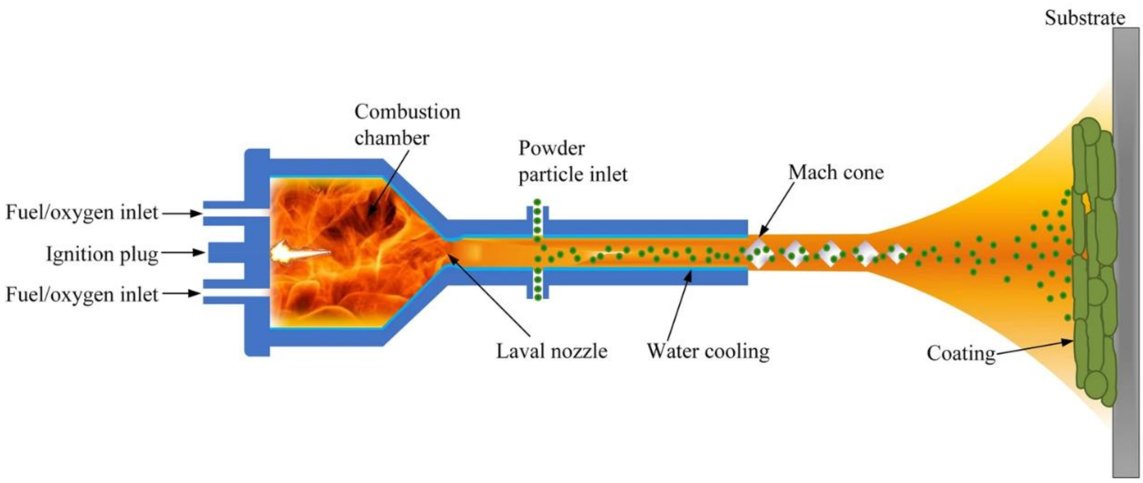

Figure 11. HVOF thermal spraying process [21]

APS is a coating technique which uses a plasma torch as a heat source. An arc is present which allows the ionization of plasma gas in which the particles of the coating are able to be injected, melted to a semi-molten state and carried to the substrate. Several gas mixtures are used however for the selection there are two main parameters to be considered, these include a primary heavy gas and a secondary gas. The requirement for the primary heavy gas such as argon (Ar) and nitrogen (N_2) are to assure a consistent flow of and particle entrainment, the secondary gas such as hydrogen (H_2) and helium (He) improve the heat transfer to the coating powders. Under standard operating conditions, temperatures of 20,000°C can be achieved, this allows the capability to melt any kind of metal powder [23].

There are two main advantages of atmospheric plasma sprayed abradables over flame sprayed abradables. Firstly the high energy input to powder particles, this can create a semi-molten state for a wide range of particle sizes and particle constituents. Secondly the availability of spraying composite blends of various different materials to a high degree of microstructural control. For example polyesters as fillers or porosity generators which are sprayed together with aluminium alloy, MCrAlY alloy or any other ceramic powder [19].

2.2.3 Current Challenges of Materials

Many challenges need to be faced regarding current sprayed material coatings for engine sealing. For Rolls Royce if they do not meet the requirements for fuel consumption, performance and service lifetime, a penalty payment is in place that Rolls Royce would pay out for not reaching the standards guaranteed upon purchase and distribution.

Metco 314 is Ni-based powder often used for abradable sealing lining in the compressor stages of aircraft aero-engines. This sprayed abradable has a large amount of porosity which can aid the breakdown of the lining, however this can also cause problems and pose challenges during operation. Often it is identified that there is distortion and compaction within the abradable coating, this is a result of the large amounts of porosity present. Densification of the material lining causes redundancy of the porosity due to the compaction and therefore surface collapse. Many of the abradables compact so much that they do not fracture by the time the blade reaches those specific regions, the blade then overheats and damage is seen often in the form of cracking.

One of the main issues with current aluminium abradable materials is the debris formation which occurs when the lining is worn upon contact with the blade. Ideally the debris formation should be fine powders, however due to high temperature and pressure conditions adhesion occurs leading to formation of oddly shaped chunks. Additionally, adhesion is also commonly seen that occurs to the blade tip, this can lead to overcutting of the abradable lining which results in large clearances and loss in engine performance. Another issue seen in Metco 320 is due to the material variability and consistency during the spraying process, this cause localised blade damage.

Debris formation can cause blockage of the combustor inlet causing reduction of air inlet, this can generate disruption of airflow within the compressor stages, an extreme consequence of this is surge. Surge is the increase in rotations per minute (rpm) of a stalled compressor. The compressor blades are airfoils not unlike propellers and wings which stall if airflow is not maintained at the proper angle of attack within the compressor stages of an aero-engine. In more extreme circumstances this can cause the direction of flow to change in the opposite direction, with the mix of fuel and high compressed gas in the compressor stage ignition can occur causing explosions and total failure of the system. This is alleviated by larger clearances and less rubbing of the abradables, however this clearly reduces the efficiency [24].

Maintenance costs for such failures and damage can be very costly to a company such as Rolls Royce, where teardown and removal of the engine is required these numbers clearly exceed 1 million pounds. Furthermore, service lifetime can be influenced greatly by the amount of maintenance and problems occurring in the aero-engine. Service and maintenance costs include replacements of components and further the labour and staffing required for such a job.

2.3 Metallic Foams and Cellular Structures

Metallic foams are open pore cellular structures usually consisting of nickel and iron alloys with uniform structural and material properties. Through adaptation of various cell sizes (450, 580, 800, 1200 and 3000 μm) they are suitable for different applications due to the easy formability, light-weight and design flexibility. Metallic foams have many unique properties including consistent porosity, with exceptional heat and corrosion resistance, excellent metallic strength, stability and durability. One very unique entity of metallic foams is their ability to be tailored to any application and are flexible in how the mechanical and thermal properties are enhanced and controlled. They offer two types of metallic foam constituents which include Ni-based and Fe-based alloy. Nickel based alloys include NiFeCrAl, Inconel, NiCrAl and monel whilst iron based alloys include FeCrAl and STS (special treatment steel) [25].

2.3.1 Manufacturing Process and Material Properties

A powder metallurgical process is employed to produce metallic foams, converting the nickel or iron into a high-temperature stable and corrosion-resistant alloy material [26]. A polymer foam template is utilised onto which nickel particles are electrodeposited to create the nickel foam depicted in step 1 of Figure 12. Porosity within the foam structure is controlled through the size of the polymer foam template. Step 2 involves the spraying of a binder solution onto the nickel foam, providing an initial adhesive surface for alloy powders. The precursor sheet material is further sectioned into smaller parts and layered; once compiled into layers, the sintering process commences.

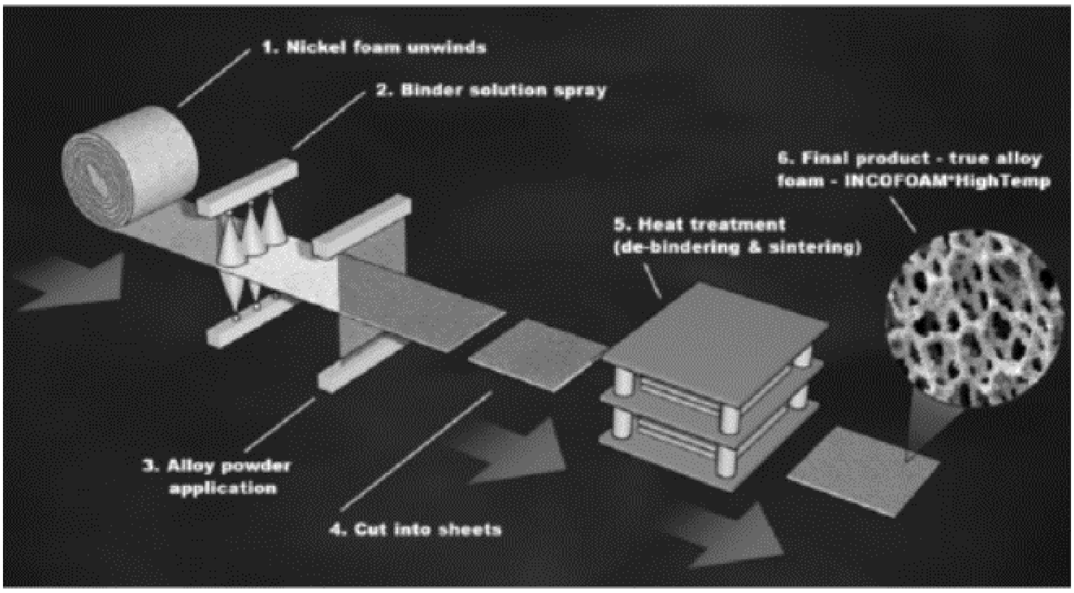

Figure 12. Manufacturing process for alloyed Ni-based foam [26]

The sintering process take advantage of the materials transient liquid phase which allows powders to diffuse into the foam struts to generate a solid state upon cool down. Figure 13 shows a comparison between pure nickel foam on the left and alloyed foam on the right. These can be achieved to fit a variety of different applications and uses, many current metallic foam materials are used for filtration due to their excellent surface area and porosity ratios. This helps to reinforce that the mechanical and thermal properties can be altered through the use of different powders and constituents being introduced into the coating processes [26].

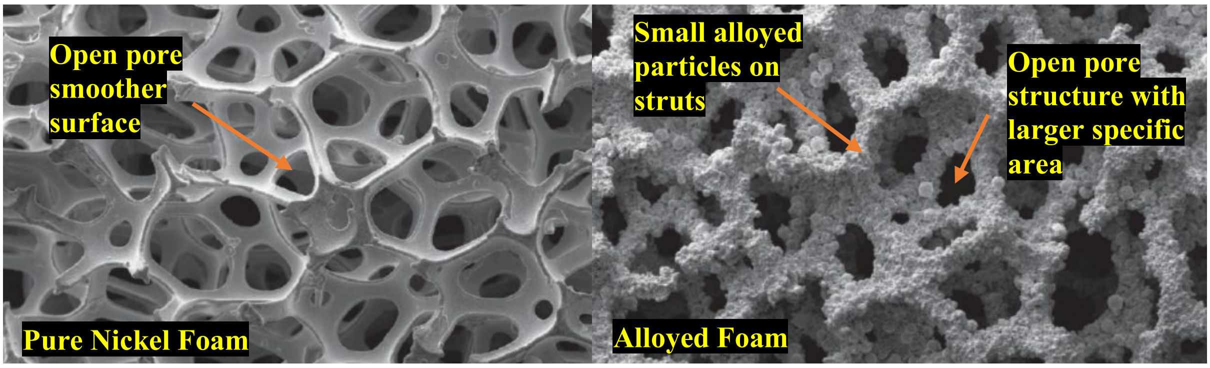

Figure 13. Comparison of microstructure for pure nickel foam and alloyed foam [26]

After the forming of the metallic foam substrates they are injected with a polymer resin to potentially enhance the cutting ability and performance. For the filled foam tests in this study polymer resin is injected into the metallic foam substrates via a pressure-assisted polymer injection method. The metal foam is placed into a mould or container, a liquid polymer is then injected under high-pressure to force it into the metallic foam's pores. The polymer is cured to solidify the structure. These filled foam substrates are formed in house by Rolls Royce.

Closed foams were also considered as an alternative substrate for abradable linings. However, initial testing indicates that the structure is unsuitable due to its high mechanical strength and tendency to cause severe wear marks on the blade. C. Motz presents a study investigating the behaviour of closed-cell aluminium foams under tension; the study identifies that dislocations and fractures are likely to propagate along the interfaces between the porous pockets [27]. The rub tests conducted clearly show that, similarly, the fracture and deformation of the closed metallic foam occur in the same areas where large empty pores are revealed. Open-cell foams can be compressed more easily and are more likely to leave the blade with less damage after a rub.

2.3.2 Performance of Metallic Foams

Gunnar Walther et al. investigated the oxidation and corrosion resistance of such metallic foams to monitor their performance and behaviour along with high temperature testing [26]. To evaluate the oxidation resistance the foams were exposed to set temperatures of air between 700°C - 1000 °C for a total time of 20 h after which after which the mass gain was measured and energy dispersive x-ray spectroscopy (EDX) carried out to determine the amount of oxidation that had occurred. The results showed that FeNiCrAl foams have superior oxidation resistance in comparison to Inconel 625, the aluminium content in FeNiCrAl foams enables the formation of an aluminium layer which can ensure excellent oxidation at temperatures above 950 °C. It was seen that the chromium reinforces the aluminium scale formation as this will prevent internal aluminium oxidation to occur. Pre-oxidizing of the alloy was also tested to see the effects it would yield, this can further reduce the oxidation this allows the protective layer to form before it is exposed to any high temperatures. The oxidation resistance of Inconel 625 is based on a chromium layer which is only stable for temperatures which are under 900 °C [26].

For foams which need to withstand extended service life under high-temperature conditions, pre-oxidizing the foams can establish a protective layer which helps enhance the material's corrosion resistance. The most desirable layer is the α-alumina, as it exhibits the best high-temperature protective characteristics. For the currently used FeNiCrAl, which contains aluminium, it can be assumed that when in contact with oxygen, an alumina layer will form. A great challenge is to limit the formation of other oxides besides alumina, as these can be harmful towards the metallic structure of the foam struts. In addition, the oxidation resistance of these foams increases with the homogeneity of the alumina scale. A regime was developed with an oxygen-containing atmosphere which ensured only the formation of α-alumina. The parameter adjusted was the oxygen partial pressure in the atmosphere, this suppressed the formation of chromia and allowed a dense and homogenous with no other oxides present form above it acting as a diffusion barrier coating. Further microstructural analysis was conducted and it was perceived that the material showed no internal oxidation or AlN precipitates. Without the presence of this alumina scale, nitride formation is prominent and is clearly observed. For this to occur, the aluminium phase is consumed towards the surface, which, as a result, creates a weaker alumina scale formation, and therefore, there is less oxidation resistance [26].

Furthermore, Gunnar Walther et al. investigated the mechanical behaviour of metallic foams after oxidation tests at high-temperature exposure [26]. A simple 3-point bend test was conducted to allow the analysis of how these materials behave and their retrospective strengths under loading conditions, a support width of 25 mm and a crosshead speed of 2 mm per minute. There were no distinct differences between the mechanical behaviour of oxidised foam with respect to an as-sintered state where a common trend of decrease in strength and an increase of elongation was observed. However, foam strength is influenced by temperature conditions up to 900 °C. It was clearly seen that the bending elongation decreased by 30-50 % with increasing oxidation temperature, where the largest gap was identified to be at a temperature of 700 °C. A unique property is that the metallic foam structures did not become brittle after oxidation.

Durability test was conducted where the metallic foam structures were exposed to a diesel exhaust atmosphere for different lengths of time, 10 h, 30 h and 100 h, with a surrounding temperature of 900 °C. Three samples were tested, a sintered sample, two of which were pre-oxidized at air and low partial pressure. It was seen that mass gain increases with time and temperature, additionally the pre-oxidation procedure helps to reduce the mass gain on metal foam struts [26]. These properties and characteristics all make foams very suitable for abradable linings. However, much work is needed to provide further research on the breakdown mechanisms and optimisation of the material structure.

2.3.3 Testing Methods for Abradables

Previous research at the University of Sheffield has concentrated on testing methods for abradable materials [15], [27]–[30][31]. These testing methods utilise test rigs that simulate the blade-to-abradable interaction on a smaller scale. Standardised testing methods collect in situ measurements to determine the factors that cause wear marks and scars. Instrumentation allows for the measurement of force in both the tangential and normal directions of the rub, as well as spot temperature and imaging of the blade and abradable substrate. These measurements assist in identifying the wear mechanisms at play and how they influence the abrasion and wear properties of coatings.

The rigs employ a spinning disc with a blade attached; a singular contact blade is designed to replicate the wear conditions. The sample is mounted onto a dyno, which is positioned on a stage that brings the sample towards the rotating blade at a set speed. Generally, the tests are conducted up to specific incursion depths, and the incursion rate (the speed at which the stage moves) dictates the test duration. This test rig forms the foundation of the experiments conducted in this PhD. The next chapter will provide a more detailed description and breakdown of the rigs, where additional improvements and instrumentation are incorporated into the test rigs.

2.4 Summary

The literature review identifies a research gap where current abradable materials struggle to provide consistent performance in service, emphasising the need for a replacement. Even under optimal conditions, these materials have been shown to exhibit numerous issues, as discussed in the literature review. Metallic foams show promise due to the flexibility of their design; their mechanical and thermal properties can be tailored through parameters such as nominal pore size, porosity percentage, and the combination of high alloy powders used in spraying. This PhD aims to further explore the potential of these foam substrates to achieve improved sealing in the aero-engine compressor stage.

Chapter 3

Methodology

In order to fully test the capabilities of abradable samples for aero-engine linings, a test rig has been previously designed to allow control over many parameters, such as incursion rate and depth, as well as the blade tip velocity. This methodology outlines an experimental approach to testing abradable materials using a representative rig; the rig has been extensively used previously and detailed in a series of papers [15], [27]–[30]. In the following section, a brief overview of the rig will be given with a focus on novel aspects such as digital image correlation and vacuum impregnation techniques to preserve internal sample structures.

3.1 Testing Rig Set Up

Figure 13 shows the test rig set-up at the University of Sheffield. This is the low speed rig and can test to a maximum speed of 200 m/s and a varied incursion rate from 0.02 – 2 μm/pass. The test rig allows an abradable material to be mounted onto a stage, which raises the abradable towards the rotating blade. This is to recreate the interaction seen within aero-engines where the blade first comes into contact with the abradable lining.

The rotating component of the test rig is comprised of a rotating disc with two blades coupled to it, one a dummy blade and another the wearing blade. The disc is coupled to a spindle, which is under the control of an inverter controller which allows the rotational speed of the disc to be set. A stage on which the abradable is mounted is located beneath the disc. This is an electronic Z-axis stage connected to a programmable stage controller which can be controlled through an external PC. This entire rig is mounted onto a steel bench which is securely fastened to the floor to reduce vibrations during testing procedures.

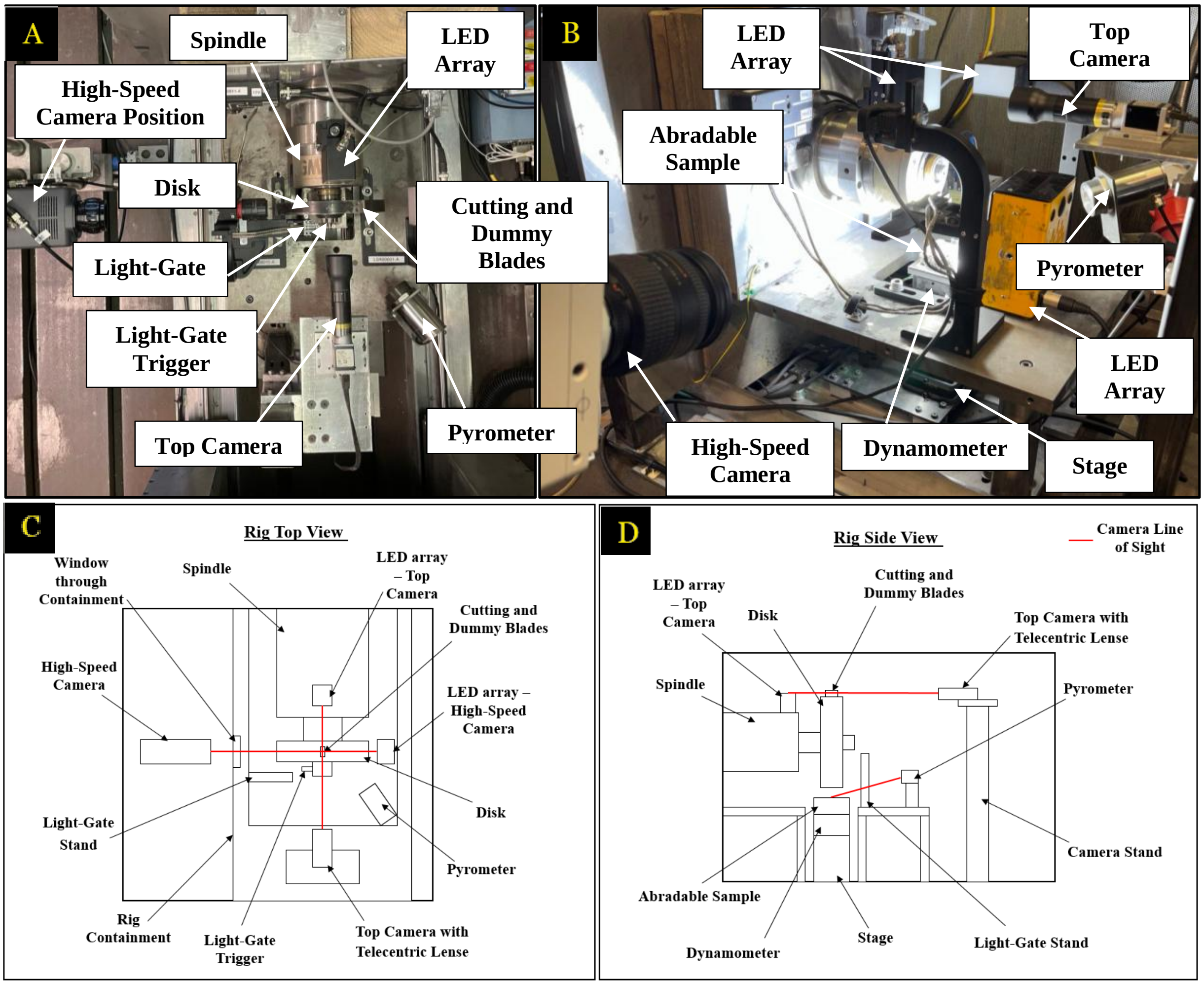

Figure 14. (A) Rig top view (B) Rig side view (C) Schematic of rig showing top view (D) Schematic of rig showing side view

3.1.1 Disc and Spindle

The horizontally mounted spindle used is a GM HSP 120g high frequency grinding spindle with permanent lubrication (GMN Paul Müller Industrie GmbH \& Co. KG, Nuremberg, (Germany), type HSP 120 g - 21000/9). This is capable of reaching 21000 rpm rotational speed which is equivalent to 240 m/s for a 109 mm radius disc attached. Coupling is achieved through use of a HSK-C40 tool that attaches the spindle and the disc together, these parts are clearly indicated in Figure 14.

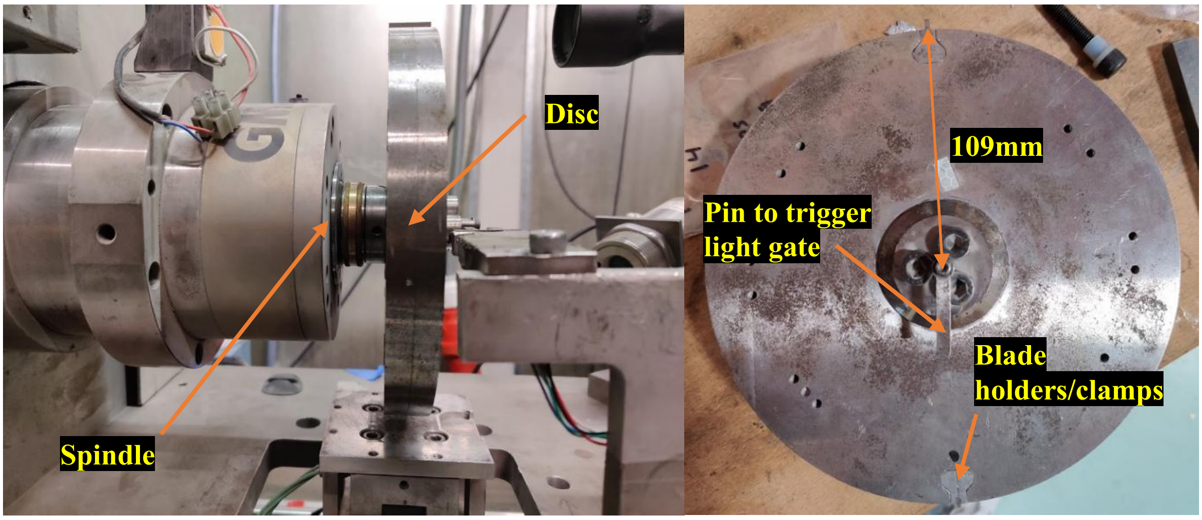

Figure 15. Disc and spindle used for low speed rig testing

The disc was manufactured with two holes which are exactly 180° apart to house the blades used for testing. These two holes accommodate two clamps which grip the blade tightly due to it having to withstand the forces of the blade when it comes into contact with the abradable. Two threaded holes are present on the outer circumferential edge of the disc in order to insert two grub screws through the disc (Figure 15). These press down on the clamps and apply pressure tightening the adjoining part and preventing vibrations and loosening of the blade during the test procedure.

A dummy blade (Figure 16) is used for balancing purposes, this blade is equal in mass but set into the disc further. This allows contact for only a single blade, balancing of the disc will generate less vibration and smoother running of the blade at higher speeds.

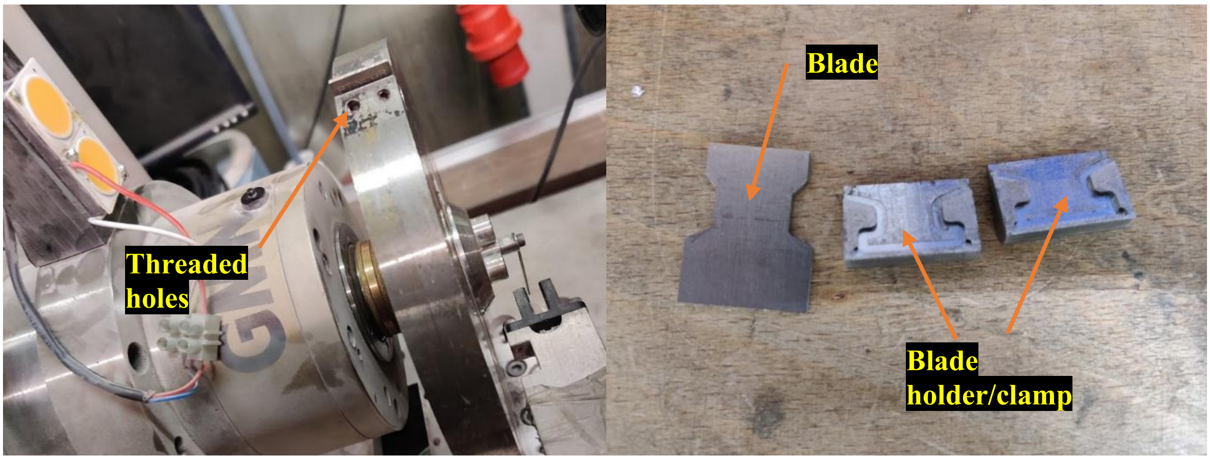

Figure 16. Position of blade and clamps to show how it is fixed to the disc

3.1.2 Stage Controller and Dynamometer

The Z-axis microscope stage, which mounts the sample and moves it towards the rotating disc and blade, is the OSMS80-20ZF-0B. The specifications are shown in Table 1.

Table 1. Stage specifications

OSMS80-20ZF-0B Stage Specifications	
Travel Displacement (mm)	20
Stage Size (mm^2)	80 x 80
Stage Material	Aluminium
Resolution (µm/pulse)	0.2
Max Speed (mm/sec)	1
Load Capacity (N)	147
Weight (kg)	1.6

The stage is bolted into the bottom steel plate and is fixed to the floor to allow stability for when testing occurs. This is located right beneath the blade and so the sample is raised along a single axis to reproduce this cutting and wear condition. To control the movement to the desired depth and speed a programmable stage controller is connected to enable incursion depth between 0.1 µm – 2000 µm at intervals of $0.1 \mu ms^{-1}$ between the blade and abradable sample. More information regarding this can be found in studies and papers previously done [15], [28], [29], [31].

3.1.3 Instrumentation

A major part of the data analysis is to investigate the amount of blade tip adhesion and material pick up from the abradable sample throughout the test. Front-on stroboscopic imaging can enable high quality images at small time intervals throughout the test to observe and measure the amount of material adhesion or blade wear from the tip surface. The reference point is taken from the first image and the latter images are compared to this datum. A more detailed description of how these are determined is found in Chapter 4.

The instrumentation includes a light gate sensor, LED strobe controller fitted with a signal delay board (Gardasoft Vision RT220F), LEDs (Cree XLamp CXB3590) and a camera (Basler Ace acA1300-60gm Monochrome GigE) which has a telecentric lens fitted (0.25X Silver Series Telecentric Lens, Edmund optics). A stroboscopic imaging system is used to monitor the blade tips during testing, this system has been extensively detailed previously [15]. The schematic is shown in Figure 17.

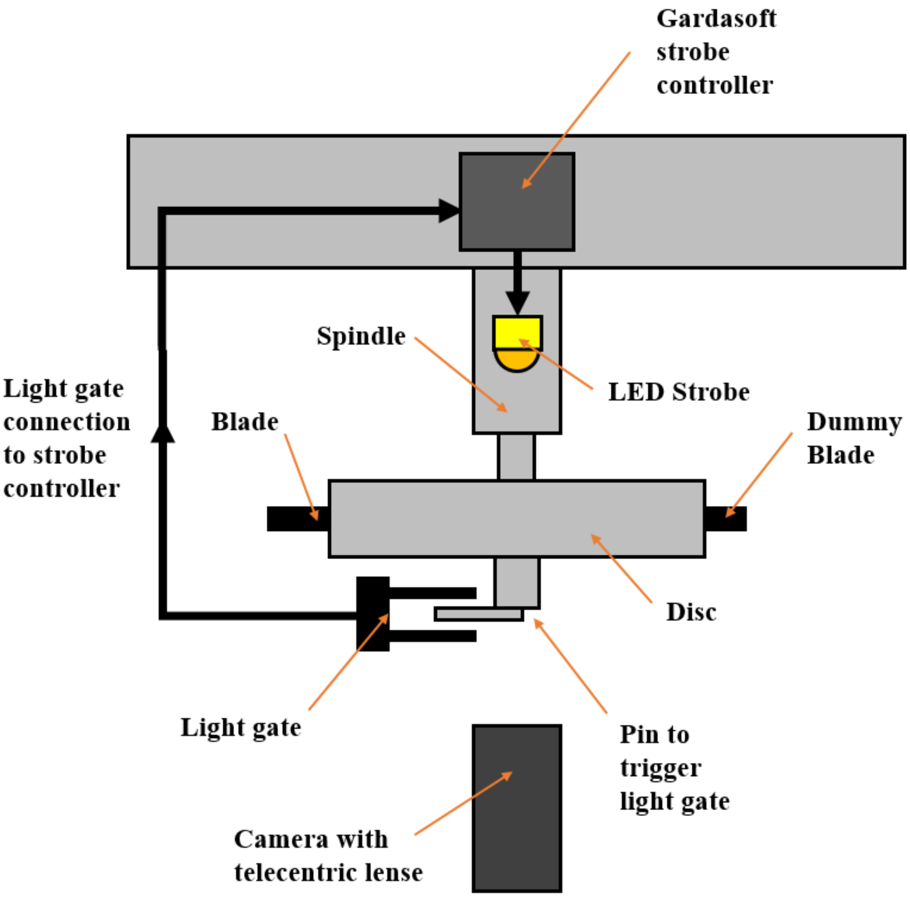

Figure 17. Set-up of the camera and LEDs with respect to the blades, spindle and disc

The schematic in Figure 17 shows the instrumentation around how the blade images are captured. A small pin on the disc triggers a light gate, the light gate is connected to a strobe controller which starts the delay for the strobe. There is a delay for the triggering of the strobe controller and the LED strobe flashing, this is calculated so the blade is in the correct frame position for imaging.

Similarly the low-speed rig is fitted with a pyrometer (CTLM-3H1CF3-C3, Micro-Epsilon, Koenigbacher, Germany) to measure the temperature in the sample, the set-up for which is shown in Figure 18.

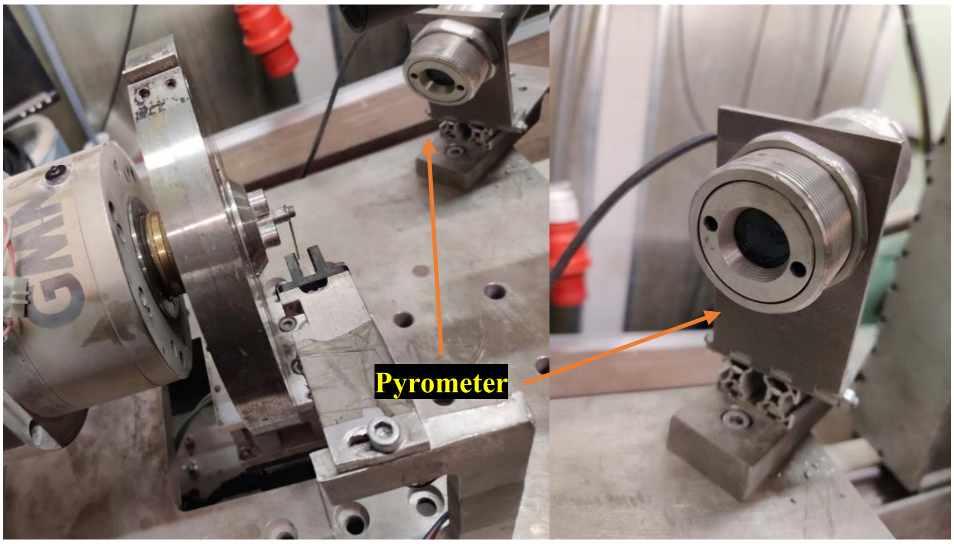

Figure 18. Pyrometer setup in low speed rig

Finally a webcam (Logitech HD Webcam C310) is used in the low speed rig checking for sparks throughout the test. Sparks can indicate excessive temperature between the wear of two metallic phases as the small pieces of metal are hot enough to glow. This can show oxidation, as many metals can burn easily in air through an exothermic reaction generating heat. Figure 19 shows an image of the webcam and it’s placement, it is located underneath the front camera imaging.

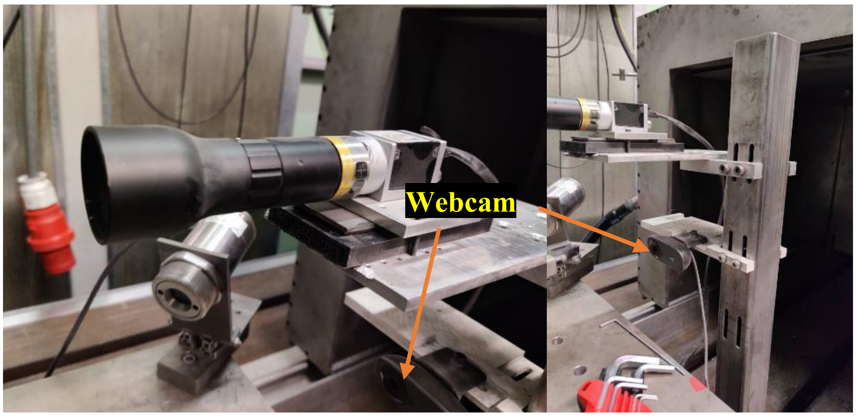

Figure 19. Webcam used in low speed test rig

3.2 Digital Image Correlation (DIC) Set-up

In addition to the current imaging system, digital image correlation (DIC) has been added to investigate the foam structure as the blade interacts. DIC is an optical technique often used to track particle displacement to obtain a strain distribution. During these series of tests, this is incredibly important since it can help to understand how the material behaves under certain loading conditions. Figure 20 shows the set-up of the DIC camera and LEDs used.

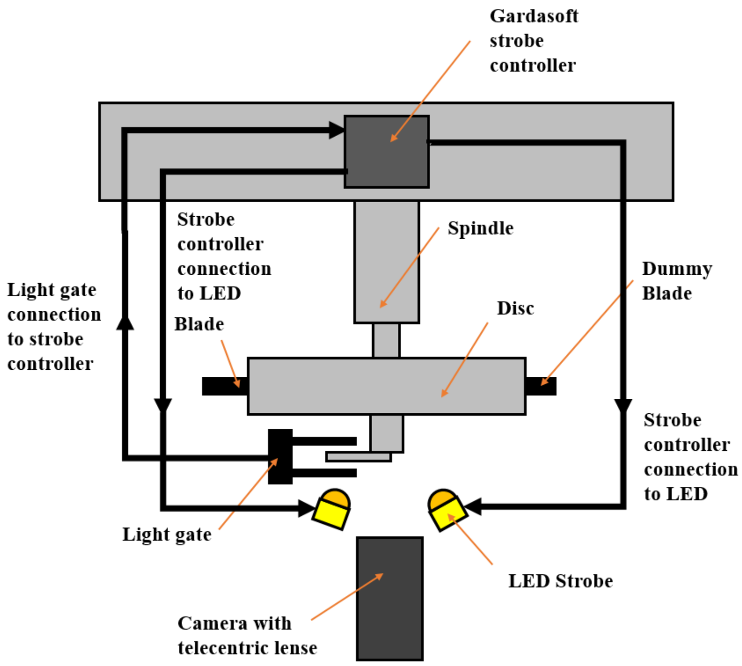

Figure 20. DIC setup and instrumentation positioning

For the front on imaging the LED placement is behind the object, however for the DIC work the LEDs are in front of the sample and angled 30 °C from the projection of the camera. This means that the separate phases can be distinguished from each other clearly and provide more detail of the sample instead of just an outline of the edges. Initially the samples are of this shape and size (48 mm x 48 mm x 20 mm). In order to perform DIC work and investigate the breakdown and impact of the blade on the abradable after each pass, the samples are machined down either side of the blade path. Figure 21 shows two CAD drawings created in SOLIDWORKS, these show the sample before and after machining.

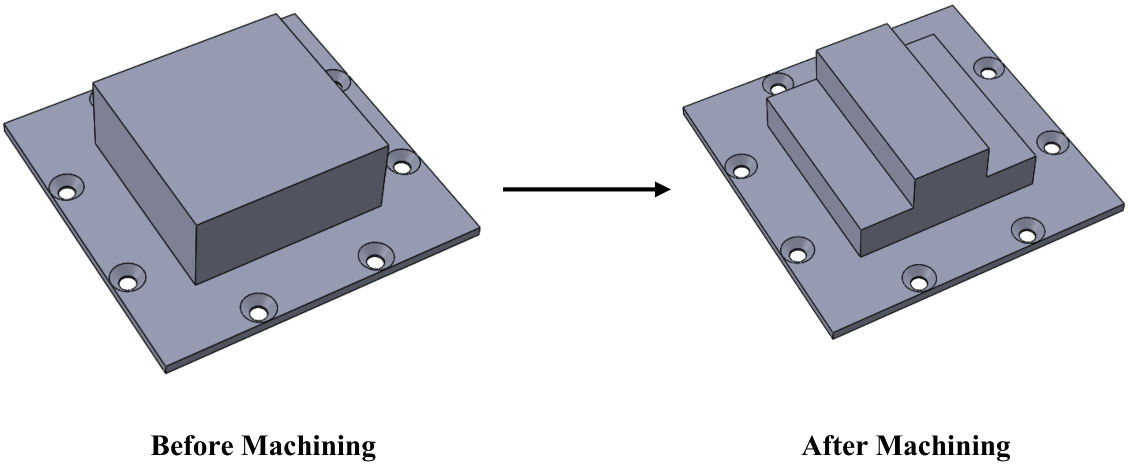

Figure 21. Sample schematics before and after machining

The camera has a specific focal length so for this to be used effectively the stage is moved accordingly to get as much detail as possible and the largest focal window possible. The LED placement is critical to the image quality, iterations are required which involves finding the angle of placement and more importantly the brightness and exposure levels. Due to the polyester phase not reflecting the light as much in comparison to the metallic phase, this requires calibration to optimise the angle of the LEDs position and the exposure settings. Figure 22 shows the final positioning of the LEDs and the sample stage for optimum imaging.

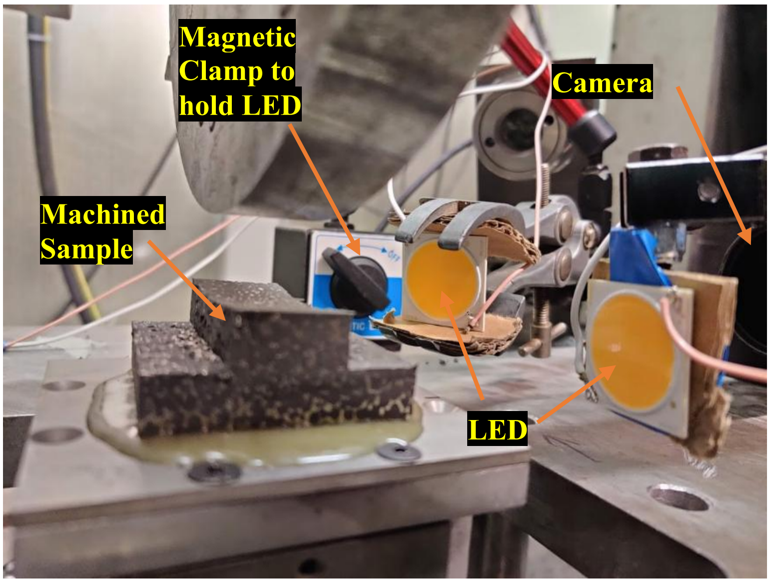

Figure 22. Optimised positioning for best quality imaging for lower stroboscopic camera for DIC processing

3.3 High Speed Camera Set-up

As noted, high-speed imaging is used to capture the blade-to-substrate interaction. The camera used is a Phantom VEO-E 340L high speed imaging device, and is able to capture up to 72000 frames per second (may vary depending on the image size). The camera is positioned outside of the test rig containment shown in Figure 13, and focused on the rub track via a small viewing window. In order to ensure appropriate illumination of the test set-up, a high-power LED is positioned by the sample to provide lighting during a test. Phantom camera control (PCC) software is used to capture images at a frame rate of 10,000 to 20,000 (dependant on the test duration), with triggering of the set-up achieved through synchronisation with the aforementioned LabVIEW programme. In combination with the force and temperature measurements, where any events of interest occur, the imaging system is then used to investigate the nature of the blade – abradable interaction at that point and provide a record of the wear events present.

Chapter 4

Post Processing Data & Technique Development

Running wear and rub tests yields lots of raw data, this includes force and temperature data and imaging data. This section will show an example of how the raw data is processed. It should be noted that the images of the samples have a blade pass direction of left to right and upwards in the vertical direction.

4.1 Standard Data Processing

Data is recorded against time stamp within the machine, this relates to the position of the stage. As the blade incurs with the sample the arc of contact increases, it has been previously demonstrated that it is appropriate to plot results against rub length as oppose to time [15].

An arc length is related to the stage position during the rub test, rub length is the cumulative contact length the blade has upon interaction with the sample. Figure 22 shows the variables to consider for the calculation of rub length. At a blade tip speed of 100ms^{-1}, for a disc radius of 109mm this equates to a rotational speed of 0.146 revolutions per millisecond. With the rotational speed in revolutions per millisecond, the time stamp of each force and temperature measurement is recorded, this time stamp will equate to how many times the blade has passed to the reading recorded.

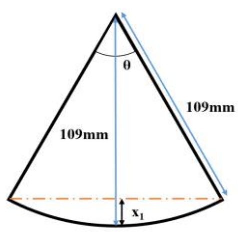

Figure 23. Schematic to show measurements for rub length calculation

The incursion depth is determined according to how many times the blade has passed, equation - 4,1 shows how the incursion depth is related to the arc length. Rub length is the cumulative sum of the arc length for each rotation of the blade, this is used to plot the data.

$$\boldsymbol{Arc\ Length = 2\pi r\left(\frac{2\left(\cos\left(\frac{r - x_1}{r}\right)\right)}{2\pi}\right)} \tag{4,1}$$

Force data throughout the duration of the test is recorded every few milliseconds. This data is then saved and post processed to a single value per pass by taking a peak to peak force per pass.

Temperature data throughout the duration of the test is also recorded every few milliseconds. Raw temperature trace is recorded by the pyrometer, this is also further post processed using the techniques detailed in [15].

Figure 24 shows an example of an image captured by the front on camera, this shows the blade tip along the short edge which is 2mm in size.

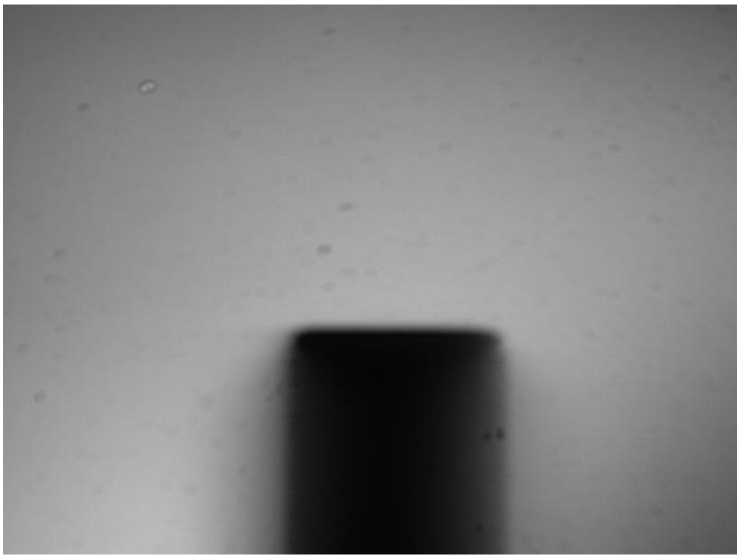

Figure 24. Example image of the blade tip captured by the front on camera

An image such as this is captured every few milliseconds, there will be slight blur in the images due to the blade moving at a high speed, however, an indication of the blade length change can be observed. Macroscopic analysis of these images can help to identify any areas of large wear or material adhesion, furthermore any microscopic or tiny details cannot be observed through normal processing and through characterisation of the blade tips.

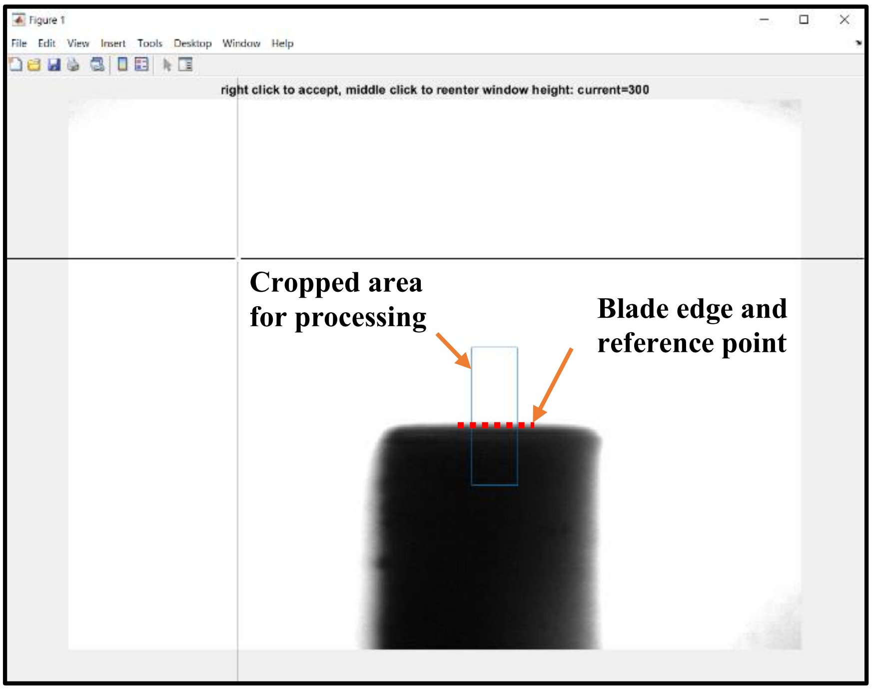

Figure 25. Selection of region for processing and the edge detection to set a reference point

In MATLAB the blade tip change can be monitored, this is achieved by first reducing the noise and finding the top edge of the blade. In order to obtain an accurate reading of blade change a small section of the blade is monitored and tracked. The images are first despeckled and an automatic threshold is applied, an area for processing is selected and the edge is found and set as a reference point for blade length change (Figure 25).

The initial position of the blade tip is determined and set as a reference marker. For the following images the displacement of the blade from this original datum point is measured as the blade length change, this is plotted with rub length to observe the amount of blade wear or adhesion during the test. This process has previously been used extensively in previous studies [15].

4.2 DIC Image Processing

DIC is a powerful tool to evaluate the areas of stress and strain within any given material when under any mechanical loading. In this instance the DIC can be incredibly useful to analyse the failure modes during the rub tests by identifying areas or weakness and more so deformation. Where such failures occur samples can be adjusted and modified to perform better to achieve little abradable and blade damage.

DIC processing is carried out in MATLAB with use of 2D Digital Image Correlation MATLAB Software [32], and is the novel section of the current experimental set-up. DIC is a powerful technique used to provide insight into how the abradable material deforms and the load transfer within a material when interaction occurs with the blade.

The camera captures images of the substrate during the rub test, the initial image is taken as a reference point. Small subsections of features in the sample are identified and tracked through the series of images, the movement of these features are calculated by pixel movement and converted to a displacement. These small subsections are tracked with respect to the previous image in the series. The displacement is further used to calculate strain and stress through the tests. Below shows a flow diagram with the steps of analysis.

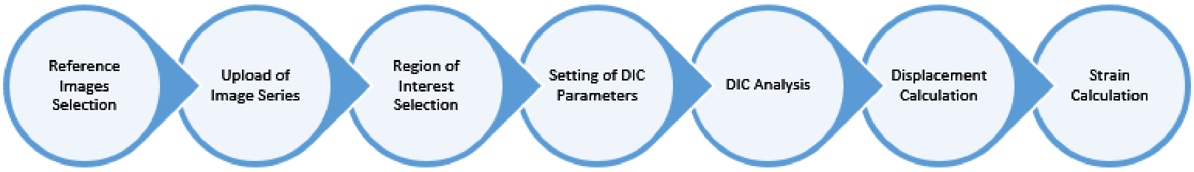

The overall goal of DIC is to obtain displacement and strain fields present within a specific region of interest (ROI) for a material which is undergoing deformation. Images are taken of the material as it deforms, these are the input in to the program. This method uses one-to-one correspondence between material points within a reference image (initial unreformed image) and following images and configurations (subsequent deformed images). DIC processing involves taking small subsections (small groups of pixels) of the initial reference image to determine the respective locations within the current image. For each subset, a displacement and strain value is obtained through the subset location with respect with the previous image. The end result of this process shows the displacement and strain distributions for the ROI overlay, the values obtained are referred to as lagrangian displacements (change in material point) and strains (change in material length) [18].

Before using the program in MATLAB, the images are first batch processed in ImageJ, this is achieved through use of a macro to crop the images to the selected size. The files are taken from a source/input folder and cropped individually, the cropped images are created in a new folder as a tiff file. Figure 26 shows the first image before and after cropping.

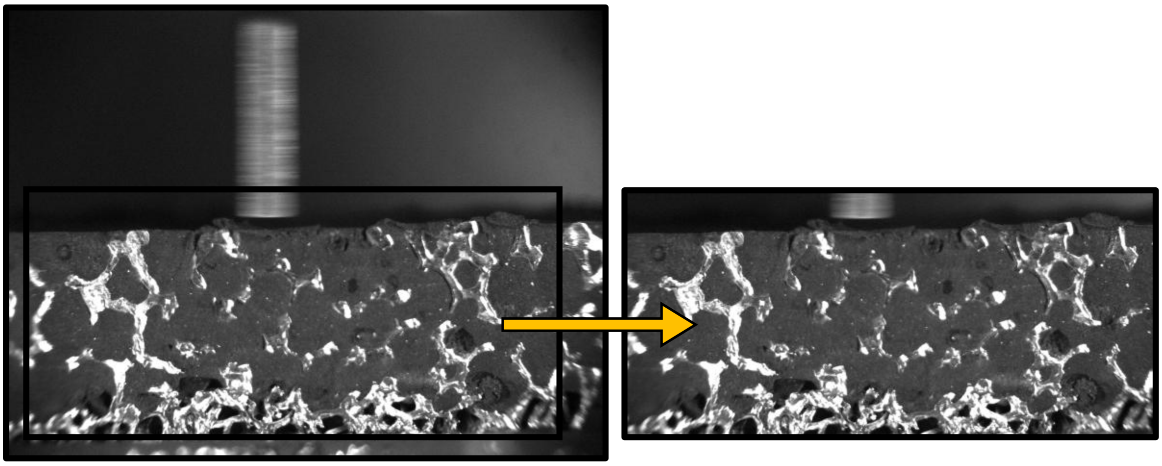

Figure 26. Cropping of required section in ImageJ as input for MATLAB programme

For the entire duration of the test, in total there were 500 – 2000 images captured, with this quantity is not possible to fully process a full complete DIC analysis for the entire test. However, a series of 50-100 images processed is still representative of the material behaviour and mechanics at the beginning, middle and end of the test.

After the images are cropped appropriately, the first image is uploaded into the MATLAB program, this first image is regarded as the reference image used for processing. Similarly the following images are uploaded to show the deformation process that occurs. Figure 27 shows the user interface once the images have been uploaded to the program.

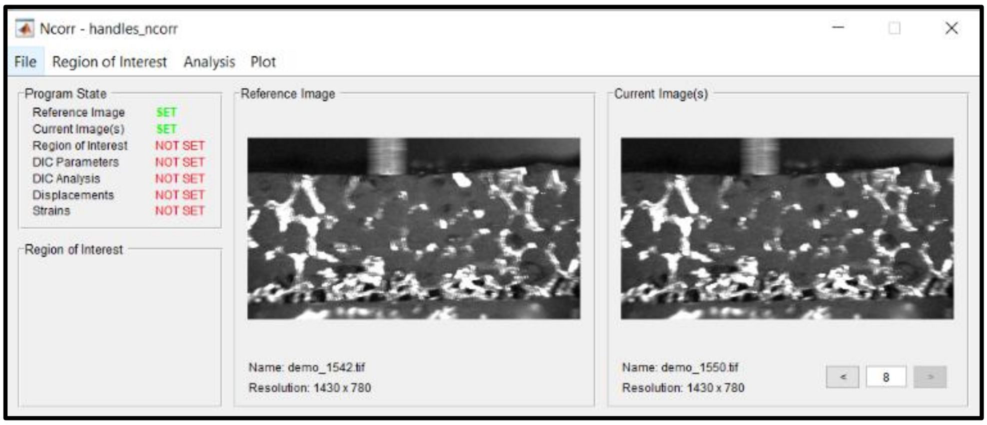

Figure 27. Upload of reference image and subsequent images to follow for processing

To reduce processing time and efficiency it is unnecessary to process the entire image for subsets (small groups of pixels) and pixel positioning, therefore a ROI is selected and drawn (Figure 28). This is selected to accommodate the focal region of the camera and is drawn and adjusted by hand with respect to the reference image, this ROI will be duplicated and analysed for the subsequent images to follow.

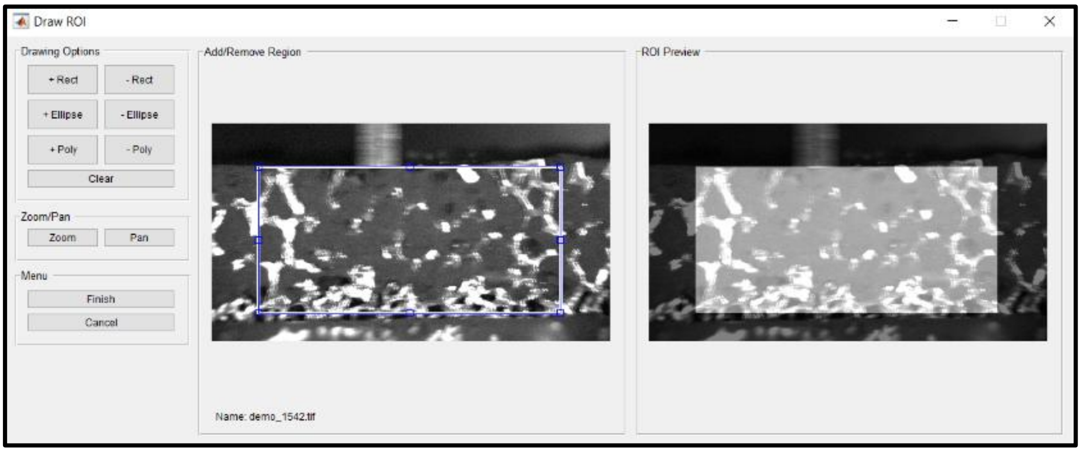

Figure 28. Selection of ROI for DIC analysis

After the ROI for processing has been appropriately selected, the DIC parameters need to be set for processing (Figure 29). Subset size and spacing is important depending on the material and size of deformation that occurs, for more noticeable deformation it is unnecessary to reduce the subset size and spacing as this will cause longer process time and show the same result. For analysis of metallic foams, it is important to highlight the filler and metallic phase deformation. A smaller subset and subset spacing can help to investigate movements within the filler polyester phase and potential load or energy transfer.

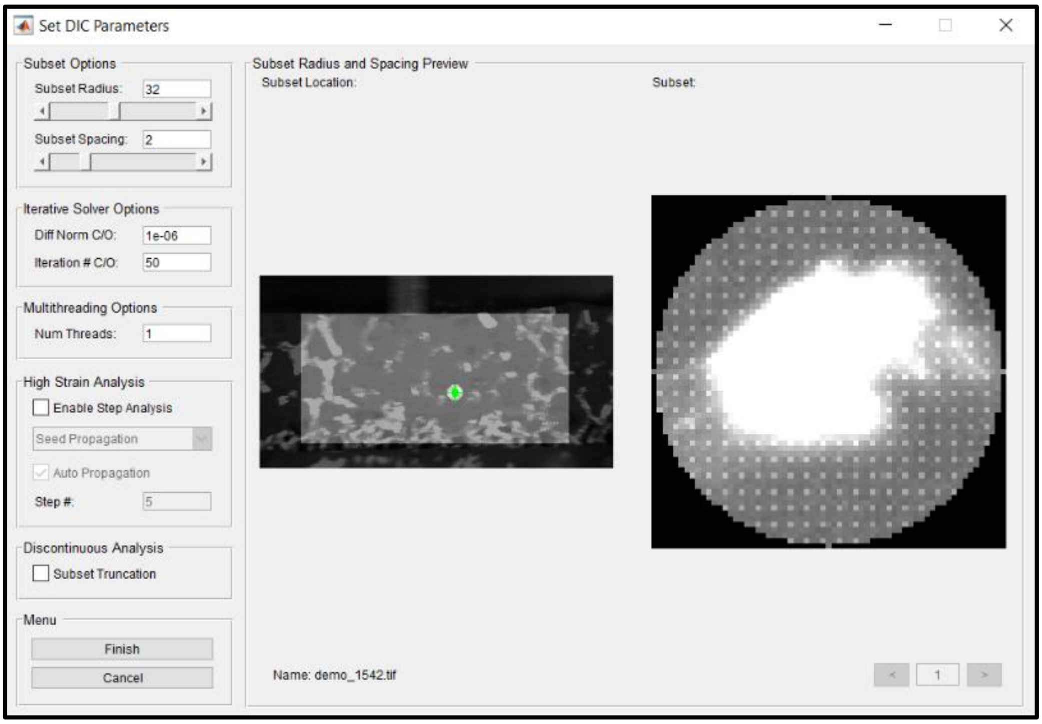

Figure 29. DIC parameters for image processing

Next is to select the subset size, a typical ligand point or region is selected and the analysis size is adjusted to accommodate it (Figure 29). An estimation can be determined of the location of the neighbour points in a deformed image, these are used to obtain the initial values of u and v displacements directly.

After the subset size has been set, the DIC analysis is run. Once DIC analysis has been completed displacements are formatted according to a set scale (Figure 30). A calibration image is uploaded, the dimensions of the blade tip are 20mm in length and 2mm wide. A line is set across the blade width, this measures the number of pixels along the line set and with the dimension input can calculate the size of each pixel. This is then applied to every single image that has been processed reassigning the displacement values obtained for both directions to the correct scale to obtain the appropriate readings.

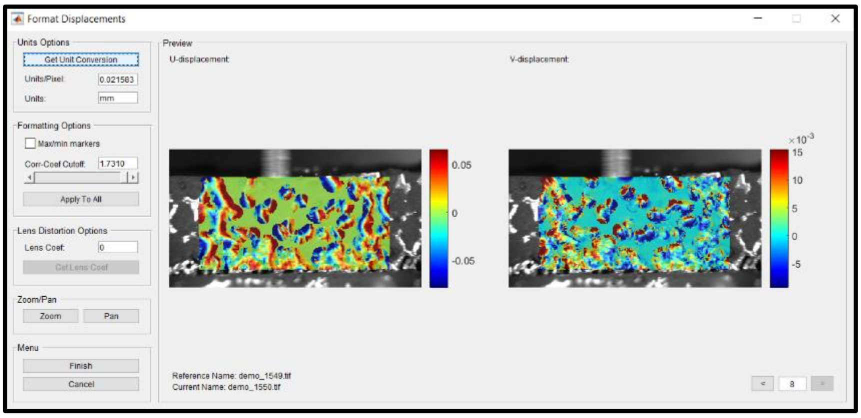

Figure 30. Displacement formatting and assignment of scale

Strain calculations are more difficult to resolve than displacements due to the fact that they involve differentiation and are incredibly sensitive to noise. These values of displacement are often noisy, they are smoothed before calculating the strain fields.

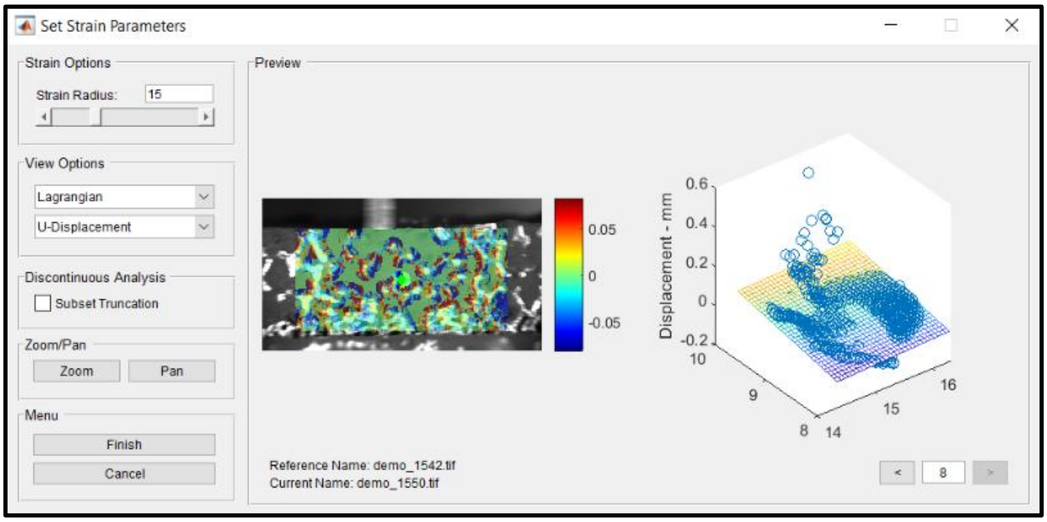

Figure 31. Strain calculation and assignment method

A strain window idea is used [33] to calculate strains, this makes use of the subset displacement data (u and v) in order to attain the length changes of certain features (Figure 31).

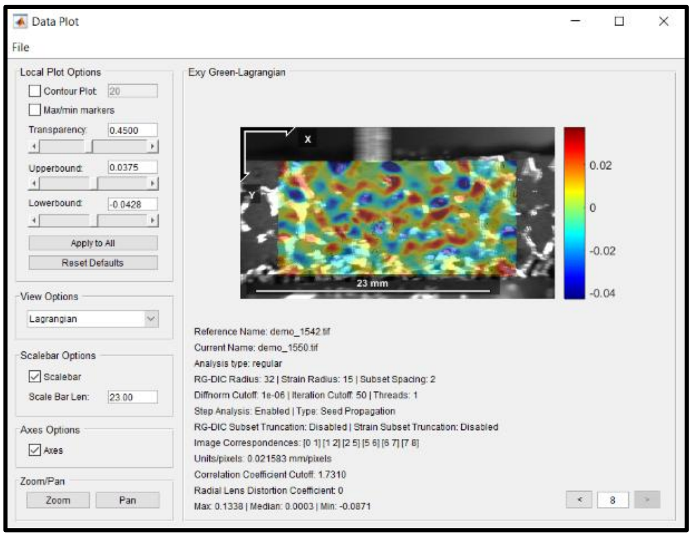

Figure 32. Overlay of strain distribution as end result of image processing

The strain distribution for every image is calculated and is overlayed onto the image, this helps to identify clearly how specific regions and phases behave (Figure 32). The final output shows this overlay with an example in Figure 32.

4.3 Sample Analysis

With rubs tests lots of the analysis involves observations of key features on wear marks or scars. Other interesting details can be found within the internal structure of the samples, for this cutting and sectioning of the substrate is necessary. High quality images are captured using scanning electron microscopy (SEM) and optical microscopy to be further evaluated.

4.3.1 Vacuum Impregnation

Prior to sectioning and imaging, the samples need to undergo further preparation. Metallic foams are incredibly porous. In order to retain the structure and prevent crumbling or breakage of the substrate when sectioning, vacuum impregnation has been used to fill the pores with epoxy resin. This keeps the internal structure intact during any sectioning or cutting procedures.

In order to impregnate the samples, a resin multi-step approach to common cold mounting is adopted. The resin and hardener kit in this project is commercially available and supplied by Struers called EpoFix. Typically the mounting cups for samples range between 25 – 32 mm in diameter, due to the substrate size being extensively larger, 3D printed cups are used to accommodate the bigger substrate size for cold mounting. The 3D printed cups consist of a flexible material commercially available as Poly-Propylene (PP).

The sample is placed into the mounting cup and the cup filled with resin. This is then carefully placed within a vacuum chamber, the seal is closed and the pump is turned on. The vacuum pump is switched on and left for half an hour, this ensures that the resin penetrates into the porous structure of the metal foams. The vacuum is then switched off and the resin is left to set overnight. This vacuum process is repeated again to ensure the substrate has been fully filled with resin. After which, the samples are ready for sectioning.

4.3.2 Material Characterisation

Optical imaging was taken of the wear scar and blade to record macro features observable from the samples, further observations are made using the SEM to observe microscopic features that occur during testing.

Characterisation of blade tips and abradable samples were carried out post-testing to observe phenomenon such as blade wear and adhesion and to identify cavities and pores within the abradable surface. Characterisation was achieved using scanning electron microscope (SEM, Hitachi TM3030) and an optical microscope (ZEISS Primotech).

Chapter 5

Open Cell Foams vs Filled Foams

5.1 Introduction

This chapter aims to investigate open-cell foams with a suitable comparison to filled foams; these initial tests are carried out to gain insight into how these open-cell porous foams behave abrasively.

The open-cell metallic foam samples were sourced and made commercially available by Recimat and Alantum. These two companies are renowned for their mass production of open-cell foams and consistent control over pore size. The manufacturing and production methods have been previously explained in detail in the literature review. The metallic foams used in this chapter are procured commercially and undergo quality control to ensure the nominal pore sizes are maintained at 1200 μm and 3000 μm in diameter. These pore sizes have been selected as they are comparable to those of honeycombs used in previous work conducted at the University of Sheffield - [31].

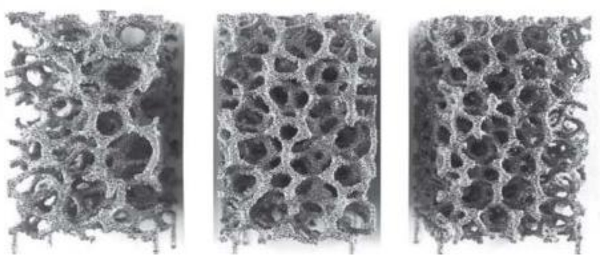

(a)

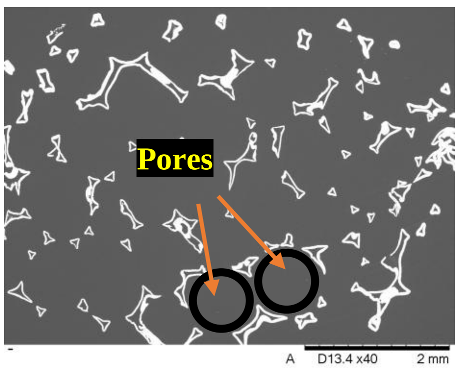

(b)

Figure 33. Sectioned partitions of open-cell foam (a) with a cross-sectioned SEM image (b)

The samples were sectioned before testing, and the pore size was confirmed to be 1200 µm, as shown in Figure 33. The partitioned sections were imaged using a high-quality camera, enabling the pores to be measured at approximately 1000 µm, as depicted in Figure 33a. This measurement was later validated through SEM imaging in Figure 33b, which consistently recorded a nominal pore size of approximately 1200 µm across the bulk material. Some EDS analysis indicated that the material composition also contained traces of Al, Fe, Zn, and Cu alloy powders for both Alantum and Recemat foams. Considering the differences in suppliers for these metallic foam constructs, the pore sizes are all remarkably similar, facilitating suitable comparisons. The role of these alloy powders is to enhance the thermal and chemical properties of the foam.

Open-cell foams are further compared to filled foams, where polyester resin is injected into these open-cell metallic foams. The literature review highlights a more detailed description of how this is achieved. In previous studies regarding abradable coatings, the addition of dislocator phases is common for solid lubrication purposes [15], [20], [34]. The aim of incorporating polyester resin to create a filled foam is to improve the abrasive performance and achieve better cutting.

5.2 Test Samples and Details

Table 2 shows the test matrix of samples and the different conditions under which the samples were tested.

Table 2. Test matrix for metallic foams investigation

Test	Abradable Material	Blade	Blade Tip Velocity (m/s)	Incursion Rate (µm/pass)	Incursion Depth (µm)
1	Filled Foam (3000 µm Pore Size)	Inconel 718	100	2	2000
2	Filled Foam (3000 µm Pore Size)	Inconel 718	100	0.2	2000
3	Filled Foam (3000 µm Pore Size)	Inconel 718	100	0.02	2000
4	Open-Cell Foam (1200 µm Pore Size)	Inconel 718	100	0.02	2000
5	Open-Cell Foam (3000 µm Pore Size)	Inconel 718	100	0.02	2000

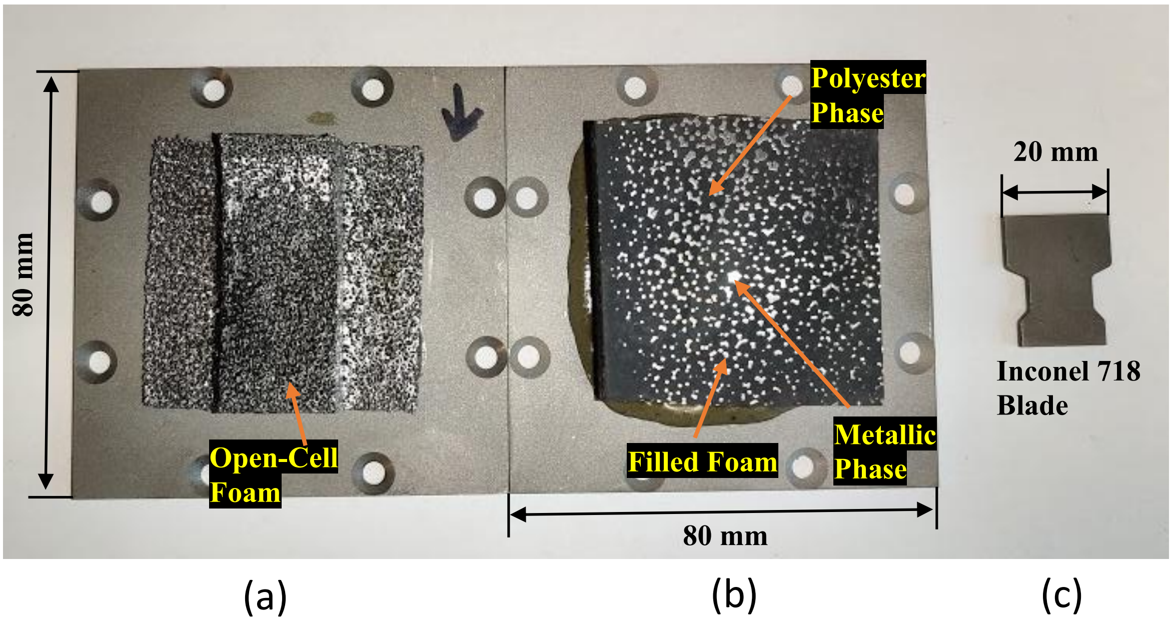

Figure 34. Test samples and blade used for testing showing open cell (a), polyester filled foam (b) including a typical test blade (c)

Filled foam substrates (Figure 34a) are metallic foam substrates with a polyester filler added into the open cellular pores, the metallic foam (Figure 34a). The polyester filler is mainly carbon based, however, for high temperature applications silicon has been added to enable high temperature performance and service life. The blade used was Inconel 718, which is a hard material and commonly used in the compressor stages for the blades. Inconel 718 consists of NiCr with small amounts of aluminium (Al), iron (Fe), molybdenum (Mo), niobium (Nb) and titanium (Ti).

The incursion rate represents the amount the stage moves the material per pass of the blade. For these series of tests the filled foam samples have varying incursion rates of 2, 0.2 and 0.02 µm/pass. Furthermore, a comparison was to be investigated of 0.02 µm/pass for filled foams with open-cell foams of different nominal pore size. The total incursion depth of all tests is 2000 µm. The 0.02 µm/pass corresponds to in flight running and 2 µm/pass corresponds to running and handling procedures carried out in the low and high pressure compressor stages.

In situ force and temperature measurements were taken, these in combination with blade and sample imaging gives a good idea of the wear mechanisms that occur during testing. Post-test imaging and DIC analysis were used to further identify failure modes within the substrate.

5.3 Results

Three comparisons were made in this study of foams that, when combined, can provide insight into the wear mechanisms and behaviours. These three comparisons include the pore size of unfilled foams, filled with unfilled foams, as well as incursion rates for filled foams.

5.3.1 Unfilled Foams - Effects of Pore Size at Low Incursion Rate

Figure 35 presents results from the test for small pore size (1200 microns) NiCr foam at an incursion rate of 0.02 µm/pass, characterising both the blade and the abradable, along with the forces experienced during the test. In contrast, Figure 36 shows results for larger cell size (3000 microns) NiCr foam under the same testing conditions. Figures 35D, E and 36D, E reveal a significant amount of blade wear for open cellular structures, as evidenced by optical images that illustrate the severity. The depth of blade wear is approximately 900 µm for NiCr 1200 and 400 µm for NiCr 3000; the larger pore size showing a lower wear depth; however, the test duration until fracture is considerably shorter. For larger nominal pore sizes, there is an increase in the severity of blade wear, which is a major concern that requires addressing and will be discussed further.

For both abradable samples due to the structure of the foam having open cell formation, the areas where metallic ligaments exist cause ridges to form within the blade when worn. SEM and optical images show these ridges. Due to larger struts and nominal pore size in NiCr 3000 the ridges formed are larger in width compared to that of NiCr 1200 as shown in Figures 35H and 36G,H. Figure 35G shows an image where the compaction of the metal foam can be clearly seen, many of the open cellular regions have fractured and are compacted together.

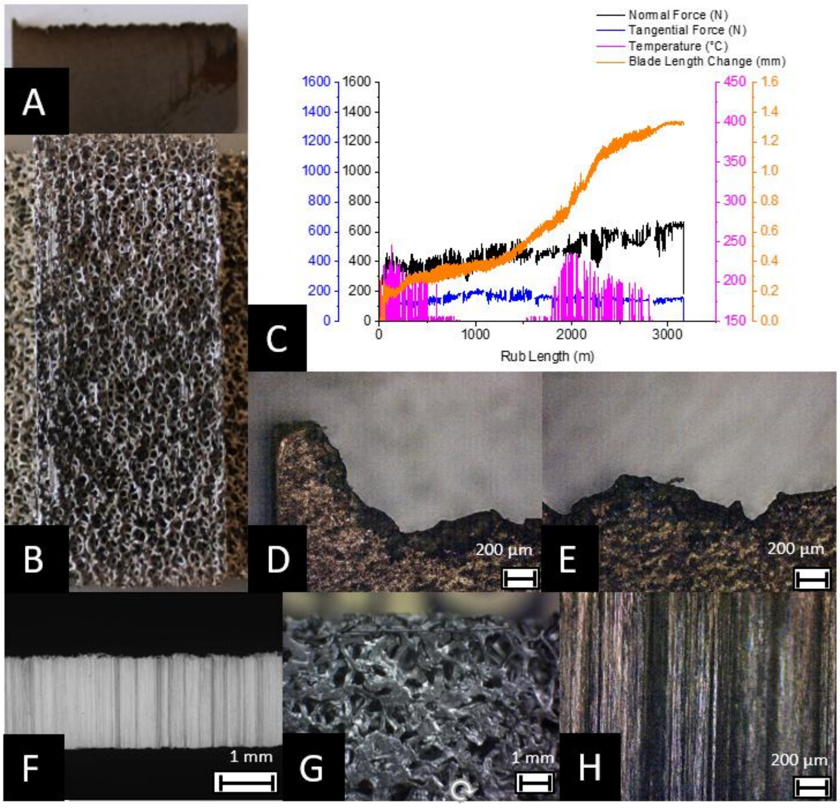

Figure 35. Open-Cell foam (1200 µm pore size) at an incursion rate of 0.02 µm/pass showing examples of the side view of the blade (A) and top view of abradable (B) samples, force, temperature and blade length change (C), optical post-test blade wear from side view (D,E), top view SEM blade tip surface (F), stereoscopic image of abradable post-test (G) and optical image of blade tip surface - top view (H)

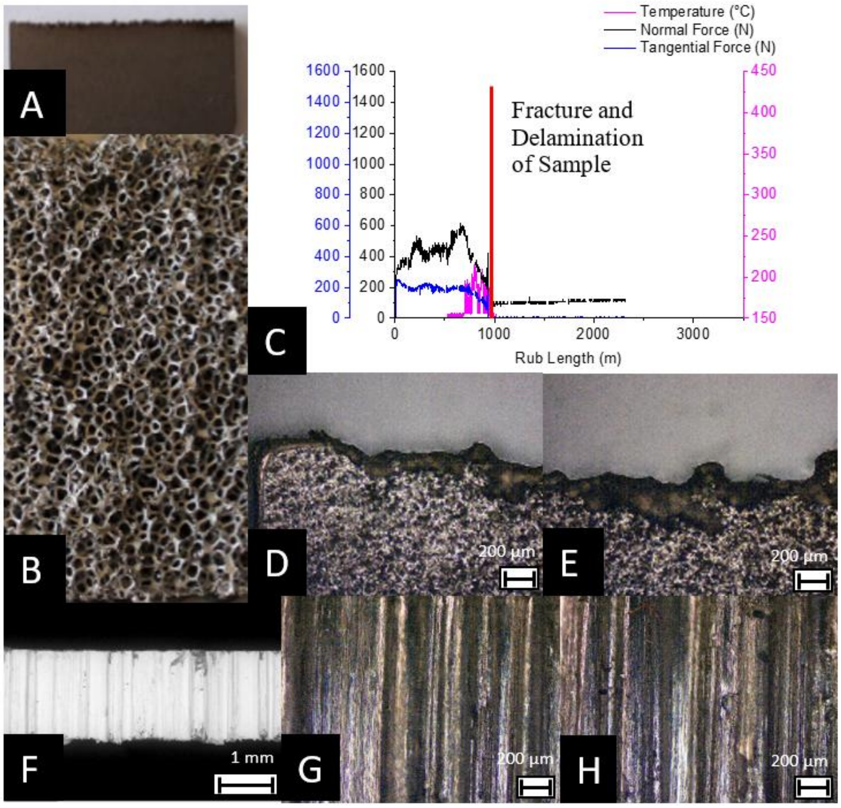

Figure 36. Open-Cell foam (3000 µm pore size) at an incursion rate of 0.02 µm/pass showing examples of the side view of the blade (A) and top view of abradable (B) samples, force, temperature and blade length change (C), optical post-test blade wear from side view (D,E), top view SEM blade tip surface (F), optical image of blade tip surface – top view (G,H)

The forces for small and large nominal pore sizes are shown in Figures 35C and 36C. The tangential force experienced is greater for a larger nominal pore size. The metallic struts are larger, as seen in Figures 35B and 36B, and thus require more force to remove; for smaller pore sizes, the relative metallic struts are smaller and therefore less force is needed to break and fracture these from the rub surface. The normal force for NiCr 3000 is greater in comparison to NiCr 1200, implying less compression and more violent wear of the two components. A smaller normal force for NiCr 1200 indicates that it is easier for the ligaments to plastically deform out of the way, leading to compaction of the abradable material. This is due to the force being absorbed upon impact by the metallic struts within the top rub surface or breaking earlier.

Observing the rub area, which has an uneven morphology, Figure 36B shows areas of missing material in the abradable material surface. This results from the dislocation and fracture of metal ligands, causing areas to delaminate and break off near the subsurface. From the imaging and characterisation, it is clear that a large amount of material is removed, as well as a substantial amount of blade wear, which explains the deep ridges captured in side views shown in Figures 36D and 36E. The eventual delamination of the extruded rub area results in the discontinuation of the test, as shown in Figure 36C. Stress accumulation from the force applied by the blade, which localises in the metallic struts, is a point of interest, detailed fully in the discussion.

It should also be noted in the results that the pyrometer measures temperature based on the emissivity of the metallic phase over a small region of the blade path. At times, the temperature appears to rise instantaneously, as seen in small peaks in Figures 35C and 36C; this is caused by the pyrometer detecting sparks from contact. Furthermore, the pyrometer has a measuring range of 150-1000°C. Therefore, any temperature below this range is measured as 150°C.

5.3.2 Comparison of Filled to Unfilled Foams at Low Incursion Rate

A comparison is created of the impact fillers have on the breakdown mechanics and behaviour of the metallic foam structures. This is through comparing two separate samples, one of which is NiCr 3000 unfilled foam (open-cell foam) and the other a NiCr 3000 foam with polyester filler present (filled foam). The incursion rate for both tests is the same and was tested at 0.02 µm/pass to provide a suitable comparison of how they behave with and without filler material.

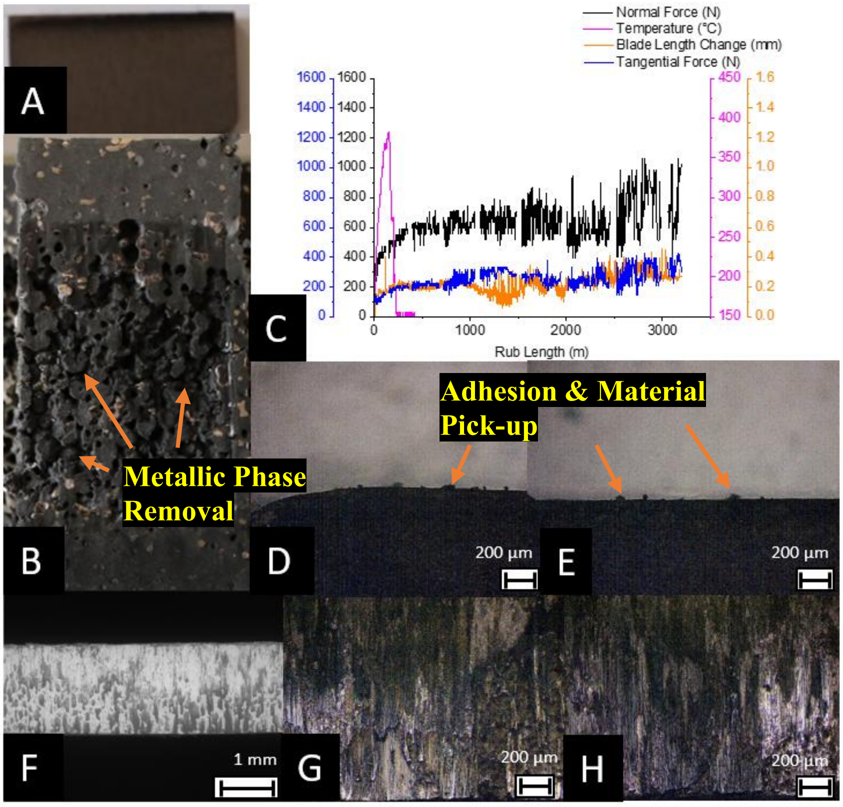

Figure 37. Filled foam (3000 µm pore size) at an incursion rate of 0.02 µm/pass showing examples of the side view of the blade (A) and top view of abradable (B) samples, force, temperature and blade length change (C), optical post-test blade wear from side view (D,E), top view SEM blade tip surface (F), optical image of blade tip surface – top view (G,H)

Figure 37 shows the results for a filled foam, it shows characterisation of the blade and abradable as well as forces experienced during the test. The top contact surface in Figure 37B shows a large amount of empty pores, the metallic phase is seen to be removed during the test. The abradable material seems to show good compaction upon contact which is a desired property. Compaction means that the abradable material becomes concentric to the blade path.

From Figure 37C the tangential and normal forces recorded are identified to be larger for a filled foam in comparison to an open-cell foam, when considering the tangential force the contact surface area is greater and therefore more cutting resistance force exists, the struts are also more supported through presence of filler meaning they do not deflect. The temperature experienced with filler can peak up to approximately 400°C generating a lot more heat, for open cell foams 250°C which generated less heat.

Figure 37A shows that with filler material there is little to no blade wear, however, there is more material pick-up and adhesion. The optical images Figure 37D,E show that material pick-up exists as a thin layer covering the blade tip, small areas exist where the debris formation is seen as small fragments of filler attached. The SEM image in Figure 37F indicates the location of the debris pick-up and adhesion to the blade. The upper part of the blade is the leading edge, most of the pick-up can occur along the trailing edge of the blade as it passes across the sample.

For an incursion rate of 0.02 um/pass, a lot of metal phase from the near surface is removed suggesting the ligands have been pulled out as shown in Figure 37B. Due to this loss of metallic phase, the remaining material revealed at the surface was the filler. Polyester filler has a low emissivity and is not picked up by the pyrometer as having any temperature. This, in turn, explains the sudden drop in temperature seen in Figure 37, where there seems to be no apparent temperature data following this anomaly.

Little blade wear is seen through optical imaging of the blade tip face indicated in Figure 37G, H. A few minor chips and breakdowns are from the recast layer, resulting from the manufacturing process. The darker areas illustrate where the filler has adhered to the blade tip surface.

5.3.3 Effects of Incursion Rate on Filled Foams

Incursion rate was varied to identify the effect it has on the breakdown mechanism of filled metallic foams. 0.02, 0.2 and 2 μm/pass was compared and the other testing parameters were kept the same for a suitable evaluation. In Fig 39C and 40C is the force, temperature and blade length change profile during the test for 2, 0.2 μm/pass respectively, the results for 0.02 μm/pass incursion can be seen in Fig 37C.

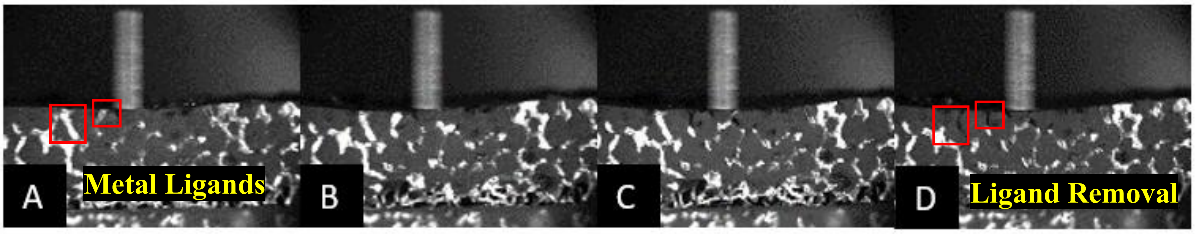

Figure 38. Evolution of material pull out phenomenon captured by bottom camera for a filled foam (3000 μm pore size) at a 0.02 μm/pass incursion rate

Figure 38 shows a series of images where the material is pulled out of the top surface and the evolution of how it occurs. This process is most apparent at lower incursion rates as energy input is low and often several passes are required to remove a ligament.

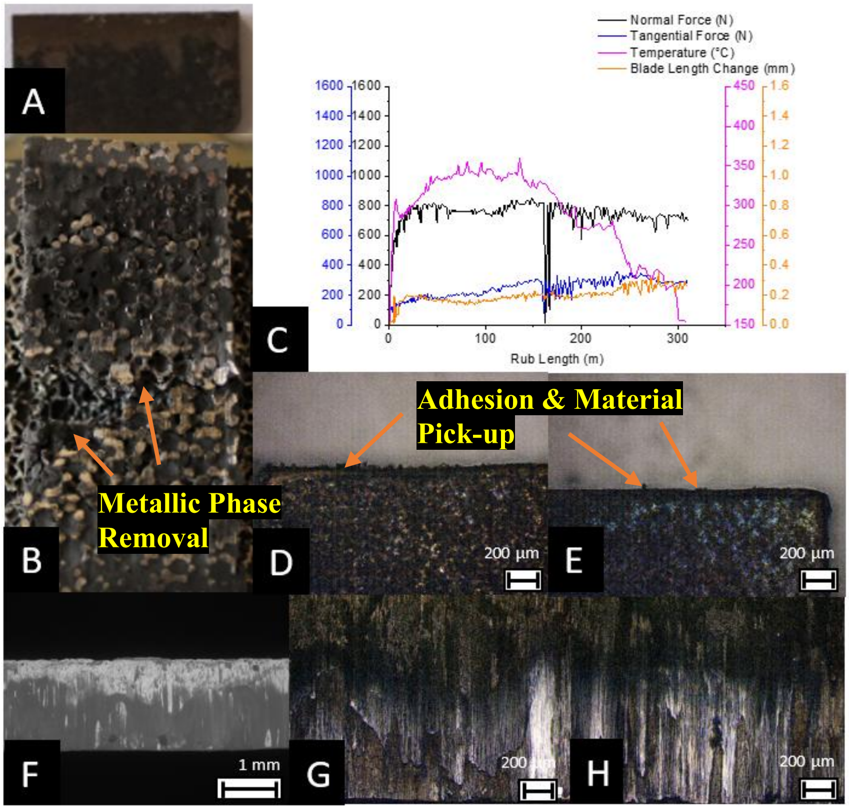

Figure 39. Filled foam (3000 µm pore size) at an incursion rate of 0.2 µm/pass showing examples of the side view of the blade (A) and top view of abradable (B) samples, force, temperature and blade length change (C), optical post-test blade wear from side view (D,E), top view SEM blade tip surface (F), optical image of blade tip surface – top view (G,H)

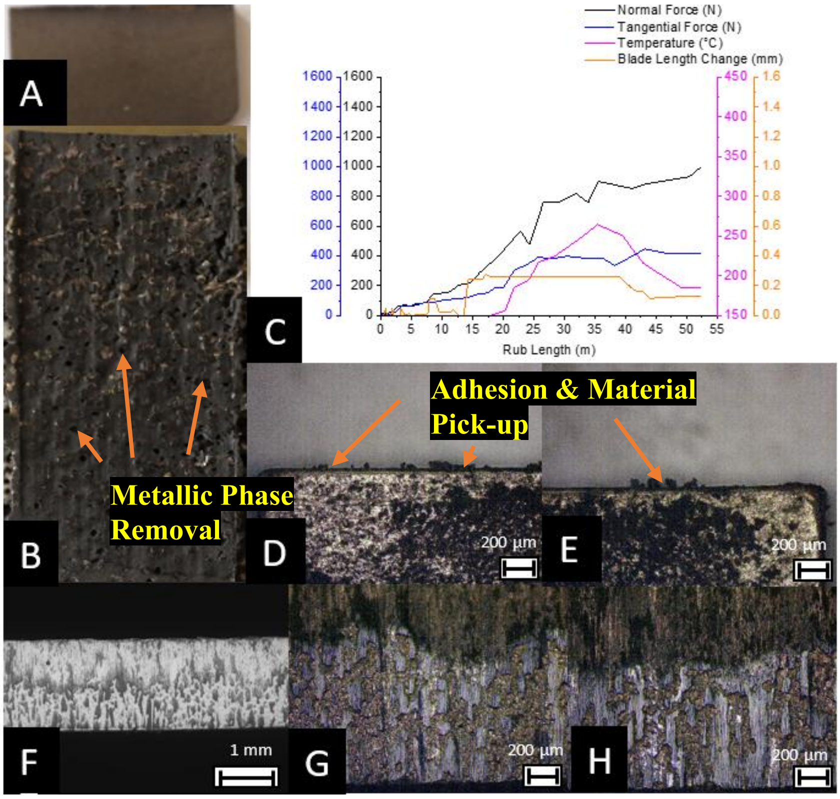

Figure 40. Filled foam (3000 µm pore size) at an incursion rate of 2 µm/pass showing examples of the side view of the blade (A) and top view of abradable (B) samples, force, temperature and blade length change (C), optical post-test blade wear from side view (D,E), top view SEM blade tip surface (F), optical image of blade tip surface – top view (G,H)

Figure 40 illustrates the results for NiCr foam at 2 μm/pass. The pick-up is very low; however, when applying factors of 10 and 100 to the incursion rate, the incursion rate decreases to 0.2 and 0.02 μm/pass, respectively, leading to an increase in pick-up as shown in the images in Figure 39 and 40, particularly noted on the blade tip surface. At higher incursion rates, the rub surface exhibits a smoother morphology with less material pull-out. The average and maximum forces acting on the abradable sample are quite similar between the tests in both shear and normal directions; however, the wear mechanics and final morphology differ significantly. A key point of discussion is why differing incursion rates result in variations in morphology.

The particle adhesion is more evenly distributed at smaller incursion rates, such as 0.2 and 0.02 μm/pass, where the optical images in Figures 37D and 39D indicate that the debris pick-up forms a more uniform layer spread across the blade surface, and the particle size remains relatively consistent. Conversely, when the incursion rate increases to 2 μm/pass, Figures 40D and E reveal that minimal material adhesion occurs, alongside sporadic locations and sizes of debris formation.

Material pull-out of the filler phase from the metallic phase is a phenomenon often observed in filled foams, and it becomes more severe at lower incursion rates. This issue necessitates further investigation, as significant material pull-out results in an uneven sealing surface, which is undesirable. As the filler material is softer compared to the metallic phase, when a shear force is applied, the filler phase loosens, thereby exposing the metallic phase at the top surface, allowing the blade to pass through and remove it with ease.

At higher incursion rates more damage is seen to the recast layer along the blade tip as shown in Figure 40G,H in comparison to Figure 37G,H, at higher incursion rates there is more force upon contact between blade and abradable sample. From the post-test characterisation seen in Figure 37B, 39B and 30B higher incursion rates create a smoother wear surface as well as less material pull out.

5.4 Discussion

As highlighted, further analysis of the abradability of foams is required, this discussion includes the breakdown mechanics and deformation upon interaction between the blade and abradable analysed in more detail. A comprehensive understanding is needed to design the best structure and composition for consistent abradable performance. There are three main points of discussion which include effects of pore size on unfilled foams, impacts of filler added to open cell foam structures and effects of incursion rate.

5.4.1 Unfilled Foams - Effects of Pore Size at Low Incursion Rate

As noted previously, significant blade wear was observed for the unfilled foams. The reason behind this wear can be investigated by further processing the images captured of the foam using a DIC technique to look at how strain is generated, specifically at the compaction of the surface.

Figure 41 shows a series of images with the DIC processing overlayed, showing the localisation of strain accumulation within the top contact surface. These series of images were taken over the initial stages of the rub at equal time intervals of half second intervals; the strobe timing ensured that each image was captured after each blade passed.

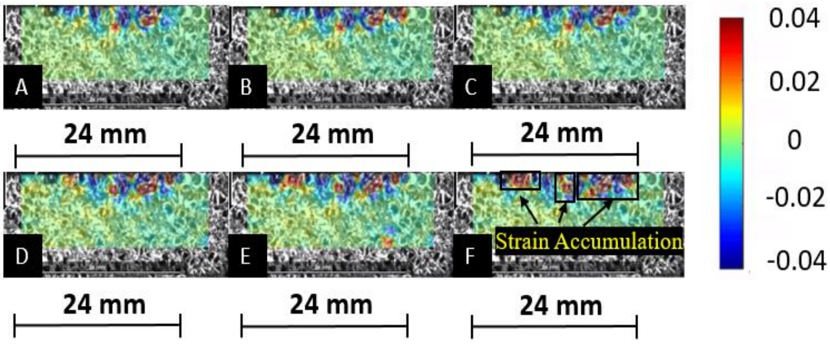

Figure 41. Evolution of strain localisation within the top rub surface for an open-cell foam (1200 µm pore size) 0.02 µm/pass – blade pass direction is from left to right – images taken half a second apart

Significant strain localisation and accumulation in the top rub surface this indicates that blade wear will always occur, as the metallic foam is NiCr composition and has relatively high hardness, and when subject to shear force this can require a large amount of force to remove and so wear into the blade is a result of this.

It is also interesting to note that the strain accumulation can be seen to vary dependant on position within the arc of contact. For example in Figure 41 the strain accumulation can be seen to amass in two main locations. Towards the left side where the blade first enters contact, strain accumulation can be seen, similarly at the exit of contact.

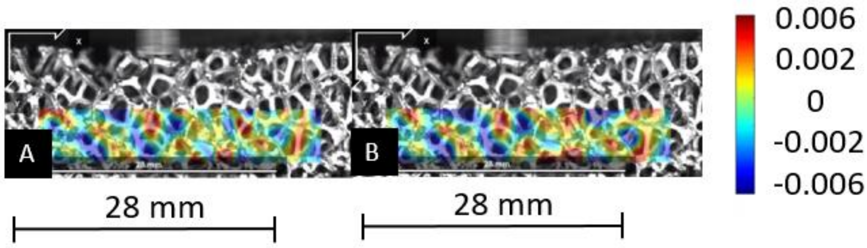

Figure 42. Evolution of strain accumulation in the bottom section of the abradable for an Open-cell foam (3000 μm pore size) at an incursion rate of 0.02 μm/pass – blade pass direction is from left to right – images taken half a second apart

The locations where stress and strain build up is clearly pinpointed within a larger pore size structure since the metallic struts can be identified more easily as shown in Figure 42. Open cellular foam structures always have two outcomes, significant wear of the blade or significant wear of the abradable. For large pore size the number of interconnecting struts within the base is significantly less in comparison to a smaller pore size foam, if any of the major ligament support structures break and get removed the structural integrity becomes weak and ultimately leads to break away.

For the larger foams, significant fracture occurs at the surface with a compactive built-up layer starting to occur before the material ultimately breaks away, bulk densification of the material is small and more fracture occurs. Given that all occurs within the locality of the surface, high surface forces and blade wear are observed. Comparing now the DIC for the finer foams, it is seen that less compaction occurs and more fracture occurs on a strike-by-strike basis, meaning that lower forces occur and the material does not wear the blade as much; however, this is still enough for some wear. The stress and strain localisation in the top rub surface for unfilled foams implies a lack of energy absorption and transfer.

As such the pore size directly influences which component wears and is damaged between the blade and abradable. With larger nominal pore size the metallic struts are larger in size, these metallic struts are stronger individually in comparison to a small nominal pore size metallic foam. The strut density, however, for larger nominal pore size is significantly reduced, in turn the spatial differences are larger between interconnecting struts this promotes a fracture mechanism where the joining struts break apart. More violent wear is thus noted for the larger nominal pore size since less compaction occurs. Conversely, for a smaller nominal pore size the fracture occurs only at the surface and more densification and compaction is noted seen in Fig 35G, this results in wear of the blade and no transfer within the abradable material. For unfilled foams of smaller size, compaction can occur as well as violent wear. It is not feasible to have open porous structures due to the excessive blade wear, this will cause low performance and minimal component lifetime as well as large amounts of debris formation in the form of fractured large metallic ligaments.

5.4.2 Impact of Filler to Open Porous NiCr Foam

Conversely, blade wear did not occur for filled foams, and the behaviour is broadly similar at all incursion rates. In this section, the overall mechanics of filled metallic foams are discussed before moving on to the next section to consider subtlety in response to incursion rate. As filled foams exhibit better cutting with minimal to no blade wear, DIC is used to understand the results further.

When a filler is present it can be seen that two things occur. Firstly it allows a degree of bulk load transfer to occur where the abradable is able to deflect and move away from the incurring blade, additionally the filler also holds the ligaments in place where a component of the blades energy also leads to ligament fracture. These two mechanisms happen together where a fraction of load transfer and a degree of breaking occurs, and combined mean that a compactive layer no longer occurs at the surface and blade wear can be avoided.

Filler material is therefore useful to help absorb and dissipate energy from the blade impact, and the main role of DIC processing is to identify failure regions of high stress and understand how the filler impacts the behaviour and response of the metallic foam structure. This highlights how fillers are important due to their capability to promote load transfer. A good example of this load transfer is shown in Figure 43 for an incursion rate of 0.02 μm/pass where it can clearly be seen that the filler absorbs the energy and transfers the load through the sample, and repetition helps reduce the breaking of the metallic phase by absorbing the energy upon impact of the blade. In comparison to open-cell foams there is no strain localisation and very little variation in strain across the whole sample, this suggests little deformation across the sample and thus supports the claim that the energy is absorbed by the filler material.

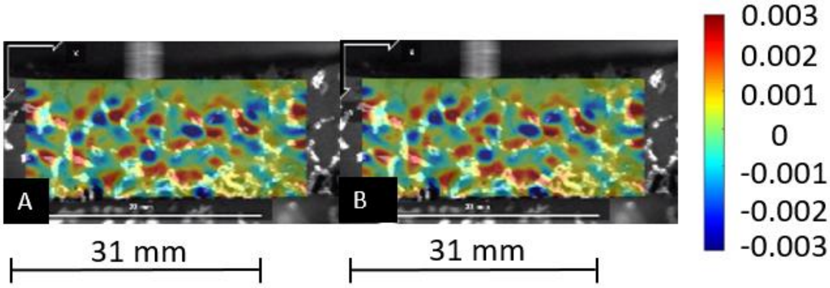

Figure 43. Evolution of strain distribution in the abradable sample for Filled Foam 0.02 µm/pass - blade pass direction is from left to right – images taken half a second apart

Areas of large strain and buckling occur where small regions of filler are surrounded by neighbouring metallic struts/ligaments, and a large impact force from the blade contact can cause the metallic phase to loosen within the entire structure. Without the presence of filler material the strain accumulates in such areas. The filler helps to reduce the severity of this phenomenon, however, long term solutions will need to be implemented to avoid or control the filler distribution. Figure 44 shows a good example of where the effects of open pores and uneven distribution or lack of filler is present, leading to large strain accumulation followed by breaking away and formation of large cavities. This highlights the importance of filler evenly distributed within the metallic foam structure.

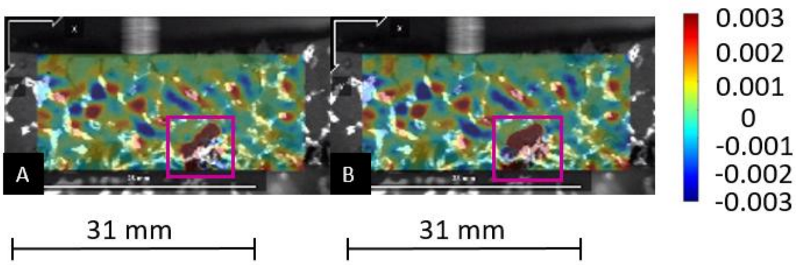

Figure 44. Evolution of strain build up when lack of filler for Filled Foam 0.02 µm/pass - blade pass direction is from left to right – images taken half a second apart

As such a good load transfer mechanism requires an evenly, well distributed amount of filler in the NiCr metallic foam structure. Figure 44 shows an example of where the strain accumulation builds and will ultimately end in fracture and damage to the abradable. The evolution of strain accumulation can be captured in these two frames, in these circumstances this can cause delamination of the abradable sample. This clearly highlights the importance of the filler to better promote the load transfer mechanism to prevent blade wear and significant damage to the foam.

5.4.3 Cutting at Various Incursion Rates

Moving on to consider the effect of incursion rate on filled foams, the post-test rub surface observed through macroscopic techniques in section 5.3.3. effectively shows this. Higher incursion rates promote more load transfer and more actuation of these positive mechanisms. Noted in the previous sections load transfer and ligament fracture were observed for all the filled foams to a degree however there were some subtle variations observed with incursion rate.

Chips and small shallow cavities are identified in the rub surface for smaller incursion rates, this is due to a lack of energy input to the system and more strain accumulation within the surface compactive layer. At the lowest incursion rate of 0.02 μm/pass there is a reduced amount of load transfer and actuation of this mechanism, this ultimately leads to some material pull out of the metallic ligaments.

The filler material is relatively soft in comparison to the metallic phase and blade. The longer test duration time for slower incursion rates such as 0.02 μm/pass means the abradable sample has taken more impact hits from the blade. The filler phase can easily loosen up and dislocate to reveal the bare metal ligaments which are thus removed as the blade impacts further. This is mostly seen at slower incursion rates which is shown by the rub surfaces in Figures 37B, 39B and 40B.

Previous studies on abradable materials show high forces with significant damage to the blade and sample with many inconsistencies in how the abradable behaves each test [27], [30]. In comparison these filled foam tests show excellent properties with consistently lower forces by a factor of 2 to 3 with little blade damage in comparison to thermally sprayed abradable coatings. Furthermore, these studies have shown excessive adhesion from abradable to blade with high temperatures where thermal marks are evident. These filled foams show little temperature variation and no thermal marks along the rub surface.

5.5 Conclusion

These metallic foams tests has been performed to investigate the wear mechanisms and breakdown behaviour during rub tests between the abradable sample and blade. The abradable samples are tested under varied incursion rates of 0.02, 0.2 and 2 μm/pass for open-cell metallic foam structures. Tests performed at higher incursion rates were found to cut better with less adhesion formation along the blade tip face, however the uniformity of this adhesive layer is very poor in comparison to lower incursion rates. Further testing will help to confirm this and provide some more understanding of how the adhesion forms and how this impacts the abradable structure.

In unfilled foams larger pore size results in more severe blade wear and abradable damage, some compaction is seen within smaller pore size, however. still a significant amount of damage to both components. Filler materials are able to prevent large strain accumulations within the metallic phase of the foam abradables, this helps the foams to perform suitably when worn with minimal blade wear and good compressive behaviour. The load transfer capability for fillers helps to transfer energy and distribute this evenly within the abradable structure, DIC imaging shows great contrast and comparison between filled and unfilled foams to identify where the strain accumulation occurs, and how this correlates to material behaviours such as fracture and crack propagation.

These results show that knowledge of the wear mechanisms in this series of rub tests provides initial insight and understanding of the rubbing forces and wear properties of metallic foam structures. Further work from this group will focus on understanding the actuation of these wear mechanisms and how to take advantage of these which is essential for investigating the feasibility of metallic foams, also a good consideration would be to use filler materials that can withstand higher operating temperatures.

Chapter 6

Polyester Resin Filled Foam Tests

Open cell foams exhibit local stress and strain accumulation within the top ligand layers, for filled foams a load transfer mechanism exists where shock and energy absorption which subsequently results in less damage to the sample and abradable. This load transfer mechanism has been identified within Chapter 5, however, more investigation is necessary to understand the role of both filler and foam in how such a mechanism is actuated.

Filled foams as seen in Chapter 5 show promise where the abradable substrate manifests the ability to actuate load transfer globally through the abradable structure, this allows for uniform deformation and an evenly distributed load throughout the abradable sample. In order to optimise these foam abradables, a series of tests were required to be carried out to investigate their performance. These were planned to replicate in engine-like conditions to understand further the key properties that influence load transfer in filled foam substrates.

This investigation assessed three main criteria that directly influence the behaviour of the filled foams during rub events. First of all the relationship between incursion rate on the cutting performance of filled foams is essential, abradable samples must not only perform well at the faster incursion rates, but also at the lower incursion rates. Additionally the filler density must be investigated, a desired global stiffness of the abradable structure is important since it is likely to result in excellent cutting. Filler density influences the global stiffness of the metallic foam and filler combination, in this instance two different filler densities are tested. Lastly the effects of incursion rate and its influence on cutting performance, these three criteria all play the same role in which they are all altering the amount of energy going into the system.

For compressor stage sealing the metallic foam and filler combination must be operable at temperatures of 200 °C in the lower stages of the compressor and up to 550 °C towards the latter stages of the compressor. In order to assess the feasibility filled foam abradable samples have been thermally aged under different temperature conditions for a fixed amount of time to investigate the thermal capabilities of such a combination of foam and filler.

6.1 Test Samples and Details

Filled foams consist of a polyester resin filler which is impregnated into a metallic foam substrate to create an abradable bulk material. The metallic foam framed structure is commercially available as Recemat BV under the trade name NC1116 consisting of NiCr with some additional metallic powders sintered into the metal ligands as part of the manufacturing process. This metallic foam framed structure is the same as used in the previous chapter for the filled foams.

The mechanical properties of the polyester resin filler can be changed by adjusting the glass fibre density within the filler. Glass fibre is often added to polyester resin to enhance impact resistance as well as improve durability and most importantly enhance the operable temperature [34][35]. Similarly the glass fibre in form of silica (SiO_2) particles was added into the resin mixture which is injected into the metallic foam. The tests conducted in the previous chapter used the same filler at a filler density of 20%.

In order to assess the samples across the three main criteria stated earlier, an extensive amount of testing was necessary to determine for each parameter how it directly influences the rub and wear mechanisms. Table 3 shows the test matrix and series of tests carried out with the independent variables as the tip speed, filler density, incursion rate and ageing temperature.

Table 3. Test matrix with all tests conducted using Ti Blades to a standard incursion depth of 2000 μm

Test ID	Material	Filler Density (%)	Incursion Rate (μm/pass)	Tip Speed (m/s)	Thermal Exposure (°C)	Ageing Time (h)
1.1	Filled Foam	10	2	100	N/A	N/A
1.2	Filled Foam	10	2	200	N/A	N/A
1.3	Filled Foam	10	0.02	200	N/A	N/A
2.1	Filled Foam	20	2	100	N/A	N/A
2.2	Filled Foam	20	2	200	N/A	N/A
2.3	Filled Foam	20	0.02	200	N/A	N/A

3.1	Filler Only	10	2	200	N/A	N/A
3.2	Filler Only	10	0.02	200	N/A	N/A
3.3	Filler Only	20	2	200	N/A	N/A
3.4	Filler Only	20	0.02	200	N/A	N/A
4.1	Filler Only	10	2	200	250	100
4.2	Filler Only	20	2	200	250	100
4.3	Filler Only	10	2	200	300	100
4.4	Filler Only	20	2	200	300	100
5.1	Filled Foam	10	2	200	250	100
5.2	Filled Foam	20	2	200	250	100
5.3	Filled Foam	10	2	200	300	100
5.4	Filled Foam	20	2	200	300	100

6.2 Results

6.2.1 Unaged (As Manufactured)

Polyester-filled foams are manufactured such that the metallic foam porosity uniformity is homogenous, this can be seen through a cross-sectional SEM image. Results will be presented to establish a clear relationship between speed with incursion rate to show the differences in material behaviour under such changes in test conditions.

6.2.1.1 Foam Wear Behaviour with Respect to Incursion Rate and Tip Speed

As seen previously in Chapter 5, polyester-filled metallic foams show representative wear mechanisms similar to traditional abradable materials, furthermore this deformation behaviour is actuated at the lower blade tip speed of 100 m/s.

Figure 45 shows the results for a filled foam abradable sample tested at the high incursion rate of 2 µm/pass with a 10% filler density under the lower blade tips speed of 100 m/s. The rub surface post-test shows signs of excellent cutting where the surface can be seen to be very smooth especially in the central area of rub, it should be noted however that the surface morphology shows open pores likely to have held metallic ligands of the metallic foam structure. During the rub event it is likely that as a result of the blade to abradable contact these

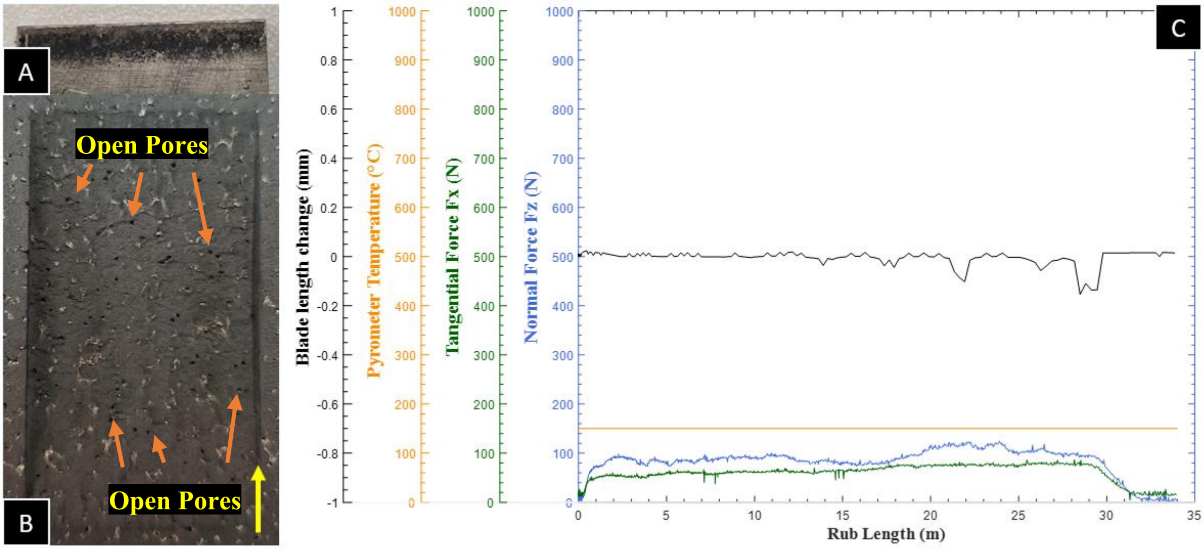

Figure 45. Test 1.1 (Filled Foam – 10% Filler Density – 2 µm/pass – 100 m/s) Post-Test Data A) Blade Tip B) Abradable Surface C) Force, Temperature, Blade Length - Graph

ligands have been pulled out and removed from the abradable structure. From previous foam tests in Chapter 5 a common phenomenon seen for filled foams is ligand pull out, subsequently the open pores in the rub surface post-test in Figure 45B. The blade surface in Figure 45A shows little signs of abradable adhesion or damage, whereas the calculated blade length change shows some variation which is likely not the case from a visual perspective.

Additionally the forces measured during the rub event prove the compliance and excellent cutting behaviour of the filled foam substrate, with a consistently low force trace with no sudden variations it can suggest that the sample cuts efficiently with little resistance. Typically for abradable coatings the forces are significantly greater than those seen in Figure 45C [36]. These significantly smaller force traces such as seen in Figure 45C are likely to suggest that there is an energy removal mechanism during the rub test, as such this would account for the excellent cutting and little abradable substrate damage also shown in Figure 45B.

Moreover it should be noted that the pyrometer reading of temperature shows a constant measurement of 150 °C, this implies that the surface spot temperature recorded does not exceed this value since this is the minimum temperature measurement the pyrometer can identify.

For the next test the same conditions as the first, however, at an increased tip speed of 200 m/s. Typically in engine like conditions the blade tip speeds are faster, to replicate these conditions the test rig is operable to 200 m/s.

The rub surface in 46B shows overall a well cut surface with no observable damage to the substrate and a smooth region at the leading edge, however in this instance tear marks can be seen to have developed along the rub surface. It is likely for this test a different mechanism exists, with a well cut rub surface shown in Figure 46B it is likely that there is additional load transfer. In this instance the resin filler material shows signs of tearing along the rub path with minimal signs of material pull-out, although at the same time no signs of blade wear can be seen through the blade length change plotted and furthermore visually from the blade tip in Figure 46A.

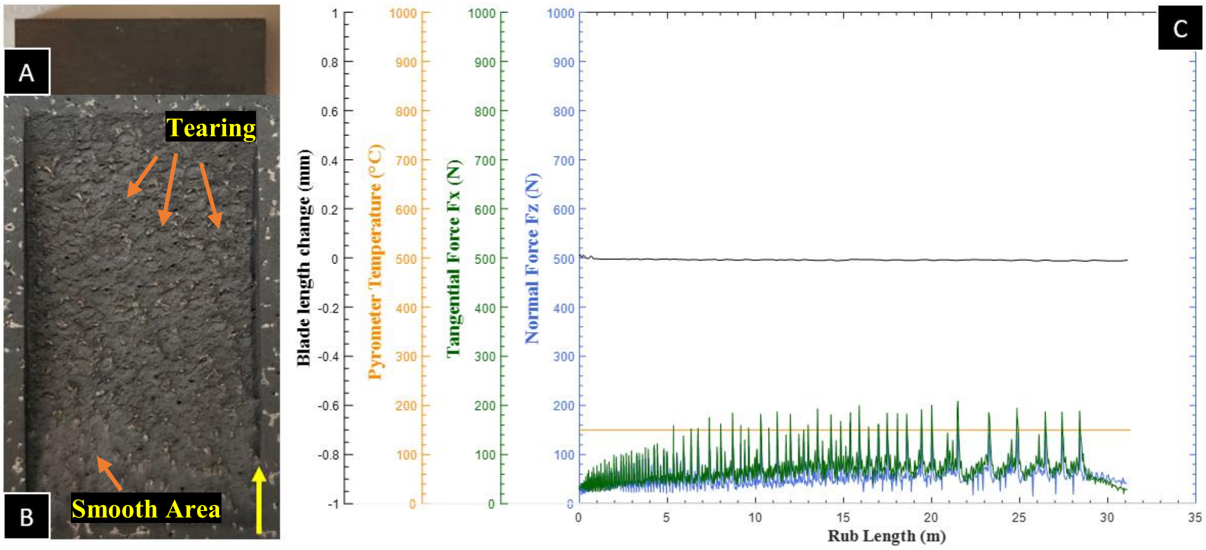

Figure 46. Test 1.2 (Filled Foam – 10% Filler Density – 2 μm/pass – 200 m/s) Post-Test Data A) Blade Tip B) Abradable Surface C) Force, Temperature, Blade Length - Graph

The forces show a periodic behaviour where the normal and tangential forces peak and drop repetitively, force peaks can be seen to reach a greater force than in Figure 45. The duration of time between peaks is similar all throughout the test, cycling of the blade is unlikely due to the relatively low forces and limited thermal exposure. Overall it is likely this change in force behaviour is linked to the observed surface tearing, as the blade speed is also increased it should be noted that there is more energy input into the system and therefore an increase in force is expected.

With an increase in blade tip speed, this more energy input to the system can be representative of a higher strain rate. In turn, the force spikes that follow suggest a potential stick-slip mechanism which is common in rub tests of resin filler material also seen in the tests conducted in Chapter 5 and will be discussed further in the discussion.

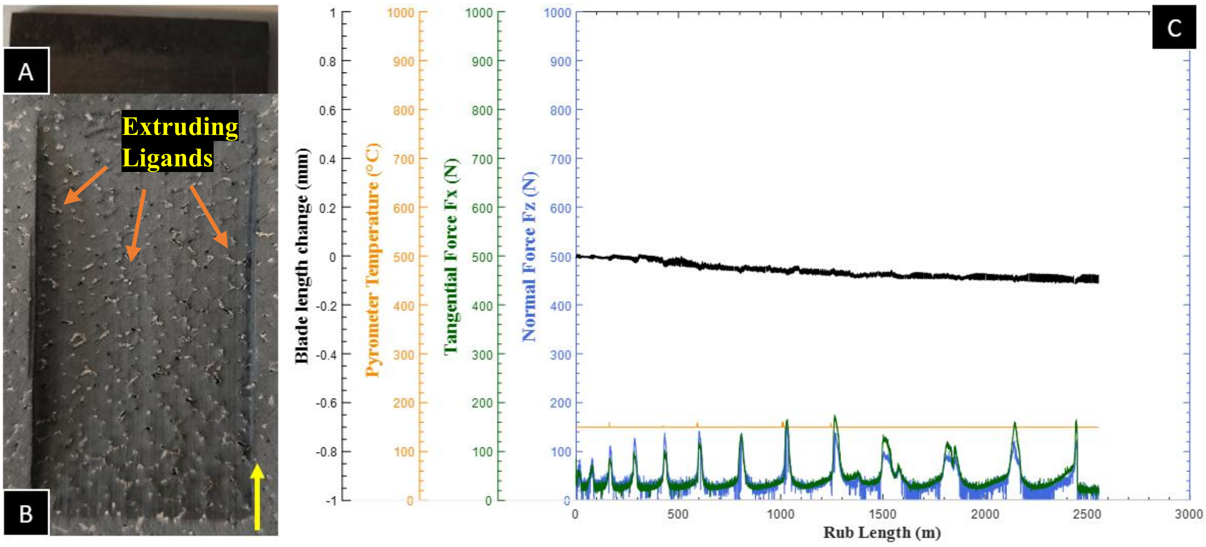

Figure 47. Test 1.3 (Filled Foam – 10% Filler Density – 0.02 μm/pass – 200 m/s) Post-Test Data A) Blade Tip B) Abradable Surface C) Force, Temperature, Blade Length - Graph

Finally a relationship should be established with a lower incursion rate of 0.02 μm/pass for the 10% filler density at the faster tip speed of 200 m/s, the results shown in Figure 47. The rub surface morphology shows less tearing and overall a smoother rub surface compared to the previous test, despite no surface roughness measurements the low forces and no blade wear can be perceived to a smoother rub surface. Empty pores can be identified to suggest that ligand pull-out has happened during the rub test. Additionally a periodic force spike is illustrated in Figure 47C where under the slower incursion conditions is commonly seen as a compression release mechanism. It can be noted that many of the ligaments revealed to the top surface are exposed and extruding out the top surface above the filler material in Figure 47B. This explains the larger tangential force spikes where more resistance to cutting than compaction exists. Specifically seen at the slower incursion rates of 0.02 μm/pass at the first interaction between the blade and ligand there is not enough energy to break it.

It is interesting to note that for the start of the rub test the normal force peaks above the tangential where the force spikes. However, for the mid and latter stages of the rub, this is reversed. Initially, where the normal force peaks it is likely there is more compaction of the abradable, however, after this initial compaction stage the material is subject to more cutting where the abradable has reached a potential limit for compaction.

Maximum and average forces have been plotted and presented in Figure 48 for each test. At the lower tip speed and higher incursion rate condition, the maximum normal force is approximately 40% greater than the maximum tangential force which suggests that the rub test consists of more compression and compaction of the abradable with less cutting capabilities.

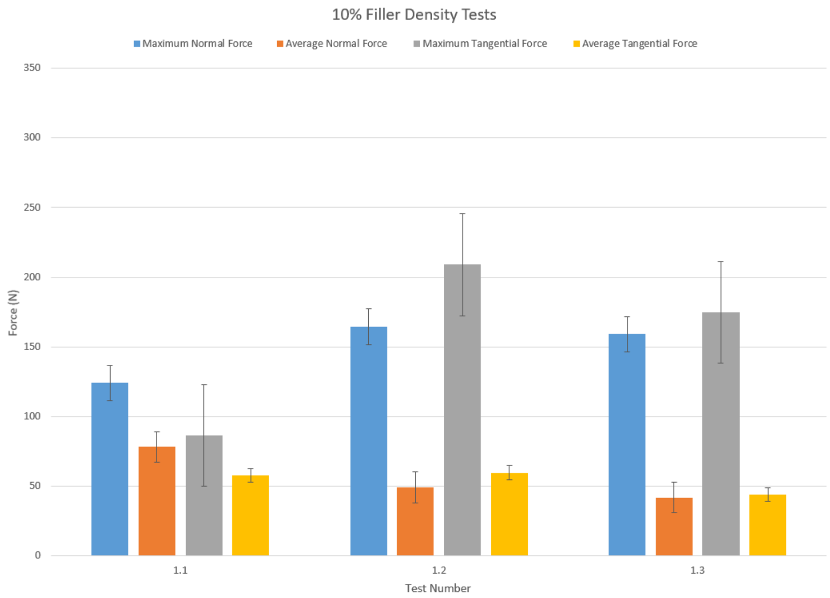

Figure 48. Force data for 10% filler density tests at all three conditions where 1.1: 10% Filler Density - 2 µm/pass – 100 m/s, 1.2: 10% Filler Density - 2 µm/pass – 200 m/s, 1.3: 10% Filler Density – 0.02 µm/pass – 200 m/s

Comparing this with the maximum normal and tangential force at the faster tips speed and incursion rate, the maximum tangential force is approximately 30% greater to imply the existence of more cutting during the rub test.

Finally with a fast tip speed and low incursion rate, it can be seen again that the maximum tangential force is approximately 10% greater than the maximum normal force to suggest the same mechanism where more cutting occurs. It can be noted that at the faster blade tip speeds the average normal and tangential forces are significantly lower in proportion to the maximum values, the stick-slip mechanisms are the main cause of this as shown in the graphs in Figures 46 & 47 where there is a force peak phenomenon.

6.2.1.2 Role of Filler Density for Filled Foams

The resin phase's filler density was changed to 20% from the previous abradable filled foams tested. A change in filler density infers a glass fibre ratio within the polymer resin. High filler density resin was previously tested to show high flexural strength [37].

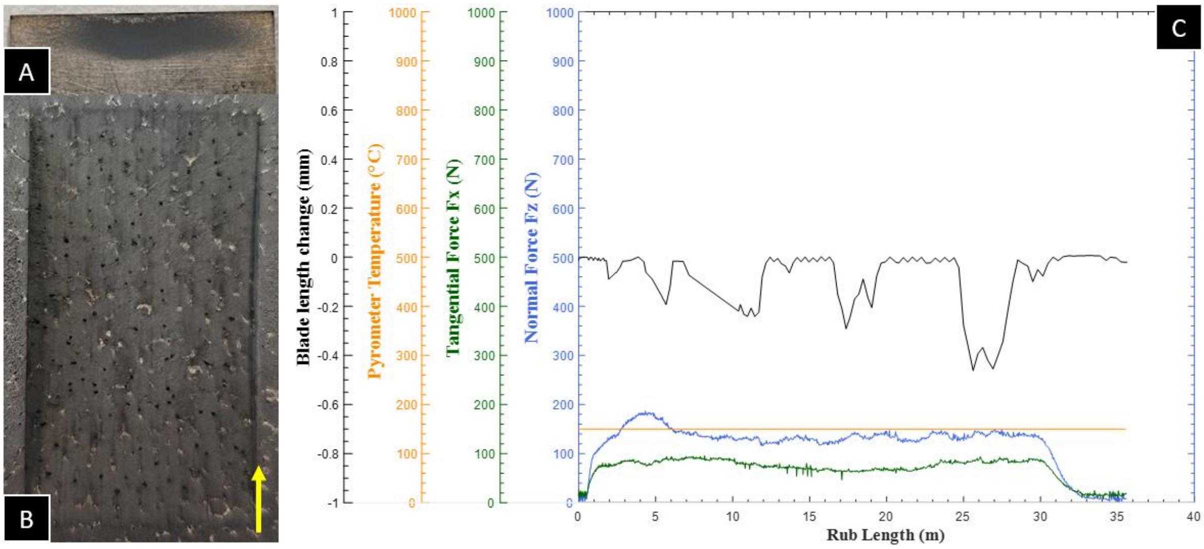

Figure 49. Test 2.1 (Filled Foam – 20% Filler Density – 2 µm/pass – 100 m/s) Post-Test Data A) Blade Tip B) Abradable Surface C) Force, Temperature, Blade Length - Graph

The results shown in Figure 49 represent a foam with a 20% filler density, tested at a higher incursion rate of 2 µm per pass and a blade tip speed of 100 m/s. The surface morphology is very smooth; however, clear signs of ligand pull-out are evident due to the visible empty pores. Thermal smearing is observed on the rub surface, and it is noteworthy that such marks appear to originate from areas where metal ligands were removed. The softening temperature of polyester resin is 85 - 105 °C, likely to suggest thermal smearing [38]. Contact between the metal ligands and the blade can cause small amounts of heat accumulation, generating these smearing marks.

The higher ratio of glass fibre may contribute to the smooth surface morphology. At a microscopic level, the glass fibre exhibits more brittle-like behaviour, which facilitates better cutting of the abradable material. Additionally, the filler can crumble around the ligands, exposing them to the blade. As a result, the interaction between the blade and the ligands leads to the removal and pulling out of the ligands, creating empty pores along the rubbing surface.

Maximum normal force peak shown in Figure 49C is greater in comparison to that of the average normal force of previously tested filled foams, this suggests that the abradable sample may resist cutting and compaction with respect to previous filled foam tests where the normal and tangential forces do not exceed 100 N for extended periods of the rub.

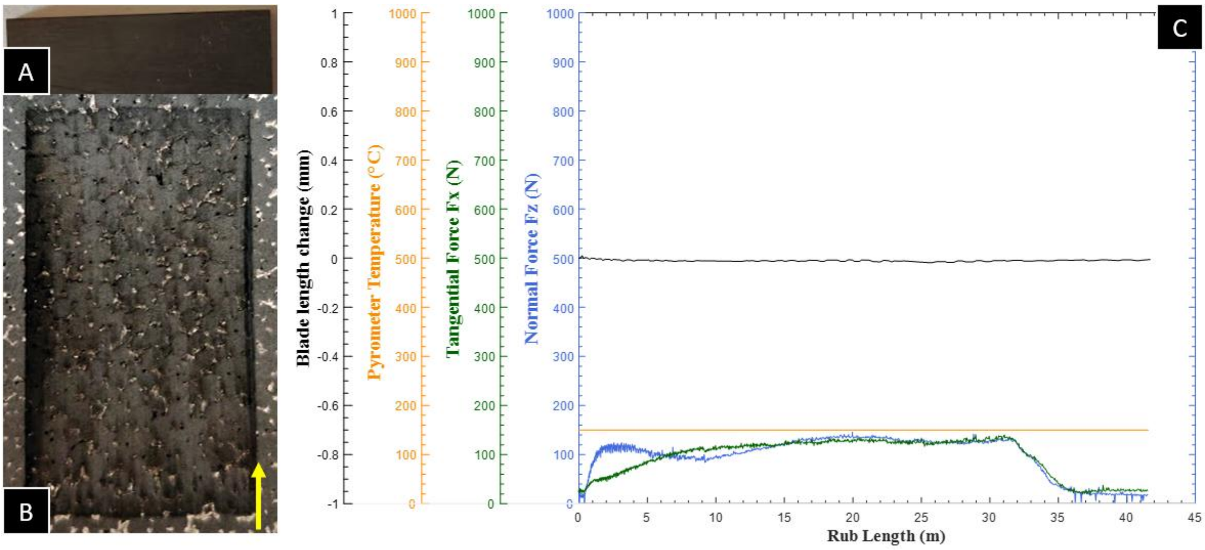

Figure 50. Test 2.2 (Filled Foam – 20% Filler Density – 2 μm/pass – 200 m/s) Post-Test Data A) Blade Tip B) Abradable Surface C) Force, Temperature, Blade Length - Graph

Additionally, it was tested at a faster tip speed of 200 m/s with a high incursion rate constant for the 20% filler density abradable; the results are shown in Figure 50. The rub surface in Figure 50B shows a significant amount of empty pores likely caused by ligand pull-out and signs of smearing, which are more prominent than in the previous test. Smearing can result from heat accumulation from localised ligand temperature where localised melting of the filler phase can occur, furthermore, these hotspots are smeared across the rub as the blade passes. Thermal smearing can most likely occur where the abradable is incapable of heat dissipation through the bulk material and is localised in the ligands within the near subsurface. The filler material crumbling and letting go quickly means no stick-slip mechanism exists in such an instance.

The forces show that cutting occurs as the main mechanism in this test, the forces in Figure 6 in comparison to that in Figure 50 are smaller. This reduction in force at the faster blade tip speeds can be explained through the greater energy input per strike, at the faster tip speeds the energy of the blade per strike is greater resulting in better cutting and lower forces experienced by the abradable sample.

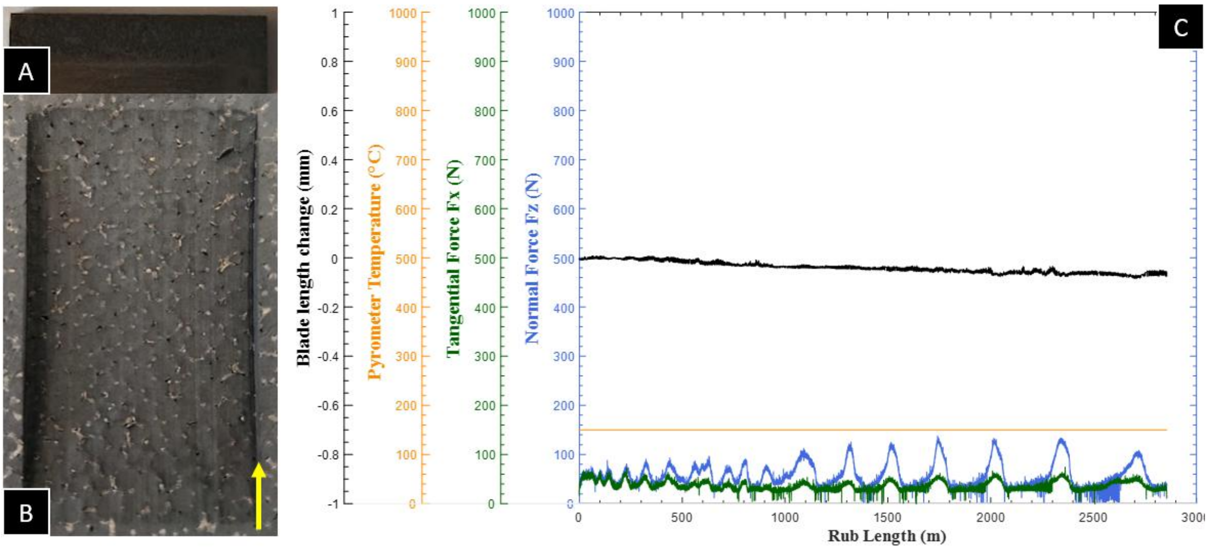

Figure 51. Test 2.3 (Filled Foam – 20% Filler Density – 0.02 µm/pass – 200 m/s) Post-Test Data A) Blade Tip B) Abradable Surface C) Force, Temperature, Blade Length - Graph

Finally, to establish a relationship with the incursion rate during the rub event, Figure 51 shows the results of a 20% filler density tested at the fast tip speed with a reduced incursion rate of 0.02 µm/pass. A few areas show open pores, which again implies that ligand pull-out can still occur at a slower incursion event for this abradable material, but it is not as prominent. Little to no thermal smearing can be identified, which can suggest either less heat accumulation or better heat dissipation.

The forces exhibit a periodic phenomenon in which the normal and tangential forces peak, indicating a compression-release or stick-slip mechanism occurring during the rubbing actions. As previously noted, reducing the incursion rate at higher tip speeds suggests a decrease in the strain rate, which is directly proportional. A similar phenomenon is observable even at a 10% filler density, as shown in Figure 47. While the forces for both the stick-slip and compression-release mechanisms demonstrate this periodic force phenomenon, there are significant differences in their physical characteristics that indicate which mechanism is likely during the test. The compression-release mechanism is typically linked to high temperatures and significant wear due to compression in the near subsurface, eventually leading to cutting [27]. In contrast, the stick-slip mechanism pertains more to the behavioural properties of the abradable material, where tearing of the subsurface results in these force peaks.

As expected, the forces recorded at the higher incursion rate in Figures 48C & 49C are substantially larger compared to the slower incursion rate in Figure 50C. This can only be with respect to the average normal force, as at the lower incursion rate, this common phenomenon of periodicity occurs within the force trace, which would imply a compression release mechanism to exist. With a filler density of 20%, it is generally seen that next to no blade wear occurs, Figure 51C shows some signs of blade wear from the blade length change over the rub test, which is as expected since at the slower incursion rates, where there is more abradable-blade contact.

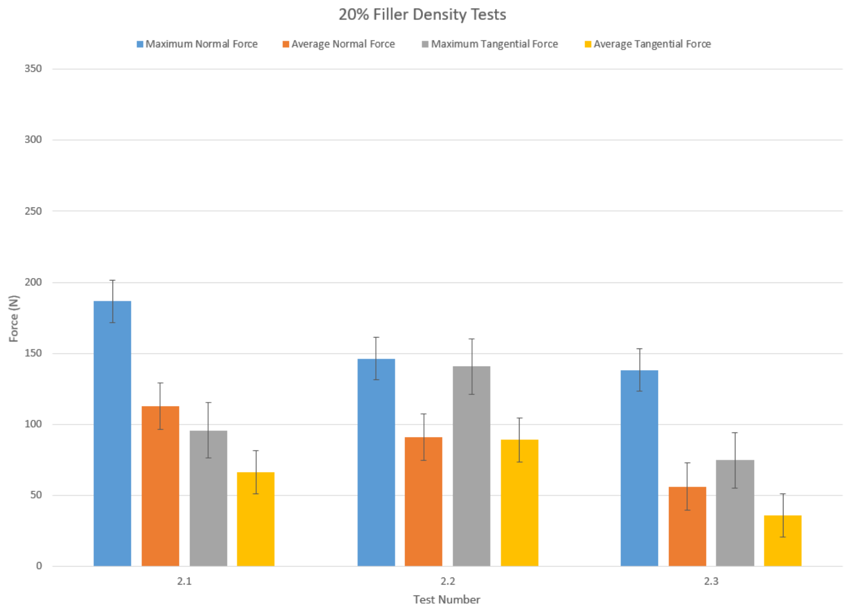

Figure 52. Force data for 10% filler density tests at all three conditions where 2.1: 20% Filler Density - 2 µm/pass – 100 m/s, 2.2: 20% Filler Density - 2 µm/pass – 200 m/s, 2.3: 20% Filler Density – 0.02 µm/pass – 200 m/s

Figure 52 shows the maximum and average forces for a 20% filler density abradable samples at both tip speeds with a closer comparison of the low and high incursion rates at the faster tip speeds. At the lower tip speeds the maximum normal and tangential forces are greater which is expected where the normal exceeds the tangential by a significant amount, less energy input can result in less efficient cutting of the abradable surface. It should be noted that at the faster tip speed the normal and tangential forces are roughly equivalent to suggest a better and more efficient cutting mechanism.

6.2.2 Filler Properties and Thermal Ageing

To understand the filler's role in the wear mechanisms of such an abradable sample, it was necessary to isolate the resin filler material and perform rub tests to identify the behavioural properties under various conditions. Furthermore, in-flight conditions propose long-term thermal exposure to such abradable samples. For such reasons, thermal ageing has additionally been used to investigate the change in material behaviour and properties during rub tests.

6.2.2.1 Unaged Filler

Both 10 and 20% filler density were tested under normal operating conditions of 200 m/s blade tip speed with varying incursion rates of 0.02 µm/pass and 2 µm/pass and no thermal exposure pretesting.

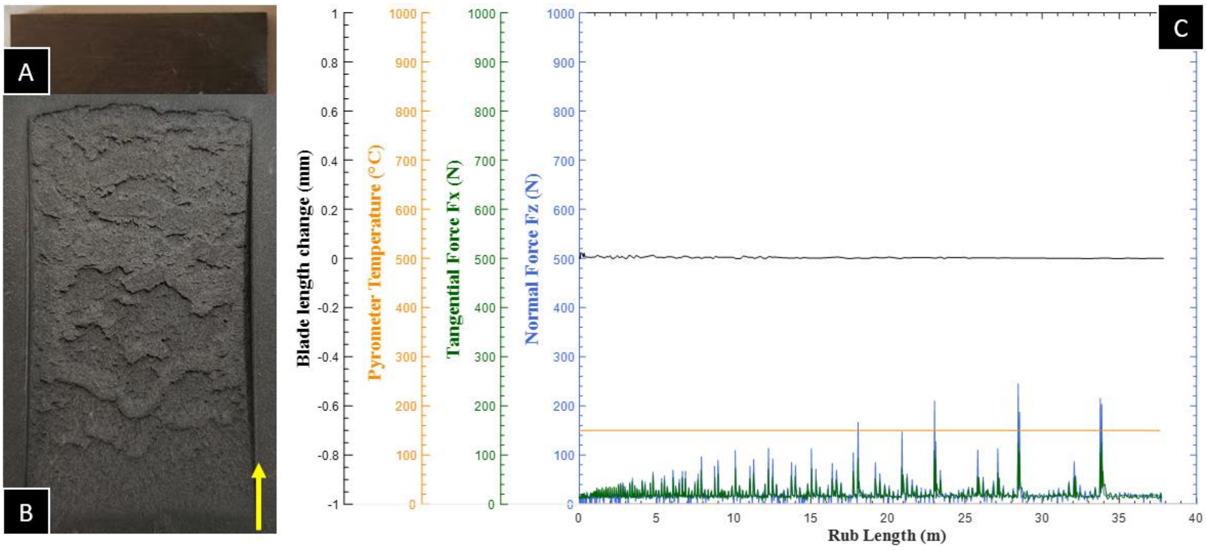

Figure 53. Test 3.1 (Filler Only – 10% Filler Density – 2 µm/pass – 200 m/s – 250 °C – 100 h) Post-Test Data A) Blade Tip B) Abradable Surface C) Force, Temperature, Blade Length - Graph

Typically a periodic force spike is seen at the lower incursion rates where a compression release mechanism occurs. Figure 53 shows a similar phenomenon, however, at the high incursion rate. Resin filler materials exhibit a stick-slip mechanism similar to that of polymer rubbers [39]. During a stick-slip mechanism, the resin material is capable of detaching from the bulk material to then reattach further along the rub contact surface.

Note that the normal force peaks and drops slightly before the tangential, this would suggest a release of an accumulation of resin which is then moved and spread further along the rub surface through the blade path. As shown in Figure 53A the start of the rub path morphology doesn’t seem to look as rough as the mid-to-end section of the rub path. It can also be noted that little blade length change occurs however from observing the blade tip post-test a small layer of adhesion has appeared.

In this case, the phenomenon seen does look as though a compression release mechanism exists, however, taking into account material composition and relative forces a stick-slip mechanism could be the driving force for such physical observations of the blade and abradable post-test.

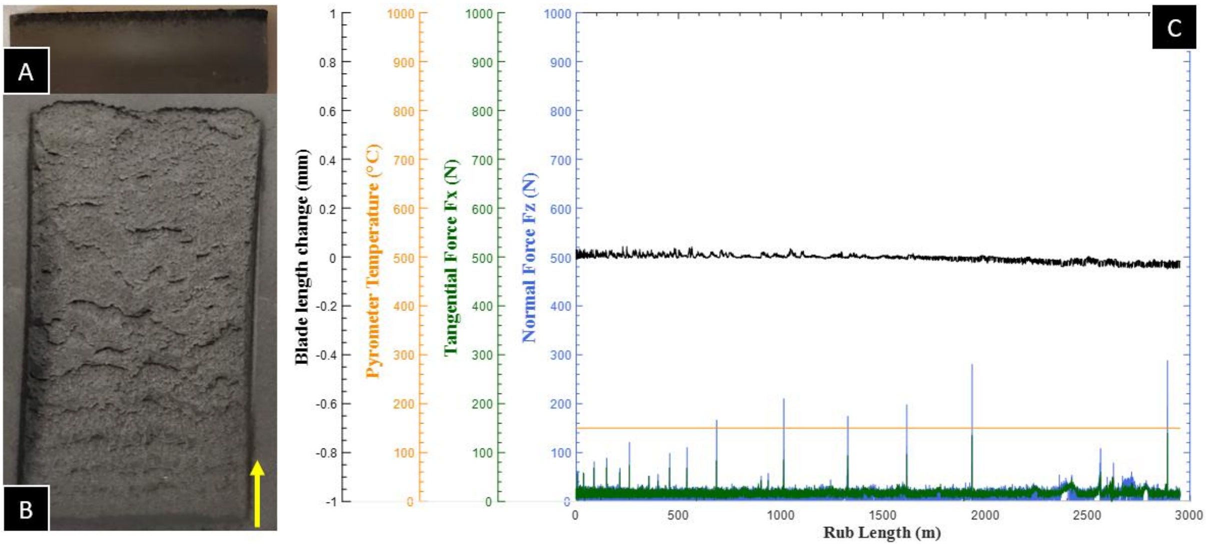

Figure 54. Test 3.2 (Filler Only – 20% Filler Density – 0.02 µm/pass – 200 m/s – 250 °C – 100 h) Post-Test Data A) Blade Tip B) Abradable Surface C) Force, Temperature, Blade Length - Graph

Figure 54C shows that at the low incursion rates, the 10% filler density resin also tears with a stick-slip mechanism. The force peaks show the normal and tangential forces rise and drop in unison where a detachment of resin filler accumulation occurs. This stick and slip mechanism can cause reattachment of the resin filler to occur which results in this rough rub surface seen post-test in Figure 53B & 54B.

A little blade length change can be seen in Figure 55C where the incursion rate is slower, this little change in blade length would suggest signs of wear however not very significant. At the slower incursion rates, more blade-to-abradable contact exists which allows for this little change in blade length.

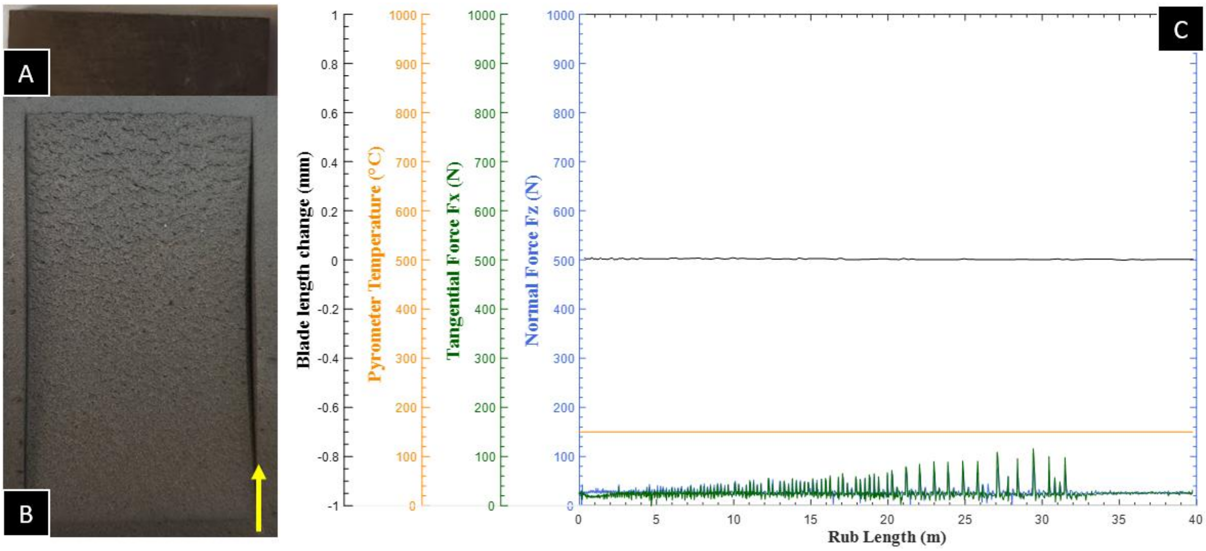

Figure 55. Test 3.3 (Filler Only – 10% Filler Density – 2 µm/pass – 200 m/s – 300 °C – 100 h) Post-Test Data A) Blade Tip B) Abradable Surface C) Force, Temperature, Blade Length - Graph

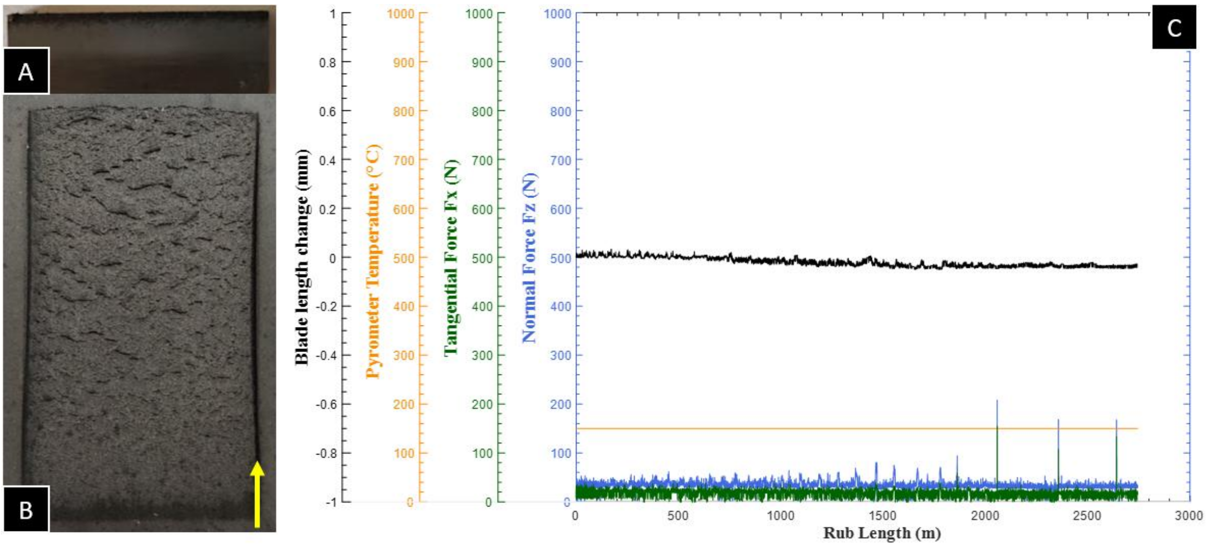

Figure 56. Test 3.4 (Filler Only – 20% Filler Density – 0.02 µm/pass – 200 m/s – 300 °C – 100 h) Post-Test Data A) Blade Tip B) Abradable Surface C) Force, Temperature, Blade Length - Graph

Figure 56 shows the results at the high incursion rate however the filler density of the foam is 20% to understand the difference in material response. Yet again this periodic phenomenon with the force trace occurs, and this stick-slip mechanism previously mentioned exists again. In comparison to the same operating conditions, however, a 10% filler density some key differences can be seen. Firstly, it can be noted that the normal and tangential forces are significantly lower where a higher filler density exists. The higher filler density is caused by an increase in glass fibre content within the resin filler. Such an increase in glass fibre content means more brittle behaviour of the foam on a microstructural level suggesting a cleaner cut and rub and dislocation of material upon each strike of the blade. A much smoother rub morphology is desired like this where the abradable has seemed to cut and compact with minimal to no blade damage or wear.

If a reduction in strain rate occurs for the 20% filler density a stick-slip mechanism does not seem to exist from the force trace however considering the rub surface post-test in Figure 57B some tearing of the foam seems to occur. The force data show very low forces with a few peaks towards the end of the rub, these would suggest a stick-slip mechanism from resin accumulation and release. The low strain rate results in a low energy input upon each strike of the blade to create a rougher surface morphology as seen in Figure 57B where the activation energy to cut the material has not been met.

At the slower incursion rate, a small change in blade length can be seen in Figure 57C. However, from the blade tip post-test in Figure 57A a layer of resin seemed to deposit on the tip edge, the reduction in incursion rate causes more passes of the blade by a factor of 100 compared to the fast incursion rate. It is likely that with more strikes of the blade, some blade wear exists.

6.2.2.2 Thermally Aged Filler

To understand the true reality of whether these abradable samples can be used thermal ageing studies have been proposed to further investigate the compatibility of these resin filler materials under more realistic conditions. Samples have been aged for a total of 100 (h) hours which is a standard ageing time according to various studies where little to no change in material mechanical properties after the first 100h mark [31][30][40], a contrast has been set between 250°C and 300°C which are suitable operating temperature exposures for the application of an abradable sample in the afore mentioned compressor stage.

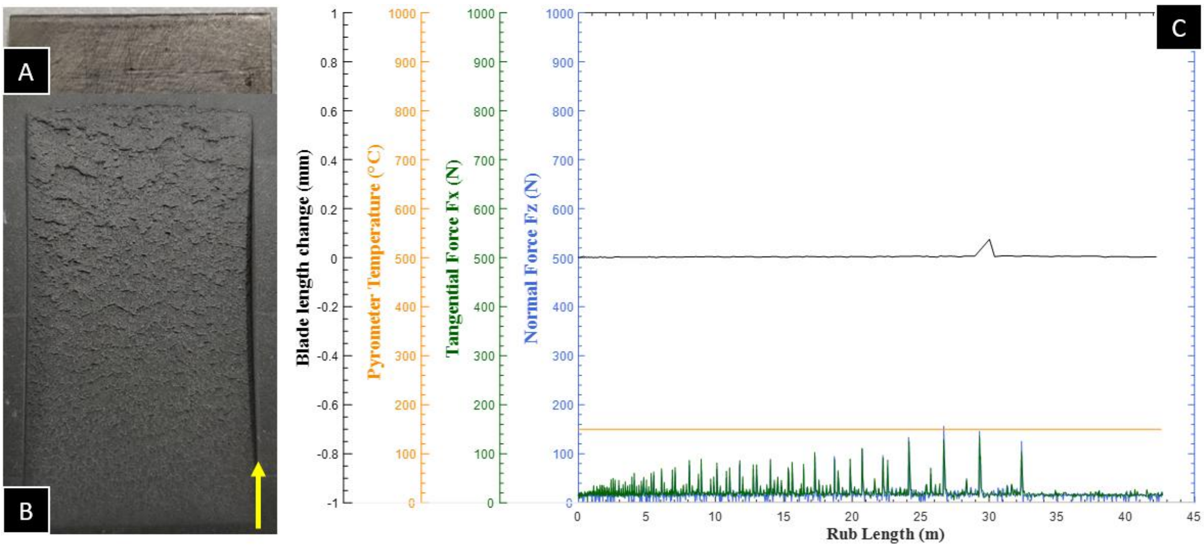

Figure 57. Test 4.1 (Filler Only – 10% Filler Density – 0.02 µm/pass – 200 m/s – 250 °C – 100 h) Post-Test Data A) Blade Tip B) Abradable Surface C) Force, Temperature, Blade Length - Graph

Figure 57 shows the results for a 10% filler density resin abradable after ageing at 250°C for 100 h. As seen visually from the rub surface morphology this rougher surface exists towards the end of the rub whilst a smoother morphology can be seen at the start of the rub. Figure 58C suggests a stick-slip mechanism to exist even after thermal ageing, all ageing tests have been subject to a standard incursion rate of 2 µm/pass. No change in blade length can be seen in Figure 57A, from the graph a small peak change in blade length occurs, however, this is due to the overexposure for image capture.

Typically seen with resin abradable samples the normal and tangential forces are very low which suggest easy removal of the material however some levels of compaction may occur during the test.

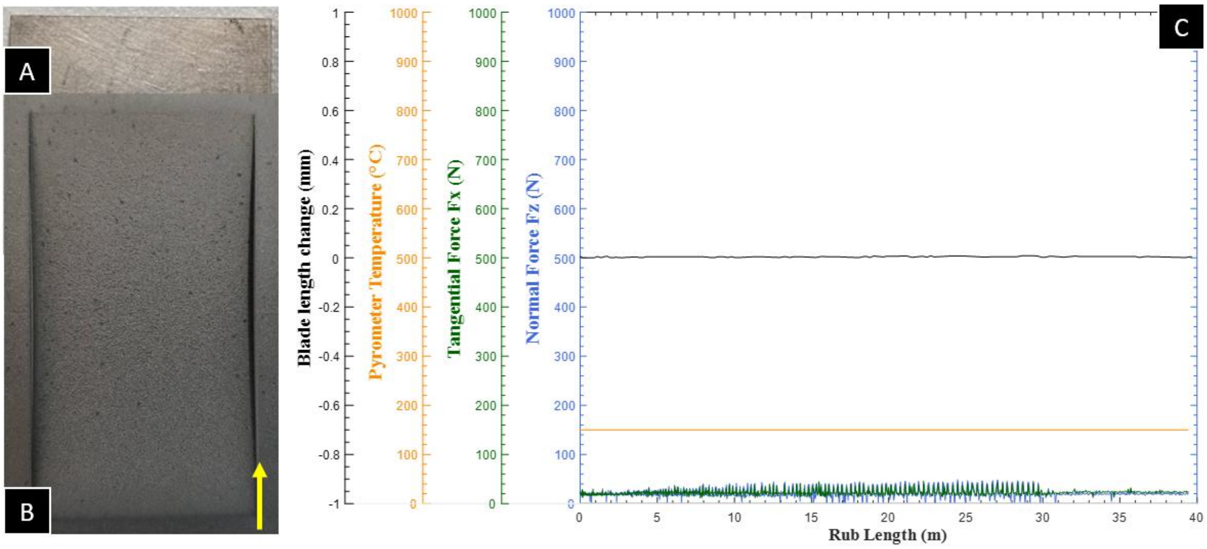

Figure 59. Test 4.2 (Filler Only – 20% Filler Density – 0.02 µm/pass – 200 m/s – 250 °C – 100 h) Post-Test Data A) Blade Tip B) Abradable Surface C) Force, Temperature, Blade Length - Graph

After ageing tests at 250°C for 100 h the 20% filler density sample can be seen to have a very smooth surface. Ageing of the polyester resin causes the resin matrix to become brittle reducing its ability to transfer stress to the glass fibre. The material is therefore more prone to brittle fracture instead of energy-absorbing deformation. Hardness of polyester resin usually decreases with thermal aging as the resin softens, the heat breaks the chemical bonds within the polyester resin, the long polymer chains break into shorter ones. Additionally, at temperatures of +200 °C oxygen reacts with the resin, oxidation of polymer chains disrupts chain packing and formation leading to a loss in structural integrity and softening [41][35], [38][42].

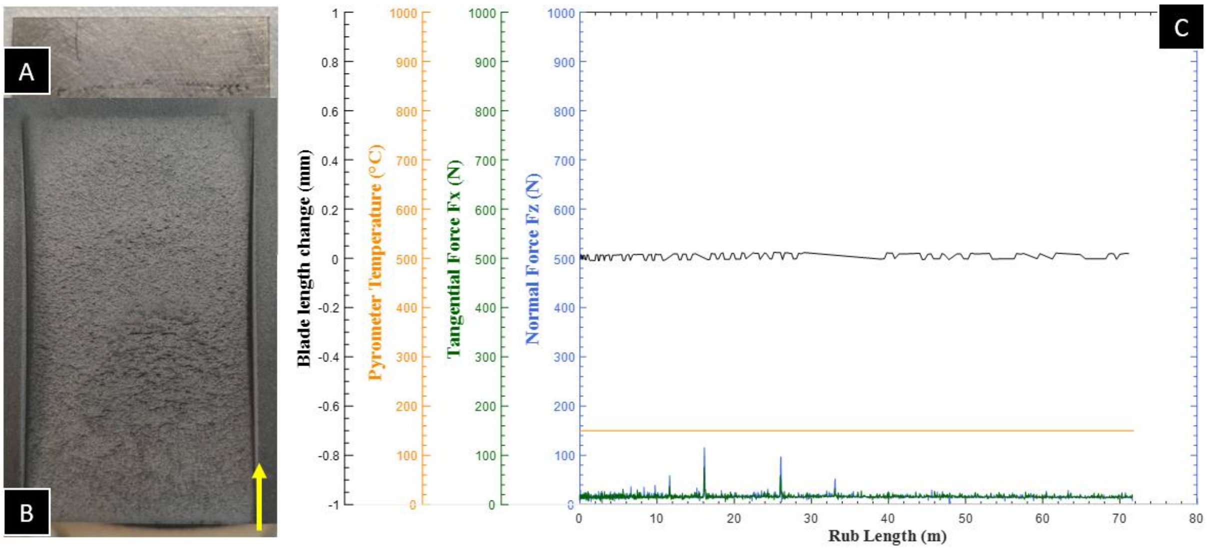

Figure 58. Test 4.3 (Filler Only – 10% Filler Density – 0.02 µm/pass – 200 m/s – 300 °C – 100 h) Post-Test Data A) Blade Tip B) Abradable Surface C) Force, Temperature, Blade Length – Graph

Forces are significantly smaller in comparison to the 10% filler density, this increase in brittle behaviour allows for more local dislocations and fracture on a microstructural level leading to a surface morphology as seen in Figure 60B. Due to such easy removal of the resin foam no blade wear or damage occurs which is very desirable.

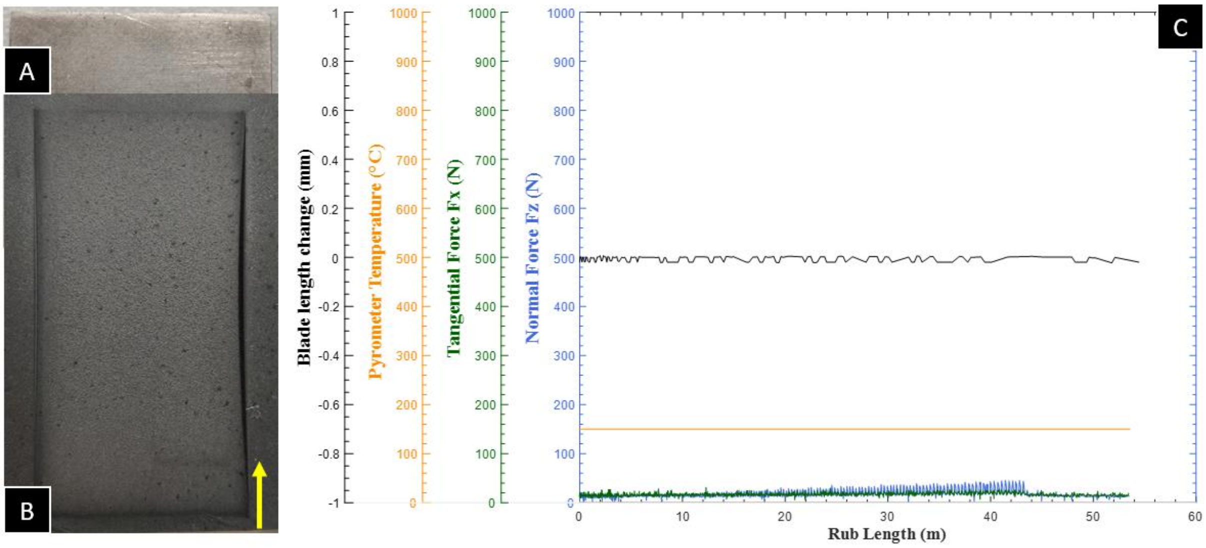

Figure 60. Test 4.4 (Filler Only – 20% Filler Density – 0.02 µm/pass – 200 m/s – 300 °C – 100 h) Post-Test Data A) Blade Tip B) Abradable Surface C) Force, Temperature, Blade Length - Graph

Figure 60 shows the results for thermal ageing exposure of 300°C for 100 h. Force data shows minimal forces upon contact between the blade and the abradable however the surface morphology in Figure 60B shows some tearing to exist. This tearing however is not in the conventional location of the end of the rub path, this could, however, be a result of inconsistencies within the resin microstructure after the effects of long-term thermal exposure. From the blade tip in Figure 60A, no blade wear or adhesions can be seen, this fluctuation in blade length change seen from the graph can be a result of overexposure of the camera.

Similarly for the 20% filler density resin, after thermal ageing exposure at 300°C for 100 h low forces can be seen yet again. As the filler is thermally aged the resin degrades, the relative fraction of glass fibre increases cause this more brittle behaviour and easier cutting [40]. Local dislocation on a microstructural scale to allow easy material removal. This shows the smooth rub surface morphology in Figure 60B. Furthermore, fluctuations in the blade length can be seen in Figure 60C, however, visually from the blade in Figure 60A no signs of adhesion or blade wear exist. These fluctuations are caused by overexposure of the camera during rub tests.

6.2.3 Thermal Ageing Under Standard Test Conditions

After isolating just the resin it is important to investigate whether these same wear behaviours and mechanics exist with standardised filled foams. For ageing tests, a comparison of the 10% and 20% filler density is assessed as well as the difference in behaviour for the difference in composition seen previously in Figures 49 & 50. These tests were all carried out at the faster blade speed of 200 m/s at the high incursion of 2 µm/pass. Ageing conditions previously used have been adopted again for repeatability purposes where 250°C and 300°C are appropriate temperatures for ageing studies for an exposure period of 100 h.

6.2.3.1 Thermally Aged

At 250°C for 100h a similar mechanism can be identified in comparison with the non-thermally aged samples where a compression release mechanism exists.

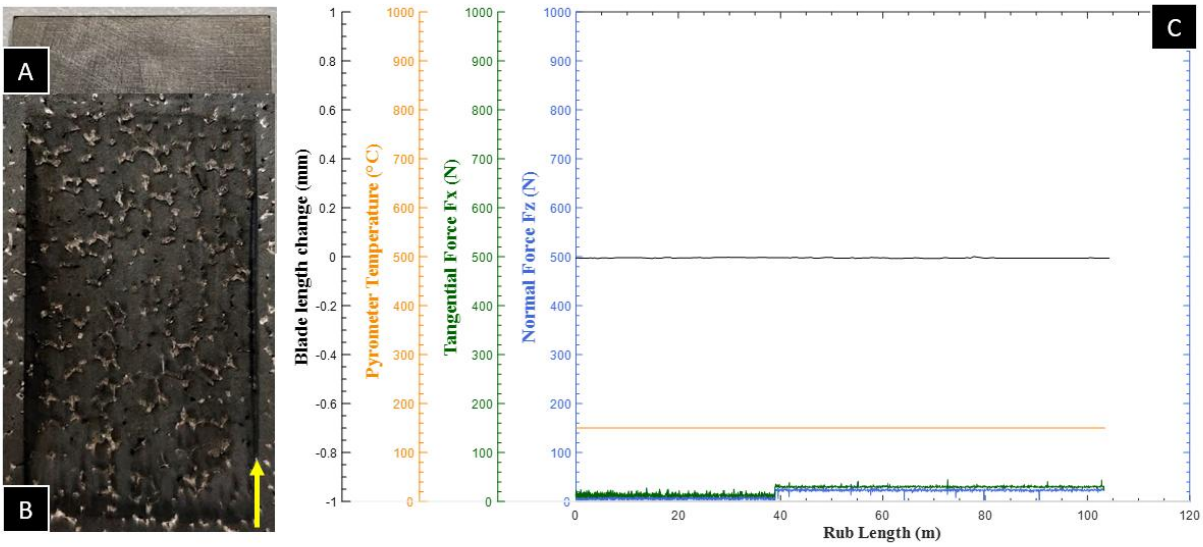

Figure 61. Test 5.1 (Filler Only – 10% Filler Density – 2 µm/pass – 200 m/s – 250 °C – 100 h) Post-Test Data A) Blade Tip B) Abradable Surface C) Force, Temperature, Blade Length - Graph

From observing the rub surface and blade tip after the test in Figures 61A & B, the rub surface looks very similar to that in Figure 48B where an unaged 20% filler density has been tested. It is known that when the polyester resin is thermally aged the mechanical properties change, such that more brittle fracture will occur as well as decreased hardness to support the smoother cut surface in Figure 61B. The metallic ligaments are seen to almost extrude outwards. This can result from the filler material crumbling around the ligaments revealing them and causing smears where temperature accumulation has occurred.

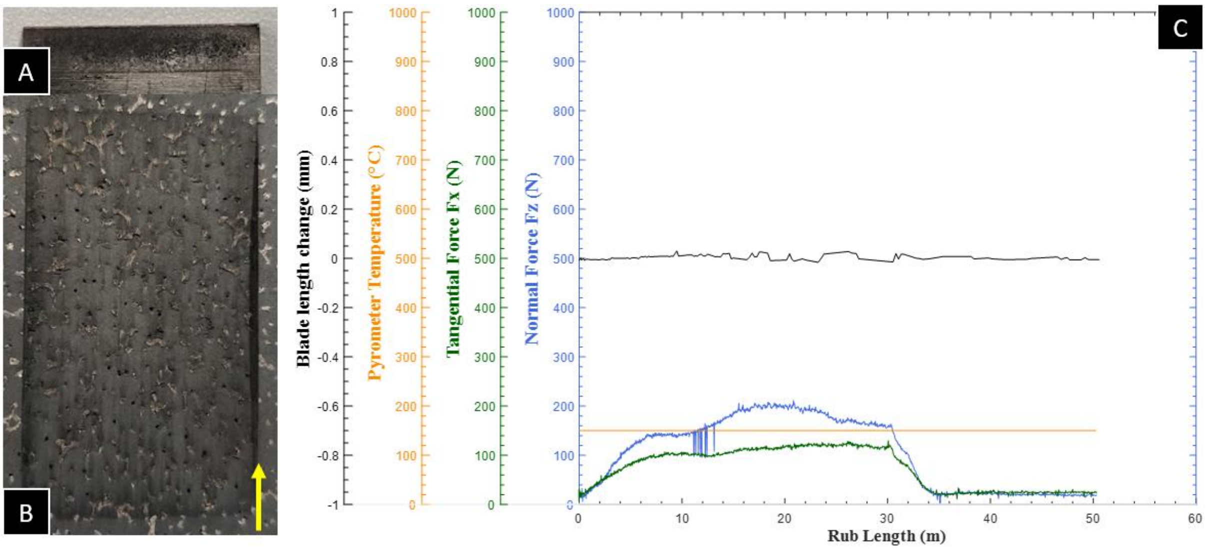

Figure 62. Test 5.2 (Filler Only – 20% Filler Density – 2 μm/pass – 200 m/s – 250 °C – 100 h) Post-Test Data A) Blade Tip B) Abradable Surface C) Force, Temperature, Blade Length - Graph

Figure 62 shows the results for aged samples starting with a standardised 20% filler density-filled foam. The forces show that the abradable resists compaction and is stiffer. The additional glass fibre content in comparison to the 10% in test 5.1 in combination with long-term exposure to temperature causes more stiffness in the bulk abradable and such a rise in the normal and tangential forces. The smooth cut surface can be described as the local brittle behaviour of the resin however a global resistance to deformation exists as shown by the larger forces in Figure 62C. Ligand pull-out and removal still can be seen to occur at the fast incursion rate however not to the extent previously shown by the slow incursion rate. The fluctuations and changes in blade length change could show potential material pick up and then loss, after looking through the images more closely these changes are a result of poor image quality.

6.2.3.2 Increasing Ageing

Further ageing tests were conducted to investigate the temperature capabilities of the filler and metallic foam complex. These have a consistent ageing time, however, the temperature was adjusted to 300°C for harsher temperature environments.

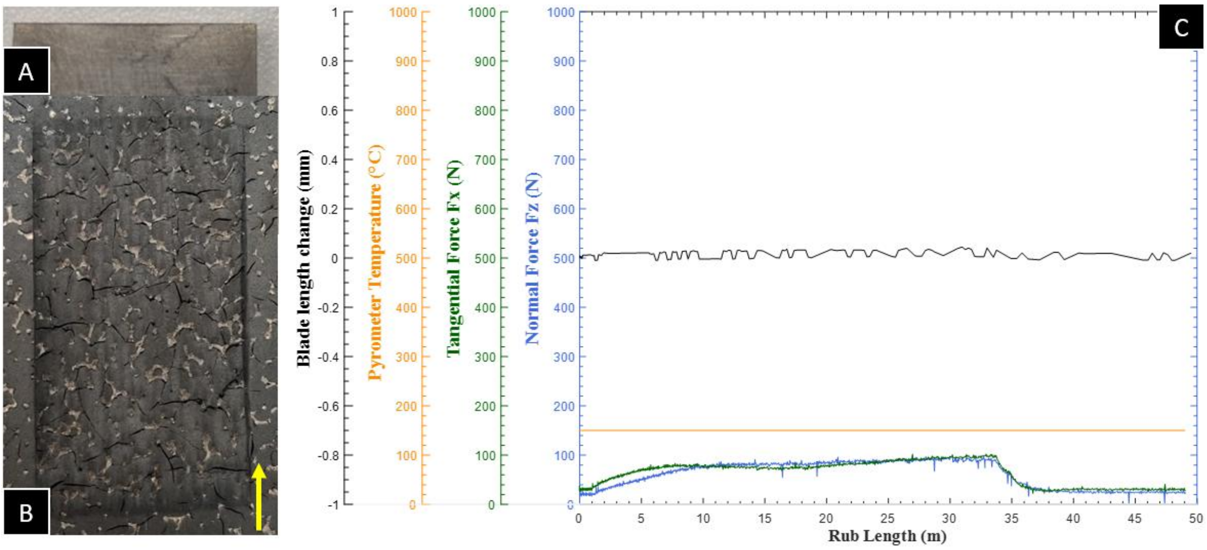

Figure 63. Test 5.3 (Filler Only – 10% Filler Density – 2 µm/pass – 200 m/s – 300 °C – 100 h) Post-Test Data A) Blade Tip B) Abradable Surface C) Force, Temperature, Blade Length - Graph

After such extreme thermal ageing exposure a few visual observations can be seen in Figure 63B. Cracking and fault lines have appeared within the abradable, a result of the oxidation of the resin at elevated temperatures where the chain packing and structural formation has been disrupted [41], [42]. As the sample is thermally aged the fraction of glass fibre in the filler increases as a result of resin degradation. The 20% glass fibre content clearly shows that there is more thermal smearing and temperature accumulation in the rub (Figure 64B), this can be linked to surface hardness.

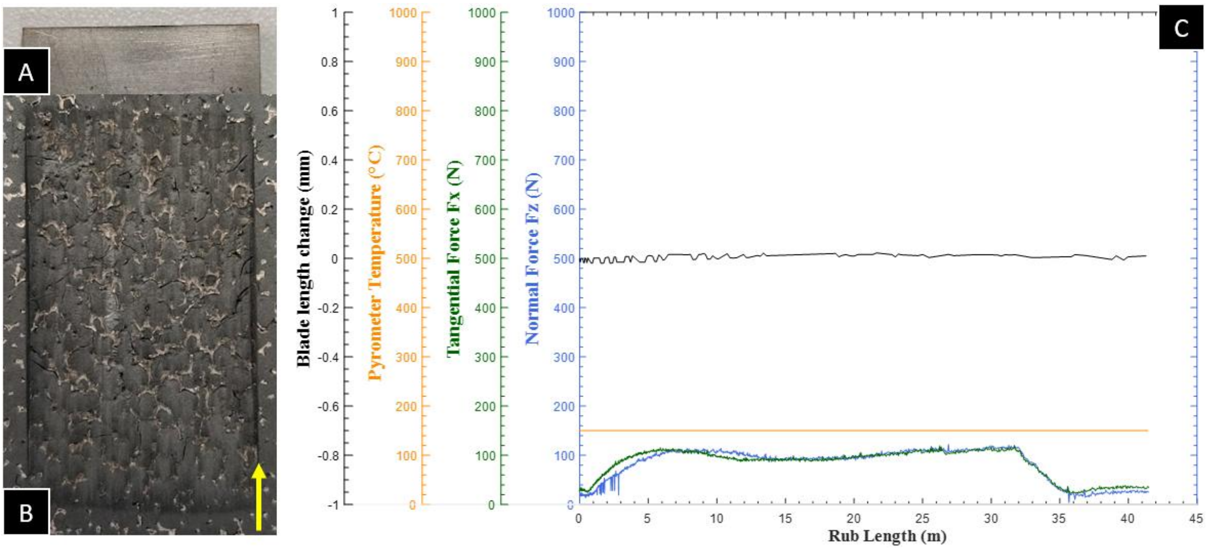

Figure 64. Test 5.4 (Filler Only – 10% Filler Density – 2 µm/pass – 200 m/s – 300 °C – 100 h) Post-Test Data A) Blade Tip B) Abradable Surface C) Force, Temperature, Blade Length - Graph

However, the forces seen during the test are significantly lower due to a local fracture removal mechanism of the resin, this is caused by the brittle behaviour after ageing [43]. Microstructural local fracture of the resin allows easy cutting as the blade strikes the sample, as a result of these localisations thermal smearing exists where the heat accumulates along the top rub surface. As the resin has become dense the ligaments are more firmly held in place to prevent ligand pull-out a phenomenon commonly seen with such abradable samples.

Considering a 20% filler density foam with such ageing conditions in Figure 64, fault lines also exist within the abradable , however, they are less prominent post-rub in comparison to Figure 64B. From the rub surface post rub a lot of thermal smearing exists, this is to an extent where in some areas thermal smearing has resulted in what seems to look like melting of the metal ligaments and resin. This thermal smearing can be due to the large amounts of heat accumulation within the rub where there is an increase in surface hardness. Figure 64A shows some thermal marks on the blade tip post-test the pyrometer has not picked up , however, this could be due to the measured location not showing any signs of rising temperature but not representative of the entire rub surface.

6.3 Discussion

6.3.1 Incursion Rate and Blade Tip Speed

It can be seen that the polyester filler will deform upon contact from the blade. However, once deformed to an extent where the deforming force has been removed, i.e. separation of the polymer, it will tear and reattach. This is where the polymer chains detach and reattach further along the rub surface to preserve a rub surface such as that seen in Figure 45B. There is likely a stick-slip mechanism which has occurred where the resin has detached and reattached in some places, additionally tearing in other regions. The resin filler that supports and holds the ligaments in place shows viscoelastic behaviour where the rubber actuates a stick-slip mechanism.

For the system to remain in equilibrium certain surface energy exists where if this is exceeded a detachment from the surface will occur creating a tear, this can be seen extensively at the higher incursion rate which directly correlates to the afore mentioned higher surface strain rate. The behaviour seen in this test is resin driven, where the resin deforms plastically it tears from the surrounding ligands, as the ligands are more firmly held in place less pull-out is seen, conversely this induces a rough surface morphology.

Lowering the incursion rate at the higher blade tip speeds is expected to have a reduction in strain rate within the abradable material. The results in Figures 45 & 46 shows a clear contrast between high and low incursion rates at the faster tip speeds, where the rub surface of the abradable and specifically the behaviour of the resin is more comparable to that of the fast incursion rate at lower blade tip speeds. The similarity in strain rate for these two conditions is likely to cause the similarities within the resin elastic response. Strain rate is important in defining the abradable response, high incursion rate with a low tip speed can be comparable to a low incursion rate at a faster tip speed and such similar abradable response can be expected.

A few temperature increases have been identified to signify that some potential sparks may have occurred during the rub. Furthermore, signs of blade wear are prominent from the graph in Figure 46C which correlates with the blade tip where signs of wear can also be identified as linked to a compression and release mechanism seen in Chapter 5.

6.3.2 Filler Density

Filler density of the resin is equated to the quantity of glass fibre the polyester resin holds, these are tested at 10 and 20%. 10% filler density shows signs of tearing which suggests ductility in the surface material. It can be noted that a stick-slip mechanism can occur per pass of the blade. The resulting surface morphology is dependent on whether the mechanism shows ligand or resin actuation. Actuation of the ligands in the abradable can lead to more ligand pull-out and overall a smoother morphology whereas actuation of the resin filler shows a rippling effect in areas of local fracture and detachment.

At the higher filler density with an increased glass fibre proportional volume it allows for a more brittle behaviour within the microstructure which in turn generates smooth rub surface, this can also be influenced by the surface strain rate stated previously where a comparison can be made between the foams at different speeds and conditions. Where the 20% filler density surface shows signs of tearing at the lower tip speeds however in comparison 10% at the faster tip speeds shows similar behaviour. From the tests carried out it would seems that the optimal filler density would be 20%.

Hasim et al. studied the rubbing contact and wear of glass fibre polyester composite to a plain resin with different sliding distances [44][35]. Similarly there is less wear for glass fibre polyester composites as the surface brittle layer breaks away more easily.

6.3.3 Thermal Ageing

For an abradable lining thermal exposure is critical for performance. Upon thermal exposure the glass fibre proportion will increase, this shows that after thermal exposure for the 10% filler density for 100 h at 250°C the cutting performance is enhanced. This increase in performance and cutting is related to the direct correlation between the increase in glass fibre proportion inducing a more global brittle behaviour [38], [40]. The 20% filler density substrate under the same thermal exposure condition also shows excellent cutting performance.

It should be noted that after thermal ageing exposure there are more signs of thermal smear along the rub surface, this suggests that the lack of ductility in the surface causing more surface friction which has in turn cause some localised heating of the metallic foam ligands and in removal has reacted the resin across the rub.

6.4 Conclusion

The strain rate of the surface contact is of great importance where this is linked to the blade tip speeds, incursion rates and filler density. For lower blade tip speeds and lower incursion rates the surface strain rate is significantly higher which results in mechanisms such as tearing and ligand pull out. The filler density is closely linked to the thermal exposure of the samples where with an increase in exposure time an increase in filler density will also occur, the higher filler density quantity generates a better cut with less ligand pull out however under higher temperatures of 300°C the expansion of the resin begins to form cracks which will influence the sealing ability. Such temperature limitations in the aero-engine call for an alternative since an optimal temperature for these substrates sits around 200 – 250 °C.

Chapter 7

Abradable Capped Metallic Foams

Open-cell metallic foams have been previously investigated for their desirable mechanical and thermal properties during rub tests. Due to the limitation of temperature operations for resin filler in compressor stages of aero-engines, abradable capped foams have been investigated consisting of conventional abradable material onto a metallic foam substrate. Filled foams show behaviours where the ligaments are cut and compacted to form a tight seal, capped foams can be relevant to show compaction and deflection of the foam phase while consistent deformation of the cap material when working in unison. The capped foams comprised of a Metco 320 (AlSi/hBN) coating were applied onto a NiCr metallic foam substrate of two different pore sizes for comparison and to study what mechanisms are actuated during rubbing tests.

Foams have been previously tested to exhibit excellent behaviours through a tendency to fracture and collapse. Current conventional materials such as Metco 320, an AlSi alloy matrix shows to have great cutting behaviours however some implications are present. These include compaction and pushback, as the blade interacts with the abradable compression occurs condensing the abradable. Under this scenario, high forces and temperatures are observed calling for more material adhesion and wearing of the blade. The addition of the foam base layer can help to reduce the high forces and wear damage as a result of localised fracture and collapse of ligaments and struts leading to a degree of compromise. In combination, the two mechanisms can show promise in creating a new generation of sealing abradable material suitable for compressor stage conditions improving performance and reliability as opposed to current technologies.

This chapter aims to investigate how capped foams behave and deform under various loading conditions, additionally looking into the optimisation of such wear mechanisms. Study of the fundamental factors and properties which can affect the behaviour and outcome to create consistency in tests being able to effectively actuate such mechanisms based on properties of materials.

7.1 Test Samples and Details

Figure 65 shows a typical blade (A) and abradable sample (B) used in this study. The test blade shown on the left of the Figure (A), manufactured from Inconel 718, and represents the standard test blade used at all times in this study. On the centre and right of the Figure 65 (B) & (C) are the as manufactured and post-processed abradable samples, where on the as-manufactured sample the thermally spayed abradable cap is clearly visible on top of the foam. As highlighted in the Figure, the foam sample has been ground prior to testing, and this process will be detailed in the following section.

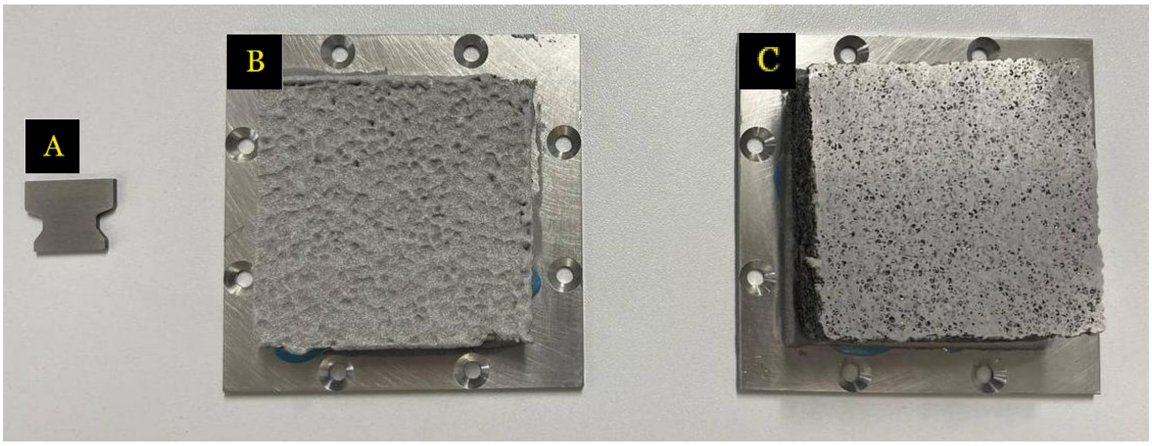

Figure 65. (A) Blade with, Samples (B) Manufactured Foam and (C) Ground Foam

The metal foam material used as the substrate is commercially sourced, and is manufactured by Recemat BV under the trade name NC1116. It is manufactured through a heat treatment process, where a nickel precursor material is unwound. This process involves the application of an initial binder solution to first coat the material, followed by another coating of high alloy powder. Next a heat treatment process is employed, consisting of steps of de-binding and sintering. The de-binding phase of the process involves removal of the initial binder solution from the metallic structure surface, before sintering enables the high alloy powder to diffuse effectively into the metallic ligaments of the foam structure, creating a homogeneous and uniform material microstructure, in this case in the form of the purchased sheet. In order to prepare the test specimens, foam samples are cut to size from the sheet and glued to a stainless steel backing plate using epoxy resin glue. Following this step, Metco320 powder is thermally sprayed onto the top surface of the foam, using conventional spraying parameters to achieve a hard (72.5 R15y) and soft (55 R15y) abradable cap, where previous studies have shown a reducing elastic modulus as the abradable hardness drops [45].

All of abradable samples in this study are ground back to form a thin top surface cap (Figure 66), where grinding is ceased when the ligands of the foam are just exposed. Grinding was undertaken on an Ecomet Buehler grinding machine using 240 grit paper. This approach has been taken to ensure a uniform sample condition was achieved, and in turn investigate whether the abradable sample is able to collapse and compress in response to the incursion event. Additionally, given the penetration of the abradable material into the foam, should grinding back not be performed, the cap would be too thick and unlikely to deform when rubbed.

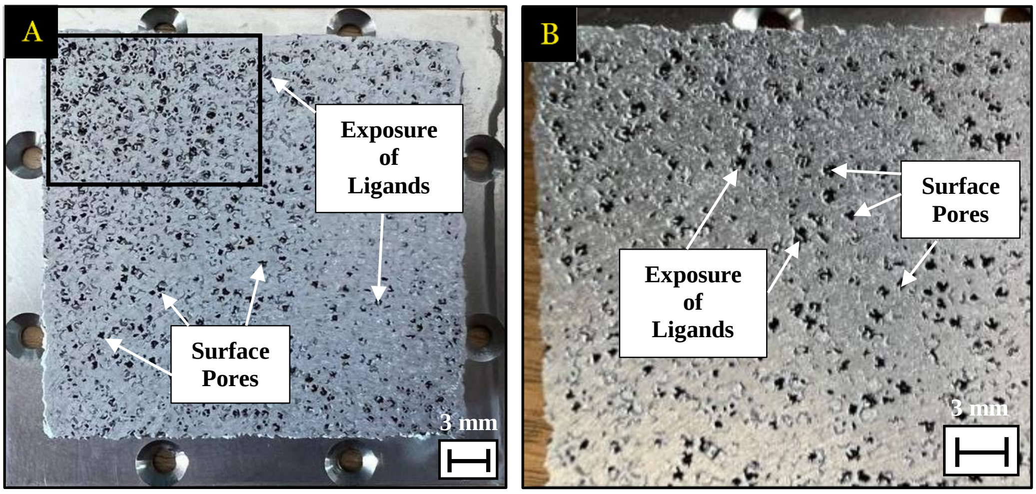

Figure 66. Ground cap surface macrostructure (A) and Surface enlargement and identification of key features and surface finish (B)

Figure 67 shows cross sections of the achieved abradable cap, with the backscattered image shown recorded using a TM3030Plus electron scanning microscope at forty times magnification. As shown in the Figure, the abradable material can penetrate up to 1.7 mm into the foam. However, it is also notable that there are many inconsistencies in penetration due to different pore locations within the metallic foam matrix. Areas of infiltration have been labelled, and furthermore the cap thickness can also be clearly identified. The two examples shown in Figure 67 are different samples which suggest that when grinding back there is consistency within the extent to which samples are ground. A range of thicknesses have been measured across the cross section for an average of 0.34 mm penetration depth.

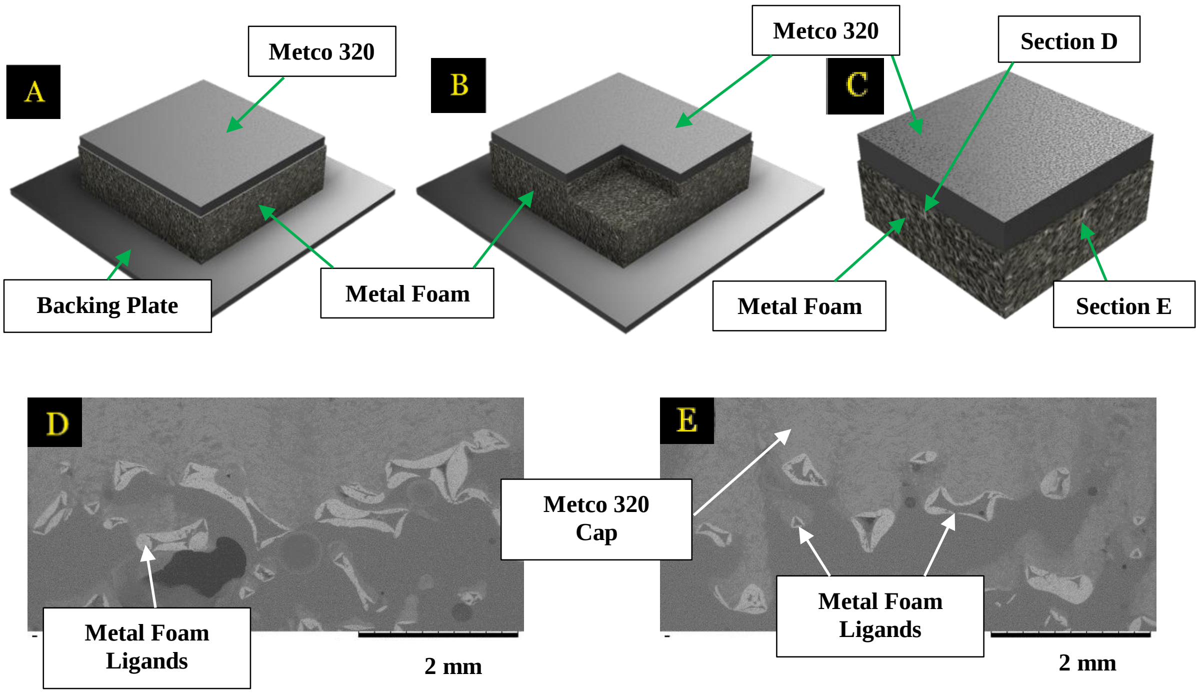

Figure 67. Schematic of A) showing a typical abradable capped foam where B) showing the remains once partition C) has been taken to observe representative cross sections D) & E)

Finally, Table 4 shows the test matrix, where for all metallic foam samples it should be noted that they were sprayed with the same batch of powder for consistency in microstructure. In each case, an initial cap thickness of 0.75 mm was sprayed onto the foam prior to grinding back, with hardness measured on the R15y scale as noted (Batch measured by Rolls Royce).

Table 4. Abradable Capped Foams Test Matrix

ID	Sample	Blade	Incursion Depth (μm)	Incursion Rate (μm/pass)	Tip Speed (m/s)	Cap - Hardness
1	Fine Foam	Inconel 718	2000	2	100	Soft (55)
2	Fine Foam	Inconel 718	2000	2	100	Hard (72.5)
3	Coarse Foam	Inconel 718	2000	2	100	Soft (55)
4	Coarse Foam	Inconel 718	2000	2	100	Hard (72.5)
5	Coarse Foam	Inconel 718	2000	0.2	100	Soft (55)
6	Coarse Foam	Inconel 718	2000	0.02	100	Soft (55)

All the abradable samples from this study are tested under the same blade speed of 100 m/s. However, varied incursion rates have been chosen, and are 0.02, 0.2 and 2 μm/pass to cover a range of engine operation conditions, where the maximum value tested is representative of pass-off and the minimum in-flight rub events [46][46].

7.2 Results

As noted, research around abradable capped foams is necessary to further understand the opportunities that such materials may offer for aero-engine sealing. This study aims to investigate the main factors that directly contribute to the way an abradable capped foam behaves during rub tests. In the results section, wear mechanisms and deformation behaviours will be investigated through the study of three main variables which include sprayed cap hardness, variation in metallic foam pore size and the effects of incursion rate. Firstly the effect of cap hardness is established on a coarse foam, before the role of pore size is explored for both soft and hard capped samples. Finally the influence of incursion rate on a coarse foam with a soft cap is presented.

7.2.1 Effects of Cap Hardness – Coarse Foam

In this section the effect of cap hardness is investigated on the coarse foam. In each case, the incursion rate is 2 μm/pass, blade speed 100 m/s and incursion depth 2000 μm. The two different cap hardness's referred to as soft and hard, have a hardness difference of 17.25 R15y, and are 55 R15y (soft) and 72.5 R15y (hard) respectively.

Figure 68 shows the rub surfaces post test (A) & (E), with leading blade edge (B) & (F), trailing blade edge (C) & (G) and blade tip (D) & (H). From the two rub surfaces it can be seen that a layer of abradable cap has been retained in both cases. However, in the case of the hard cap (Figure 68E), increased fracture and breakage of the surface occurred when compared to the soft cap (Figure 68A). Comparing the morphology of the rub surfaces further, it is also clear that compaction and deformation of the cap occurred more readily for the soft cap, given it's more continuous appearance. Conversely, the harder cap shows abrasion of the cap and reduced bulk deformation, where local fracture also occurs and propagates from the edges of the rub track. Whilst edge fracture similarly occurred for the soft cap, it is noticeable that in this case it is less than for the hard cap, and also does not lead to wider cracking of the abradable layer.

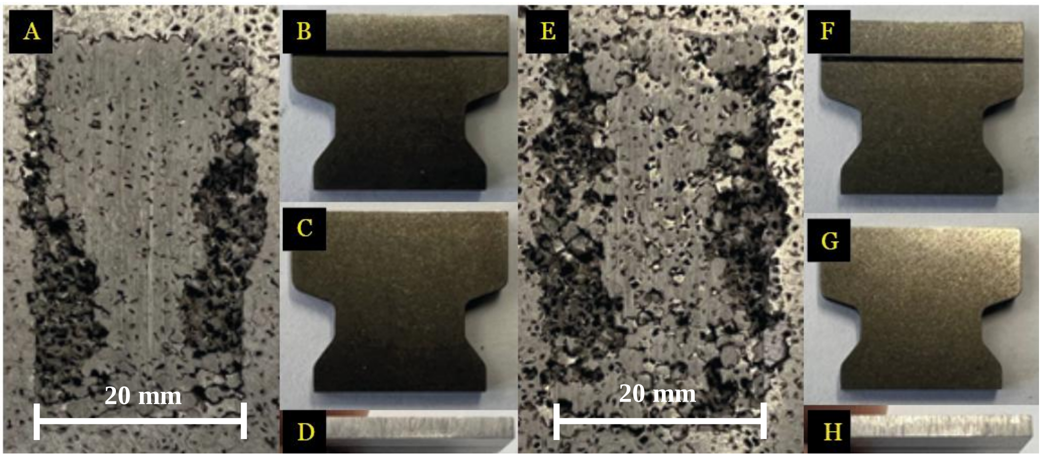

Figure 68. Test 3- Soft Cap: A) Rub Surface B) Leading Blade Edge C) Trailing Blade Edge D) Blade Tip – Test 4- Hard Cap: E) Rub Surface F) Leading Blade Edge G) Trailing Blade Edge H) Blade Tip

Table 5 shows blade mass measured before and after the rub tests. These measurements were performed in order to determine if either blade wear or adhesive transfer of material from the abradable had occurred, As shown in the Table, mass change is negligible for both tests, with a marginal amount of blade wear recorded in each case. These results are consistent with the images of the test blades shown in Figure 68, where Figure 68D and 68H for the tips of the blades from the tests with the soft and hard caps respectively, show scratches reflective of light abrasive wear.

Table 5. Blade weight change post and prior to rub tests

Sample	Mass Before (g)	Mass After (g)	Δ Mass (g)
Soft Cap (3)	4.37	4.36	0.01
Hard Cap (4)	4.36	4.35	0.01

Figures 69A & 69B show the forces and blade length change for the soft and hard cap tests respectively, plotted against rub length. Rub length has been previously identified as a suitable plot parameter for abradable linings testing [15], and represents the total sliding distance of the blade. As shown in the Figure, in both cases forces first rise to a peak, before reducing to a steady state level. However, in the case of the softer cap, this peak is higher, with the subsequent steady state value also similarly so. Whilst it may initially be counter intuitive that higher forces are recorded for the softer cap, when coupled with the observed wear scars, this is less surprising. As noted, the soft cap was observed to act as a compliant layer, triggering deformation of the underlying foam. Conversely, the stiffer hard cap was seen to primarily abrade and fracture, with the foam and abradable acting as discrete bodies.

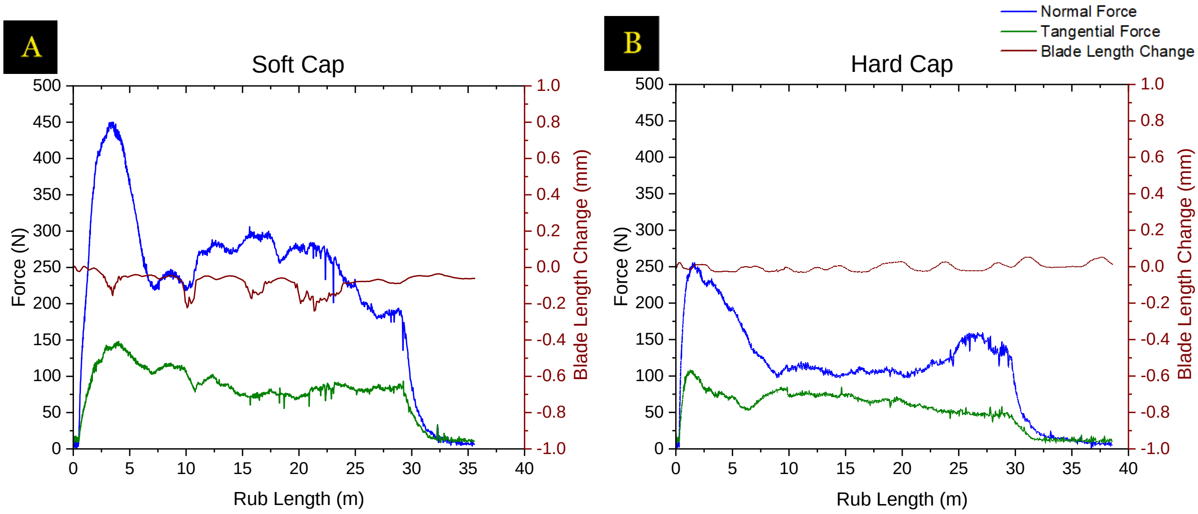

Figure 69. Force traces at fast incursion rates for A) soft and B) hard capped foams

The result seen for the soft cap is also consistent with a previous study investigating the effect of abradable hardness, where soft abradables were observed to rub as opposed to cut, and high normal forces develop [4]. Comparing the forces to tests conducted of just Metco 320, it is clear that the forces are lower by a magnitude of 2-3 times clearly suggesting that the abradable is managing the contact force [30]. This behaviour combined with the compliance of the soft cap itself is therefore likely to lead to the high normal forces and deformation of the cap and foam observed. Whereas, in the case of the hard cap, it's rigidity and ability to be cut, means that the blade instead removes the abradable, resulting in a lower build-up of normal force. In summary, Table 6 shows the maximum and average normal and tangential forces, along with force ratio, where the previous highlighted differences in normal force and force ratio are evident. In the Table, it is also notable that whilst tangential forces for the two tests are similar, the ratio of tangential to normal forces is higher for the hard cap, with an increase in this value linked to a transition to cutting as opposed to rubbing, further supporting the view that the hard cap is cut by the blade.

Table 6. Maximum and average forces in the normal and tangential directions for soft and hard capped foams, additionally a force ratio.

Sample	Max NF (N)	Max TF (N)	Mean NF (N)	Mean TF (N)	Force Ratio
Soft Cap (3)	450.16	148.01	223.74	79.15	0.354
Hard Cap (4)	225.30	108.16	108.83	54.09	0.497

Finally, considering the observed cracking and increased rupture of the hard capped foam, this is likely linked to the outlined wear mechanic. Whilst as noted forces are lower for the hard cap, it's high stiffness results in the cap and foam acting as independent bodies, meaning poor energy transfer occurs. In turn, this will result in the energy from the rub that is not relieved via material removal, being concentrated in the near surface, resulting in the observed rupture of the foam ligands. This aspect of the behaviour of the capped foams will be further explored in the subsequent discussion, where material sections will investigate the level of compliance of the foam, alongside any damage.

7.2.2 Effects of Pore Size – Soft Cap & Hard Cap

As previously noted two foam sizes have been investigated, a fine (1200 μm) and coarser (2000 μm) foam. In this section, results are presented for both foam types, with either a hard or soft cap, once again at a high incursion rate condition of 2 microns per pass.

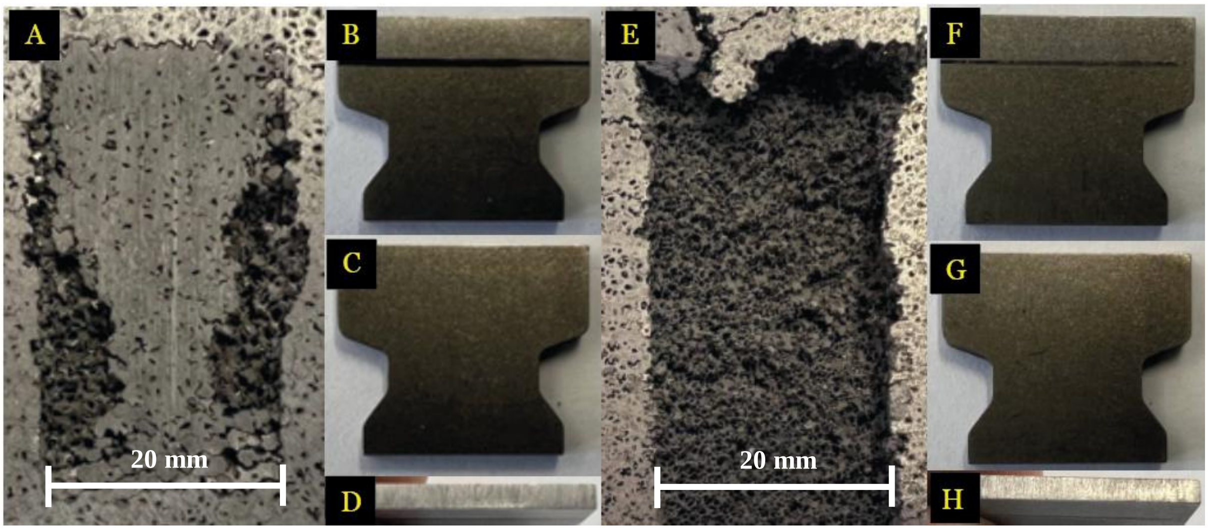

Figure 70. Test 3 - Coarse Foam: A) Rub Surface B) Leading Blade Edge C) Trailing Blade Edge D) Blade Tip – Test 1- Fine Foam: E) Rub Surface F) Leading Blade Edge G) Trailing Blade Edge H) Blade Tip

Figure 70 shows the results for the two foam sizes for the soft cap. In the Figure, the previously detailed result for the coarse foam with the soft cap is shown, alongside that for the fine foam with a similar soft cap. At this point it should be noted that mass loss measurements were similarly made for the blade samples both pre and post-test, with negligible changes once again observed, combined with light abrasion marks similarly on the blade tips. As shown in the Figure, where previously for the coarse foam the cap to a large degree remained at the end of the test, with deformation observed in the underlying foam, in the case of the fine foam, the cap has been removed. Further investigation determined that the cap delaminated from the foam surface, and this will be further investigated via the force measurements recorded (Figure 71).

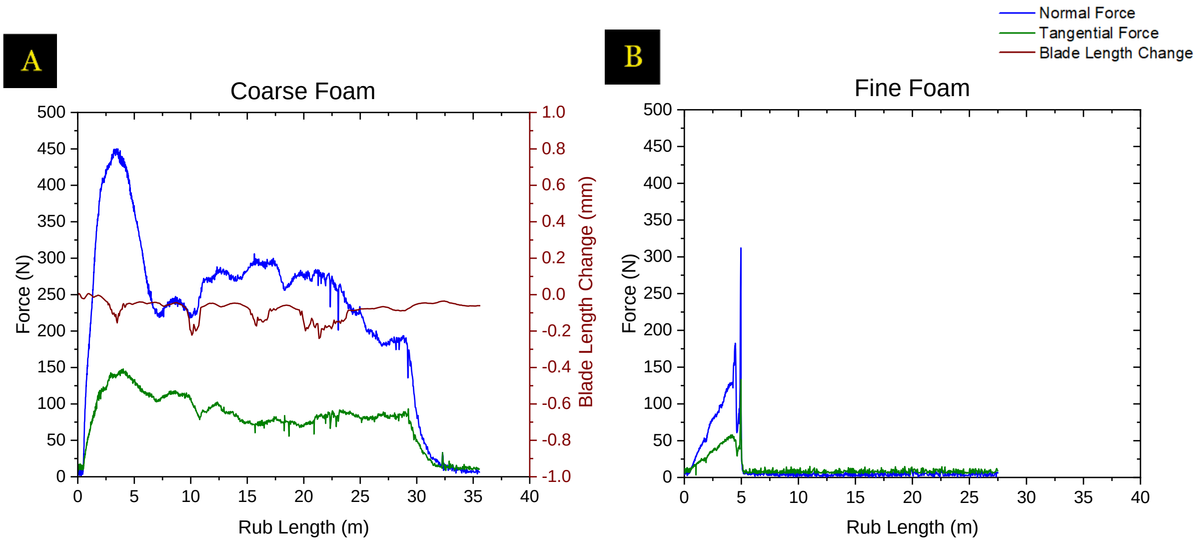

Figure 71. Force traces for soft cap where A) coarse foam and B) fine foam

As shown in the Figure, whilst in the case of the coarse foam forces first peaked before plateauing to a steady state, for the fine foam failure occurred in the initial stages of the test as the forces began to rise. This result is consistent with a previous study, where it has been seen that smaller pore sizes result in localised stress and strain accumulation within the upper layers of the foam, with this providing an explanation as to why delamination has occurred at the foam – cap interface. Considering this result in the context of that previously seen (Section 7.2.1) for the coarse foam with the hard cap, it is likely that the increased stiffness of the fine foam, has similarly led to the foam and cap behaving as independent bodies, resulting in a similar although more extreme failure.

Maximum and average forces for the tests, alongside force ratios are shown in Table 7, where it is noticeable that failure of the fine foam occurred at a lower normal force than the coarse foam sustained, further highlighting the likely role of stress concentrations in the failure observed. It is also notable that whilst stiffer overall, the individual ligands of the fine foam are weaker when compared to the coarse foam, meaning they are also more susceptible to failure in such cases.

Table 7. *Maximum and average forces in the normal and tangential directions for coarse and fine foams*

Sample	Max NF (N)	Max TF (N)	Mean NF (N)	Mean TF (N)	Force Ratio
Coarse Foam (3)	450.16	148.01	223.74	79.15	0.354
Fine Foam (1)	312.05	133.30	24.48	15.63	0.638

Finally, moving to the test performed with the fine foam with the hard cap, almost immediate failure was recorded. Considering the previous result for the coarse foam with the hard cap (Figure 68E), where the stiffness of the cap was identified as leading to the cap and foam acting as discrete bodies, combined with a similar effect identified for the fine foam with the soft cap (Figure 70E), it is unsurprising that was the case. Clearly, the combination of the hard cap with the fine foam accentuates the identified issue, leading to the almost instantaneous rupture observed at the foam – cap interface.

7.2.3 Effects of Incursion Rate – Soft Cap & Coarse Foam

The final tests in this chapter compare the effect of incursion rate for the coarse foam with the soft cap. In addition for the previously presented result for this material at an incursion rate of 2 microns per pass in section 7.2.1, results are now presented at 0.2 μm/pass and 0.02 μm/pass. This material combination was chosen to explore the influence of incursion rate, as it represented the most promising foam-abradable system.

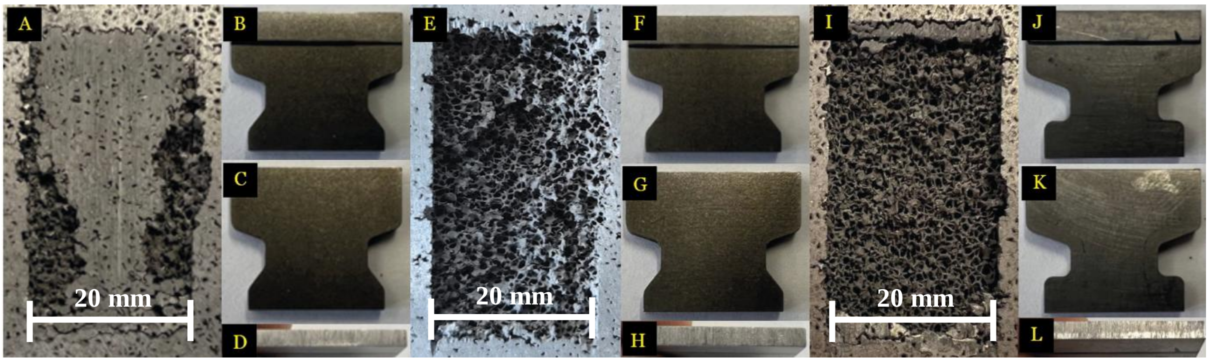

Figure 72. Test 3 - 2 μm/pass: A) Rub Surface B) Leading Blade Edge C) Trailing Blade Edge D) Blade Tip – Test 5 - 0.2 μm/pass: E) Rub Surface F) Leading Blade Edge G) Trailing Blade Edge H) Blade Tip – Test 6 - 0.02 μm/pass: I) Rub Surface J) Leading Blade Edge K) Trailing Blade Edge L) Blade Tip

Figure 72 shows a comparison of the rub surfaces and blades at different incursion rates. As previously detailed, at 2 μm/pass (Figure 72A) deformation of the cap/foam system occurred. Moving to incursion rates of 0.2 and 0.02 μm/pass (Figures 72A & 72I respectively), significant differences can be seen in the rub surfaces, with removal of the cap having occurred. As might be expected, little to no wear of the blades has occurred as a consequence of the cap detachment, with this result confirmed via mass change measurements. The force measurements for these two tests are plotted against rub length in Figure 73, and as shown in the Figure, forces are low throughout the test, although it is unclear at what point detachment occurred.

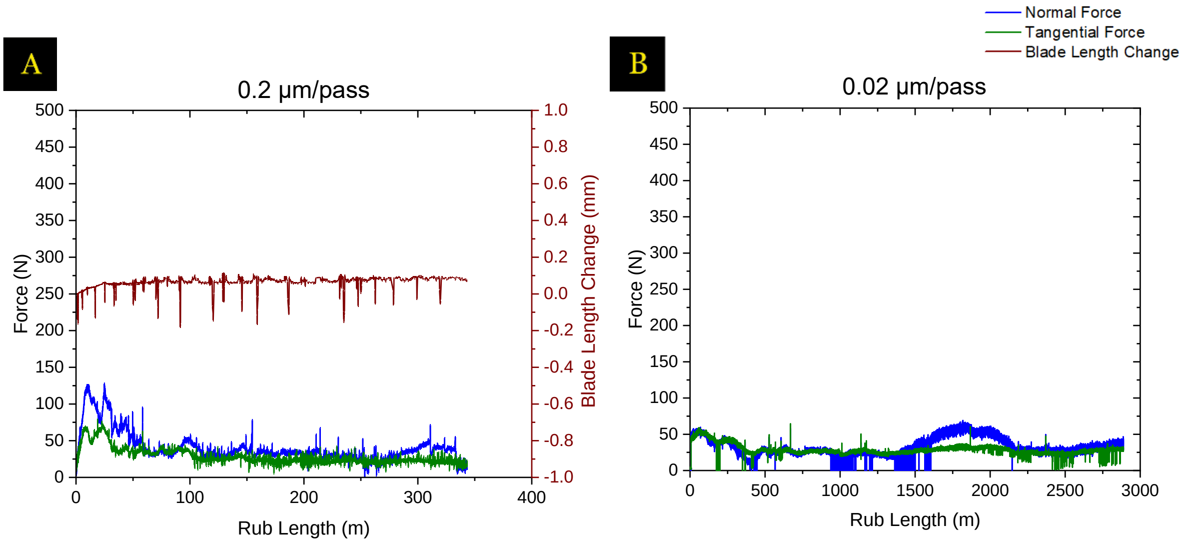

Figure 73. Force traces for soft cap where A) 0.2 μm/pass and B) 0.02 μm/pass

In order to compare forces across the three incursion rates investigated, average and maximum forces are once again detailed, and are shown in Table 8. In this case, force ratio has been omitted given the low values of force recorded at the lower two incursion rates leading to significant variability in the data, albeit with this indicative of an intermittent rubbing contact. As shown in the Table, forces recorded at incursion rates of 0.2 μm/pass & 0.02 μm/pass are significantly lower than those seen at 2 μm/pass, with this providing an explanation for the behaviour observed. Previous work has shown that at faster incursion rates, energy input into the system per strike of the blade is higher [47], and although for these tests a soft compliant cap has been used, a given amount of energy will still be required to actuate the cap and trigger deformation of the cap / foam system. Given the low values of force recorded for the latter incursion rates, it is likely that this threshold was not reached, and energy was once again concentrated at the cap / foam interface, leading to the observed failure. However, from the data it is unclear as to whether initial cutting of the cap occurred or a more instantaneous failure, and this will be further explored in the next section.

Table 8. Maximum and average forces in the normal and tangential directions for different incursion rates

Sample (µm/pass)	Max NF (N)	Max TF (N)	Mean NF (N)	Mean TF (N)
2 (3)	450.16	148.01	223.74	79.15
0.2 (5)	168.65	72.54	49.30	30.30
0.02 (6)	69.10	64.42	33.06	30.81

7.3 Discussion

In order to further investigate the wear mechanisms present, samples were vacuum impregnated, mounted and sectioned. This approach was undertaken in order to determine to what degree the abradable cap was preserved post-test, as well as to investigate collapse of the foam and in turn accommodation of the rub. In addition images recorded using the high speed camera were also analysed to further investigate the progression of the material removal mechanism, with images presented at incursion depths of 500 µm, 1000 µm, 1500 µm and 2000 µm. In combination, the further analyses detailed are used to further discuss the influence of cap hardness, foam pore size, and incursion rate.

7.3.1 Soft vs Hard Caps

As previously highlighted, for the soft cap with the coarse foam, progressive collapse of the underlying foam was identified, where forces first peaked before plateauing to a steady stage value. As shown in Figure 74, when viewed in combination with the force data, images taken from the high speed camera support this view, where gradual collapse of the rub track is evident. From these images, it can also be determined that rupture of the abradable cap only occurs at the edges towards the end of the rub event, with this likely linked to edge tearing as the cap is further pressed into the foam.

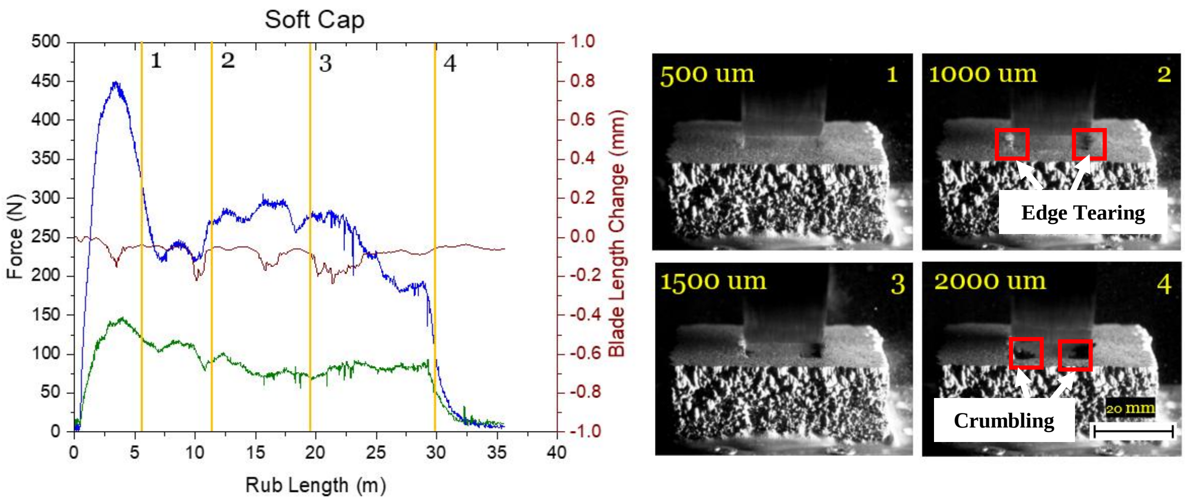

Figure 74. Rub progression stages at different set incursion depths for a soft-capped coarse foam abradable at 2 microns per pass

These observations are supported by the material sections shown in Figure 78, where a broadly uniform cap of abradable material (1.2 mm) is preserved along the centre line of the rub in the direction of blade travel, with this accompanied by collapse of the underlying foam structure. Conversely, at the edges of the rub track, tearing is evident, with both abradable cap and the underlying foam structure removed.

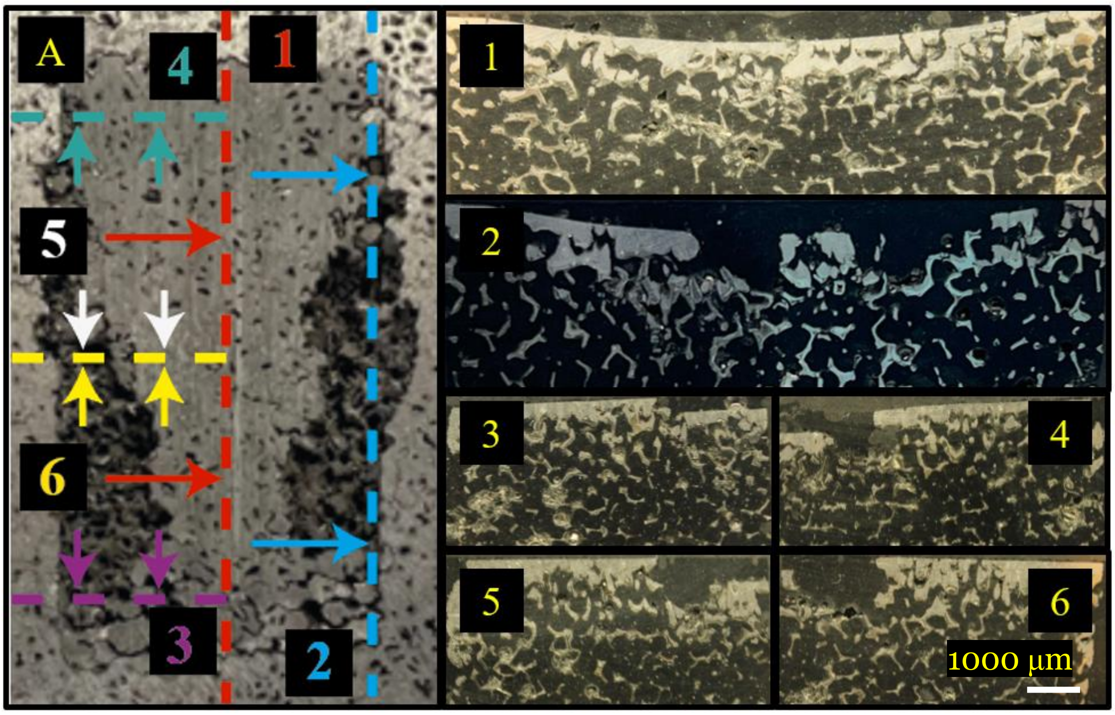

Figure 75. Soft capped coarse foam abradable showing sections in different planes

Moving to the test with the hard cap and coarse foam (Test 4), significant differences can be observed. As previously noted, forces were at a lower level, with this determined to be due to cutting of the abradable cap. As shown in Figure 76, a pronounced rub track is visible on the sample from as early as 500 microns into the rub depth, where this was more limited in the case of the soft cap at the same stage. This highlights the differing wear mechanic present for the two samples, where in the case of the soft cap material is compressed, until ultimately the foam deforms, where for the hard cap it is removed via cutting.

This view is further supported by the section taken through the hard capped foam. As shown in Figure 77, where it can be seen along the centre line of the rub track in the direction of blade travel, that the cap is thinned (0.3 mm), with little to no compaction of the underlying foam. At the same time, as was the case for the soft capped foam, tearing has similarly occurred at the edges. Whilst this latter observation doesn't imply large scale compaction of the foam has taken place, and oppose the result observed for the centre line, it does suggest more generally that a small level of deformation may be taking place, as if the abradable was being completely cut, such tearing would not take place

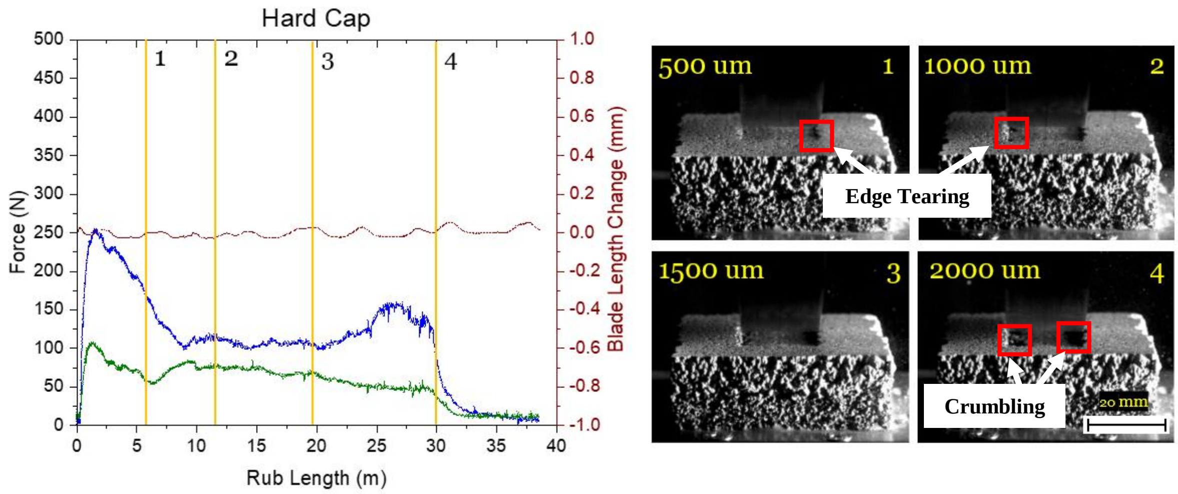

Figure 76. Rub progression stages at different set incursion depths for a hard-capped coarse foam abradable at 2 microns per pass

As previously noted, there are differences in the amount of cutting visible after sectioning of the abradable samples post-test. Converting the images to greyscale, and then segmenting them into metallic & porous phases by separating the light and dark phases. The amount of cutting that has taken place can be inferred from the remaining metallic material in the near surface, given the cap is significantly more dense than the foam. In turn, a numeric assessment can be made as to whether more cutting has indeed taken place for the hard cap.

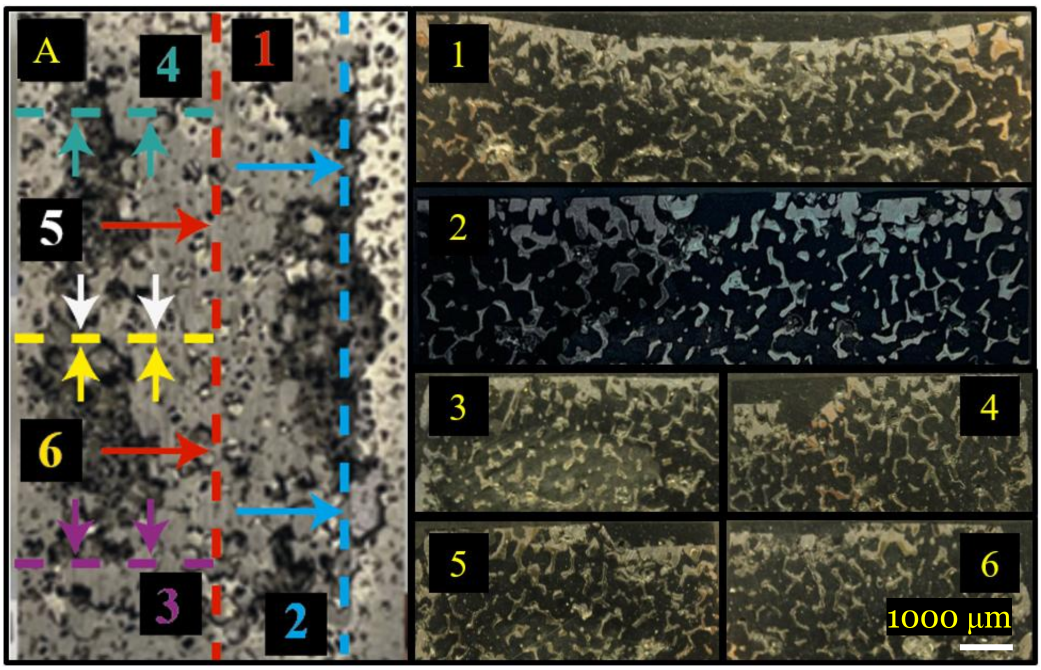

Figure 77. Hard capped coarse foam abradable showing sections in different planes

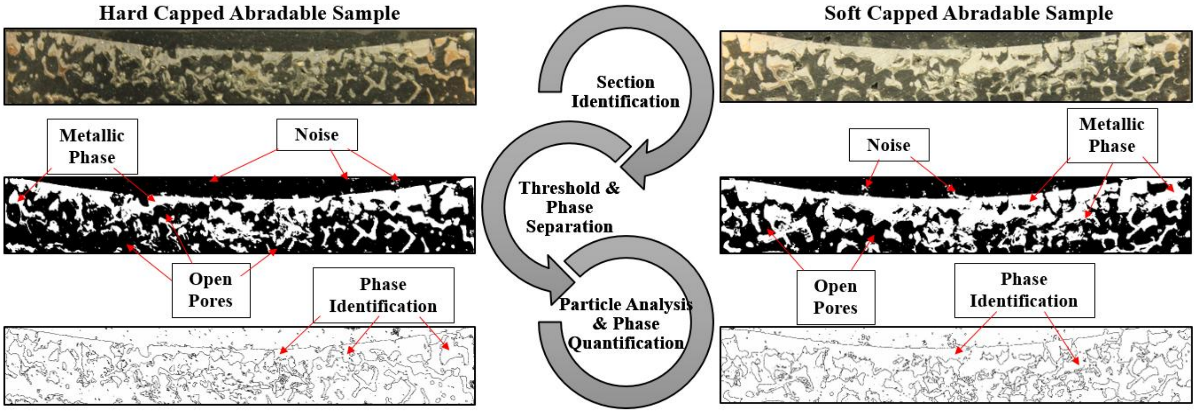

Figure 78. Analysis steps for quantification of metallic phase remains over the same section area, including threshold and porosity percentage

Following the analysis detailed in Figure 78, the determined metal percentage in frame for both the hard and soft caps is 33.5 % and 43.5 % respectively. Whilst there will be some discrepancies due to the metal ligand phase having varied percentage quantities dependant on the section taken, this has been minimised by capturing as little metallic foam. Even taking into account such discrepancies, the outcome still remains evident that for the soft cap an additional 10 % material has been retained. Reflective of the compaction taking place. In the case of the hard cap, the material loss determined can be associated with an increase in cutting.

7.3.2 Compaction

As highlighted in the results section, the variables of cap hardness, pore size, and incursion rate are broadly linked in terms of the wear mechanism generated, and the response of the abradable capped foam to the incursion event. In the case of a hard cap, the abradable and foam act as discrete elements, with material being removed by the blade from the top surface of the abradable, whilst at the same time some energy from the interaction is transferred to the underlying material. This latter energy transfer and compression of the system is in particular evidenced by the edge tearing seen for these samples. However, given the lack of compliance of the hard cap, and in turn inability to actuate the foam, energy is stored in the near surface and rupture occurs. In many respects this is similar to the wear mechanic seen for nickel based abradable materials at moderate and high incursion rates [28], where material removal fails to keep pace with the incursion rate, and compression followed by surface rupture of the sample occurs.

Edge cracking is due to the compaction beneath the blade, the cap is being pushed downwards causing the areas at the edge of the blade crack in accommodation of the strain where areas not directly underneath the blade remain at the original position.

In a similar way, when the foam is stiff, regardless of the compliance of the abradable cap, a related wear mechanism occurs. For this case, the foam and abradable again act as single bodies, with energy once more being stored in the near surface, should the rub not be accommodated by removal of the abradable by the blade. This in turn leads to ligand failure, and delamination of the abradable cap.

Finally, as seen in the case of the coarse foam with the soft cap at reducing incursion rate, failure once gain occurs. Given that the reducing incursion rate is accompanied by a reduction in normal force [48], this creates a situation where the energy input is not sufficient to globally deform the foam, and in many respects is similar to the situation where the cap is either too hard or foam too stiff. Different stages of rub progression shown in Figure 79 clearly highlight the localised failure of the cap where no global deformation occurs.

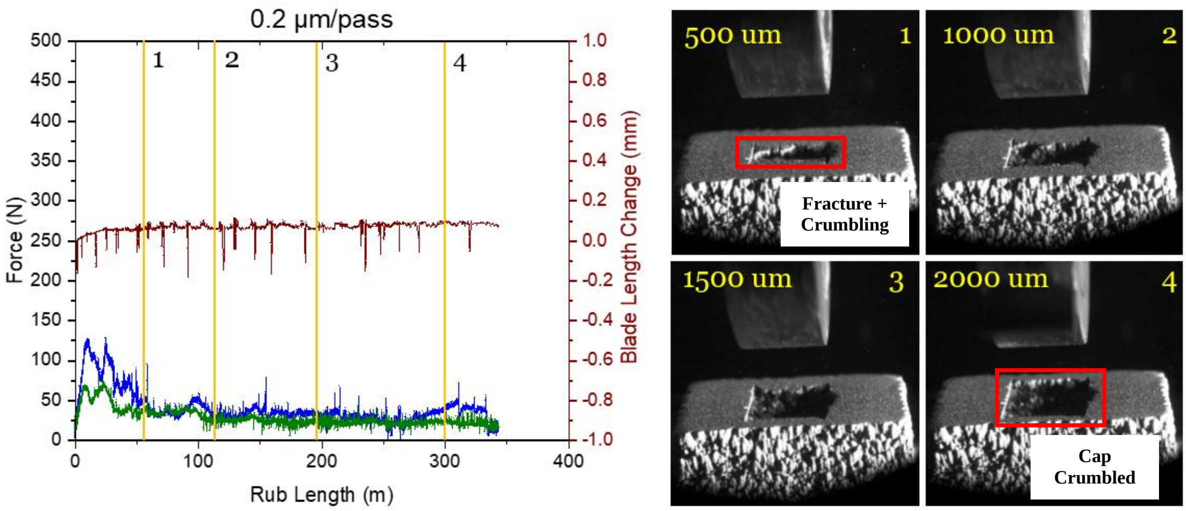

Figure 79. Rub progression stages at different set incursion depths for a soft-capped coarse foam abradable for a lower incursion rate

These inter relationships are highlighted in Figure 80, where as shown the only sample to achieve energy transfer and deformation of the foam and cap, was the coarse foam sprayed with the soft abradable. On this point, it is interesting to note that in this case the soft abradable was both advantageous given the fact it had a lower elastic limit [46], and also in that it didn't readily cut, meaning normal forces were high [47]. In particular this latter point is opposed to conventional research into abradable materials, where a failure to dislocate, can lead to high forces and temperatures, and in turn blade wear. However, in this case, given the need to actuate the foam sample it was of benefit.

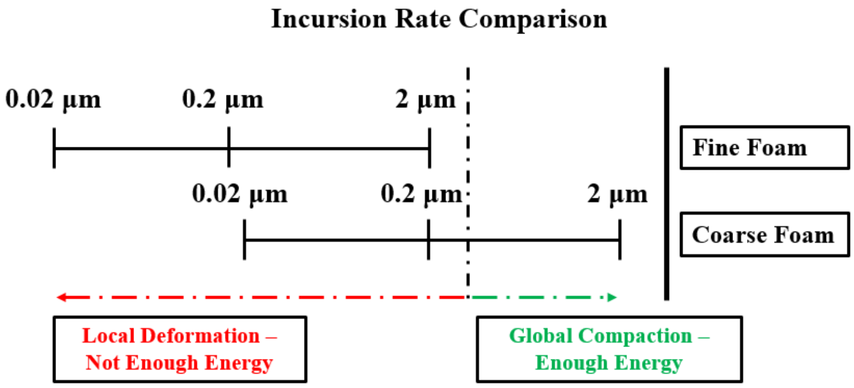

Figure 80. Links between incursion rate and pore size for mechanism activation

7.4 Conclusion

These series of tests have been performed investigating the rub response of abradable capped metal foams, with the aim of creating a hybrid material that is able to collapse and conform to the blade incursion event. It was identified that the compliance of the cap along with the stiffness of the foam were key variables, where if either the abradable cap was too hard or the foam too stiff, deformation of the underlying foam did not occur, and instead sample failure took place. Similarly, whilst good results were achieved in the case of a soft cap on a coarse foam, deformation of the hybrid material was reliant on sufficient actuation through a high incursion rate, as the incursion rate was linked to the force input to the system. In cases where the incursion rate was reduced, failure to deform the material and accommodate the incursion once again occurred, with a failure similar to that seen for hard abradable caps or stiff foams. Finally, whilst considering detrimental to abradability in more conventional settings, soft abradables were found to be of benefit in this study, as the rubbing as opposed to cutting present promoted higher normal forces, leading to the desired deformation of the foam material. Edge tearing was also identified as an issue due to the discontinuity at the extremities of the rub track, and alleviating this represents a topic of further work.

Chapter 8

Patterned Abradable Capped Metallic Foams

Abradable capped metallic foams have been previously investigated to show interesting deformation and wear mechanics during rub tests. Previously investigated filled metallic foams lack the temperature capabilities required for the compressor stages of an aero-engine, following on conventional abradable material in the form of Metco 320 (AlSi/hBN) has been extensively tested as a cap with an underlying layer of metallic foam where desirable mechanisms such as collapse and compression exist within the metallic foam phase during rub tests.

Abradable capped foams show excellent compression and fracture mechanics under fast incursion rate rub test conditions, their tendency to collapse and create compaction zones allows for deformation conformity with little debris. Such mechanics however have only been observed to occur effectively at the fast incursion rates where enough energy input into the system allows for actuation. Commonly seen is an initial force peak where the abradable foam and cap compact followed by cutting and material removal.

The work in this chapter aims to investigate how actuation of these mechanisms mentioned can be triggered through a series of fault lines within the abradable cap. This is achieved through metallic masks placed over the metallic foam for the spraying process, this ensures that areas where fault lines exist in areas where the mask pattern covers the top surface.

8.1 Test Samples and Details

The metal foam material substrate used is commercially sourced, this is manufactured by Recemat BV under the trade name NC1116. Manufactured through a heat treatment process, variation in parameters is to be considered when selecting a suitable base metallic foam complex for which the cap will sit on top. Key properties of the foam can be modified to allow an excellent selection for the type of metal foam used in this series of tests, previously tested a coarse foam with a larger pore size shows better collapse and a lower overall material stiffness. Softer caps are desirable with its reduction in stiffness and ability to actuate more of a compaction and compression mechanism whereas for a harder cap the cutting mechanism takes over to thin the cap surface with more local deformation. After extensive testing previously carried out a soft coarse foam has been decided to be the base criteria for this series of tests.

Following the foam selection, Metco 320 powder is thermally sprayed onto the top surface of the foam using conventional spraying parameters to generate a soft cap layer, previous studies have shown that as the hardness of the abradable drops a reducing elastic modulus (material stiffness) similarly occurs. Metco 320 a conventionally used and commercially sourced coating for abradables within the compressor stages of an aero-engine, an aluminium silicon alloy powder matrix with an addition of hexagonal boron nitride (hBN) composite. Operable up to 450 °C including improved corrosion resistance is very desirable when in combination with a metallic foam can still work effectively. The role of the hexagonal boron nitride (hBN) is to act as an inert lubricant, with such a reduction of frictional heating in the blade contact an improvement in abradability exists. Furthermore, hexagonal boron nitride within the metallic matrix creates weaker interparticle bonding to allow for easier material removal where there is contact with the blade.

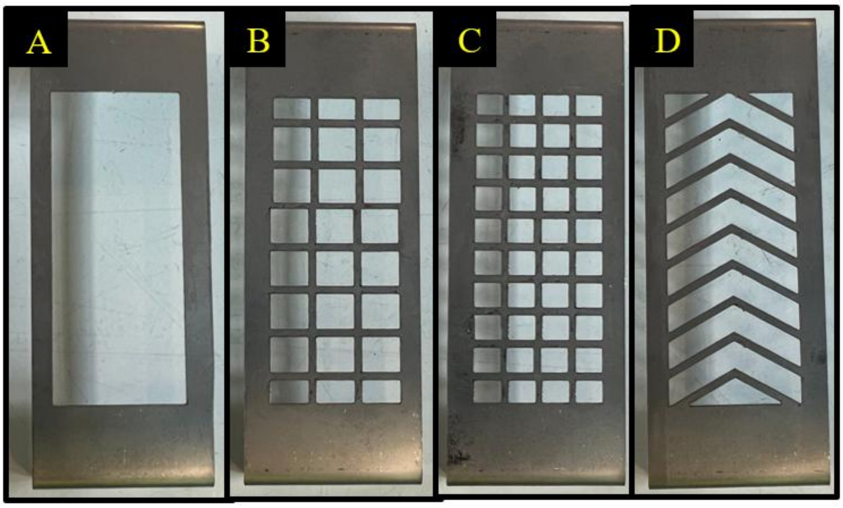

Figure 81. Metallic mesh plates for spraying procedure showing four Types A - D

Afore the mentioned fault lines are introduced to further actuate certain mechanisms seen to occur within capped abradable foams. Figure 81 shows the different mesh designs which are used to allow fault lines to be generated on the top rub surface, these design are specially chosen to investigate which type of tracks help to promote fracture and deformation is a more controlled manner.

Ground capped foams have shown a unique phenomenon known as global compaction and deformation, this is where the cap and foam abradable structure allows for efficient dissipation of the input energy through fracture of ligands and global compaction of the rub surface. Prior to grinding back hardness tests are conducted on a sample of the same powder batch (measured on the R15y scale), this is to provide an indication of material hardness between different batches. There is difficulty in controlling the cap thickness using conventionally sprayed parameters and conditions, the samples in this study are ground back in preparation for rub tests. The thin top surface cap is achieved using an Ecomet Buehler grinding machine using 240 grit paper and a rotation speed of 200 rpm, this approach has been taken to ensure that the sample condition is uniform and consistent. Figure 82 shows the step by step process through which samples are prepared for rub tests.

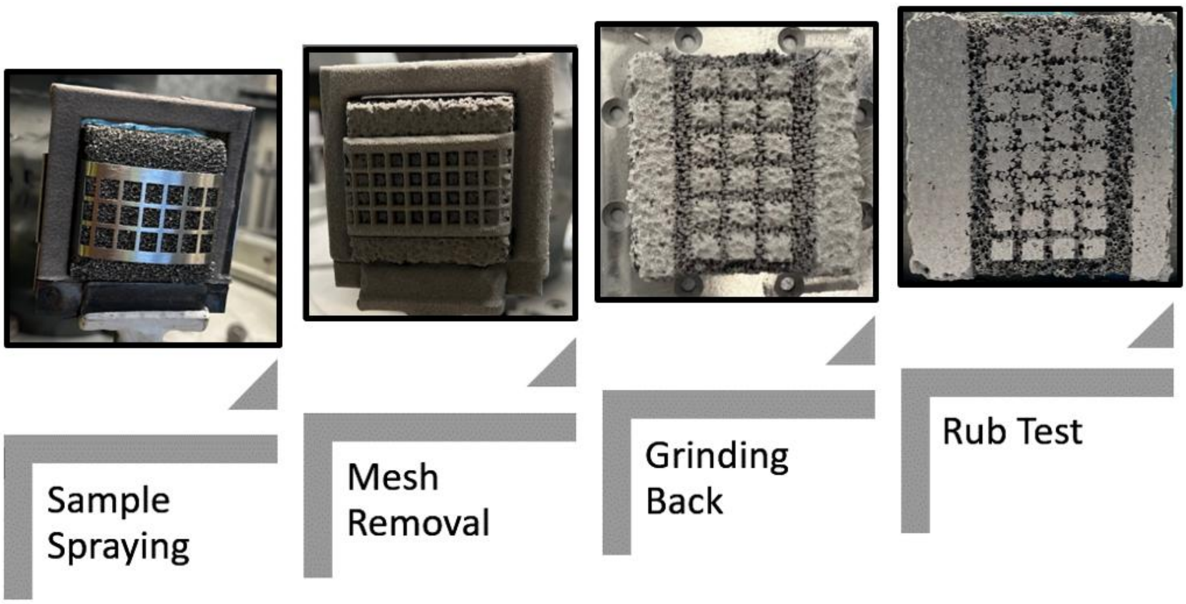

Figure 82. Step by step process for sample preparation

After this step by step process of sample preparation shown in Figure 82, samples are ready for rubs tests. Figure 83 shows an example of the six mesh pattern foams ready for testing after being ground back to reveal a thin top surface cap where metallic ligands from the underlying foam start to reveal themselves through the top surface.

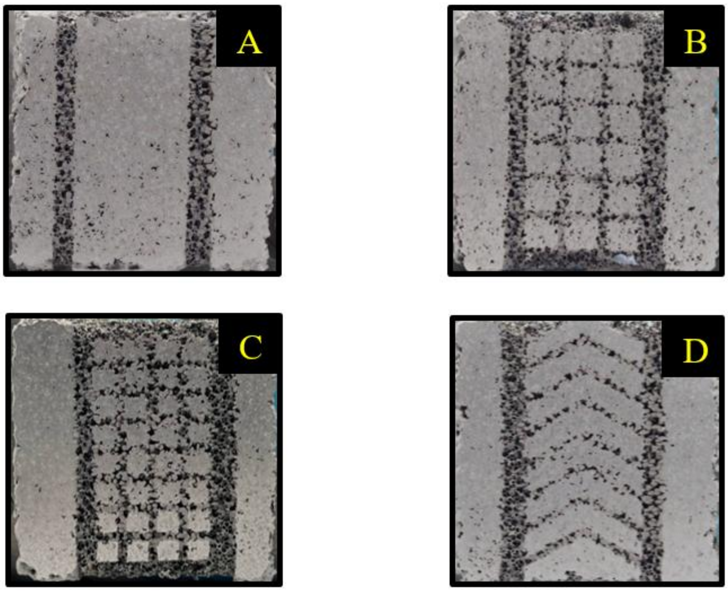

Figure 83. The four different patterned mesh designs ready for testing

To confirm whether mesh foams are a feasible solution to promoting more desired wear behaviours during rub tests, preliminary tests have been conducted. All abradable samples for this study are to be tested under the same blade speed condition of 100 m/s, at 100 m/s representative wear mechanisms can be seen, additionally due to the nature of the metallic foam structure at faster tips speeds of 200 m/s the results would be catastrophic.

Table 9. Test matrix for mesh pattern foams

Sample	Foam Type	Blade	Incursion Depth (µm)	Incursion Rate (µm/pass)			Tip Speed (m/s)	Cap - Hardness
Type A	Coarse Foam	Inconel 718	1500	2	1	0.2	100	Soft (60)
Type B	Coarse Foam	Inconel 718	1500	2	1	0.2	100	Soft (60)
Type C	Coarse Foam	Inconel 718	1500	2	1	0.2	100	Soft (60)
Type D	Coarse Foam	Inconel 718	1500	2	1	0.2	100	Soft (60)

Table 9 shows a test matrix with an incursion rate of 2 µm/pass, for a given foam design 2 µm/pass is first tested and if successful 1 and 0.2 µm/pass. This has been chosen as 2 µm/pass was seen to previously actuate a foam where there aim of this Chapter is achieving the same behaviour at lower force using incursion rate as a cut off criteria for testing.

It should be noted that the metallic foam samples were sprayed with the same batch of powder for consistency in microstructure and cap hardness. In each case, an initial cap thickness of 1-

1.5 mm was sprayed onto the foam prior to grinding back however are all ground back to the same criteria where visually metallic foam ligands start to become visible along the top surface.

The samples tested in Chapter 7 were achieved up to an incursion depth of 2000 µm, in these series of tests as shown in Table 9 the incursion depth has been altered to 1500 µm. In order to assess the pre fracture state, previous testing shows that up to this altered incursion depth it is possible to retain this condition for further analysis techniques.

8.2 Results

8.2.1 Tests at 2 µm/pass

In this section the feasibility of adding in fault lines within the top cap surface of capped metallic foams will be tested. In each case, the incursion rate is 2 um/pass, blade speed 100 m/s and incursion depth 1500 µm. The different sample designs are referred to as A-D as shown in Figure 83, these have all been tested.

Figure 84 shows the results after testing Type A at the fast incursion rate at an incursion depth of 1500 µm showing the rub surface post-test (A & E), with leading blade edge (B), trailing blade edge (C) and blade tip (D). The surface shows signs of fracture and local deformation however only at the edges, edge tearing is prominent however considering the main rub area little to no local surface fracture with compaction clearly evident in 84E. It is likely to be compaction as the abradable has conformed to the blade arc much like the sectioned tests in Chapter 7.

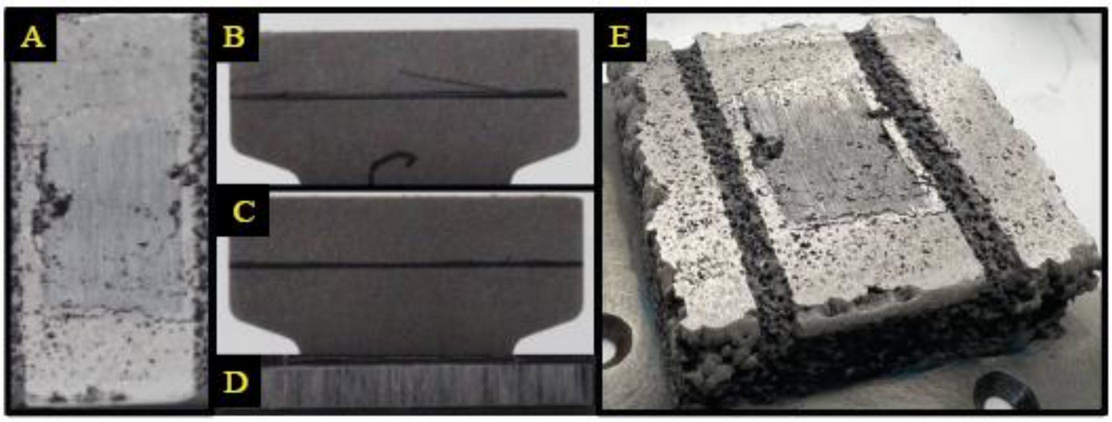

Figure 84. Type A at 1500 µm incursion depth and fast incursion rate: A) Rub Surface, B) Leading Blade Edge, C) Trailing Blade Edge, D) Blade Tip, E) Rub Surface

Typically for Metco 320 thermally sprayed abradables there is a lot of blade adhesion of the abradable depositing onto the blade, the absence of blade adhesion in this test is likely to suggest that there is more compaction present. The smaller amount of edge tearing seems to imply that the two fault lines in line with either side of the rub path has helped to reduce the surface material damage.

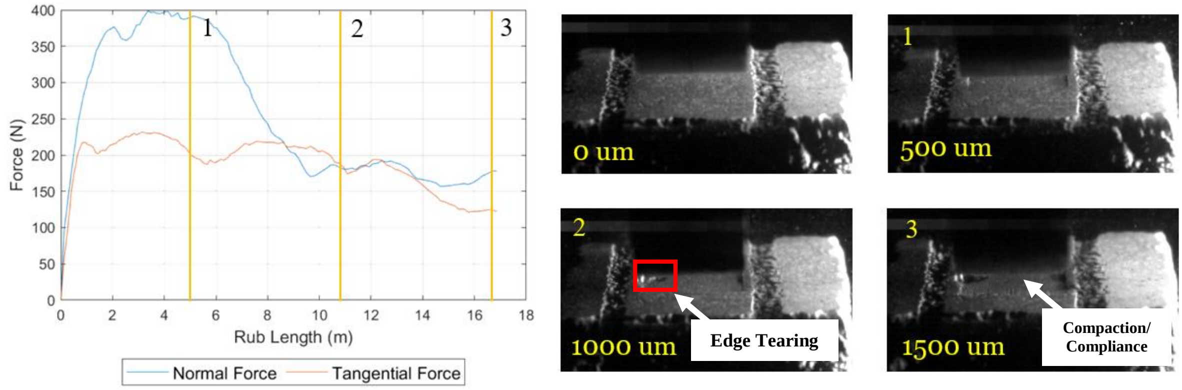

Figure 85. Progression of rub at 1500 µm depth for Type A at 2 µm/pass showing the 3 stages of rub representative of the different incursion depths: 500 µm, 1000 µm, 1500 µm

The progression of rub in Figure 85 shows the extent to which compaction occurs, this is prominent from the early stages and further up to the latter stages of rub. Observing the compaction mechanism from the rub progression, the initial force peak confirms these observations. For an abradable capped foam an initial force peak is typically representative of a large compaction mechanism which progresses and further stabilises as the extent of compaction reduces as the test continues through to the mid and latter stages of rub.

Moving to the second foam design Type B is composed of tile tracks of same size to help promote deformation of the abradable in the direction of the normal force, the local weak points can help to control where fracture and ligament deformation occurs. Figure 86 shows the results for Type B at the fast incursion rate showing promising results where the rub surface is able to maintain a large portion of the surface and subsurface material. The rub surface in Figure 6A shows that the fracture and deformation can be seen to be located where the fault lines are present, edge tearing is yet again seen and where this has occurred local subsurface fracture and eventual cap removal.

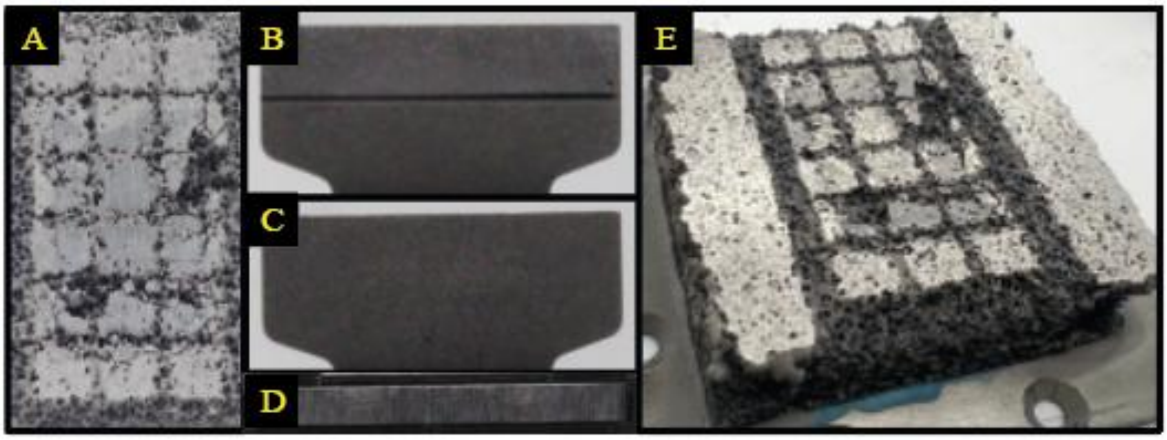

Figure 86. Type B at 1500 µm incursion depth and fast incursion rate: A) Rub Surface, B) Leading Blade Edge, C) Trailing Blade Edge, D) Blade Tip, E) Rub Surface

The blade images shown in Figure 86A, B and C show again little to no blade damage or adhesive signs, this is likely to suggest either cutting or compaction of the abradable substrate. 86E shows the rub surface post-test where the angle of capture can clearly show the extent to which compaction has occurred.

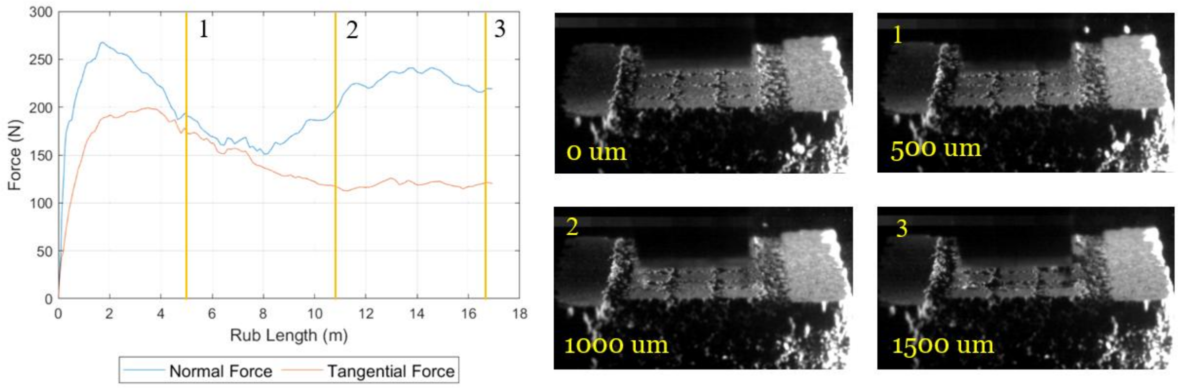

Figure 87. Progression of rub at 1500 µm depth for Type B at 2 µm/pass showing the 3 stages of rub representative of the different incursion depths: 500 µm, 1000 µm, 1500 µm

The force data in Figure 87 shows that initially there is a force peak similarly to all capped foam substrates however unlike most this doesn't stabilise and it is evident that there is a second force peak. As there is no blade adhesion or damage as well as very little surface damage or delamination it can be hypothesised that a compaction release mechanism is in place. This mechanism is where the blade keeps pushing and compacting to a point where the underlying metallic foam will collapse directly underneath the abradable cap. Following this event the force will drop as shown in the graph and a similar event will then proceed to occur as the next underlying metallic foam layer will compact and deform with more and more energy from the blade to abradable contact. The rub progression in Figure 87 also confirms that there is a large amount compaction not only in the early stages of rub however progressive towards the end of the test, as the rub surface is maintained in a pre-fracture state it can be further analysed to understand how the internal structure has behaved.

Type C represents a similar pattern to B, although in this case the foam types are smaller (Figure 88E). Additional fault lines are generated to further help to dissipate the energy into the system through the ability to control the locations of where deformation should occur. As follows Figure 88 shows the abradable surface and relevant blade images to show post-test results.

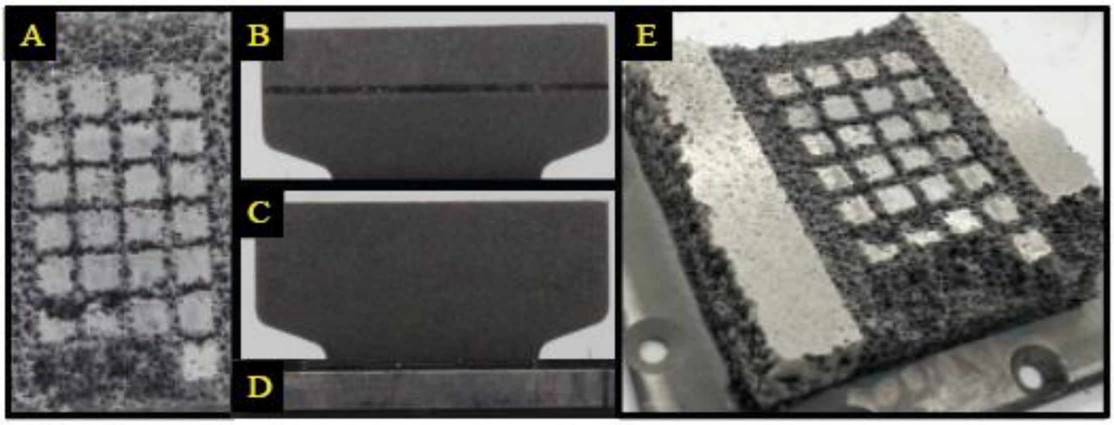

Figure 88. Type C at 1500 µm incursion depth and fast incursion rate: A) Rub Surface, B) Leading Blade Edge, C) Trailing Blade Edge, D) Blade Tip, E) Rub Surface

The abradable shows some missing tiles from the bottom of the substrate, this was already the case pre-rub where they were removed along with the spraying mask to reveal the surface pattern. It can be noted that the surface in 88E shows that besides this little to no material loss from the substrate surface and near subsurface which implies that the foam and cap combination is compliant. Where there is abradable cap and foam compliance this is likely to lead to a large amount of compaction with no material loss where the energy has allowed local fracture along the fault lines that were introduced for that specific purpose. Similarly to previous tests the blade shows no signs of material adhesion or damage along the tip surface.

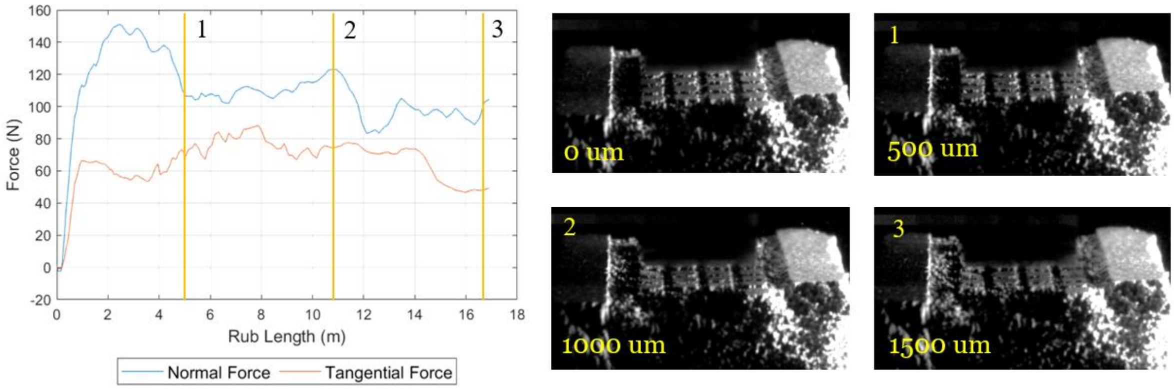

Figure 89. Progression of rub at 1500 µm depth for Type C at 2 µm/pass showing the 3 stages of rub representative of the different incursion depths: 500 µm, 1000 µm, 1500 µm

From the force data in Figure 89 it should be noted that in comparison to Type A & B the forces are significantly lower, this reduction in force is likely to lead to less substrate damage. Just comparing the rub surfaces for all three types tested so far at the incursion depth of 1500 μm it should be noted that the smaller the contact area the smaller the force. As the tiles become smaller it can be expected that the cap and foam hybrid regions are more durable which suggests a lower global stiffness which in turn lead to a reduction in the forces during the rub event. A consistent compaction and foam compliance can be seen in the rub progression (Figure 89) at every stage of rub.

Type D incorporates a pattern designed for the purpose of releasing energy efficiently through every pass of the blade, the arrows allow concentrated energy release through the edges as it rubs in through the tips. Similarly fault lines are added to further investigate whether the collapse and fracture for eventual energy release and dissipation can be controlled.

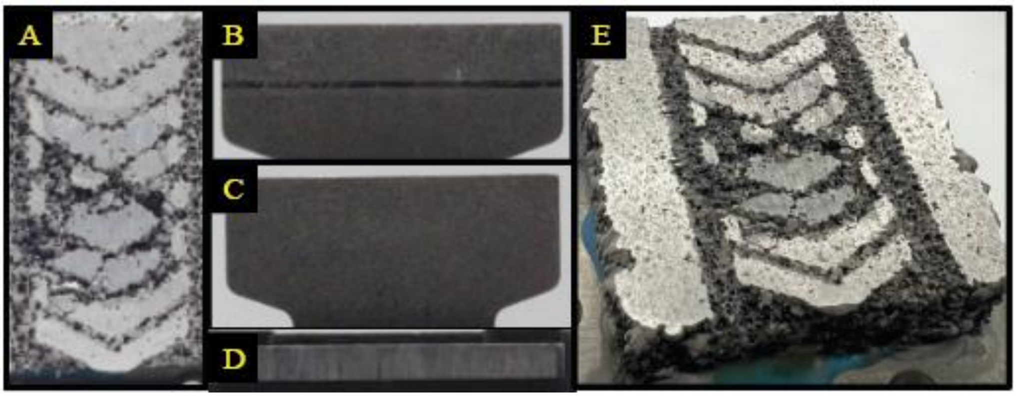

Figure 90. Type D at 1500 μm incursion depth and fast incursion rate: A) Rub Surface, B) Leading Blade Edge, C) Trailing Blade Edge, D) Blade Tip, E) Rub Surface

The abradable surface shows fracture in the centre position of rub, additionally edge tearing is evident in 90E. The local fracture in combination with the fracture events within the centre of rub is likely to have led to material loss and subsurface damage. The blade images show no signs of surface damage on the contact tip, furthermore there are no signs of material adhesion onto the tip surface. It is interesting to consider that fracture has only occurred within the central area of rub whereas the leading an trailing edges of rub have still managed to survive the rub event.

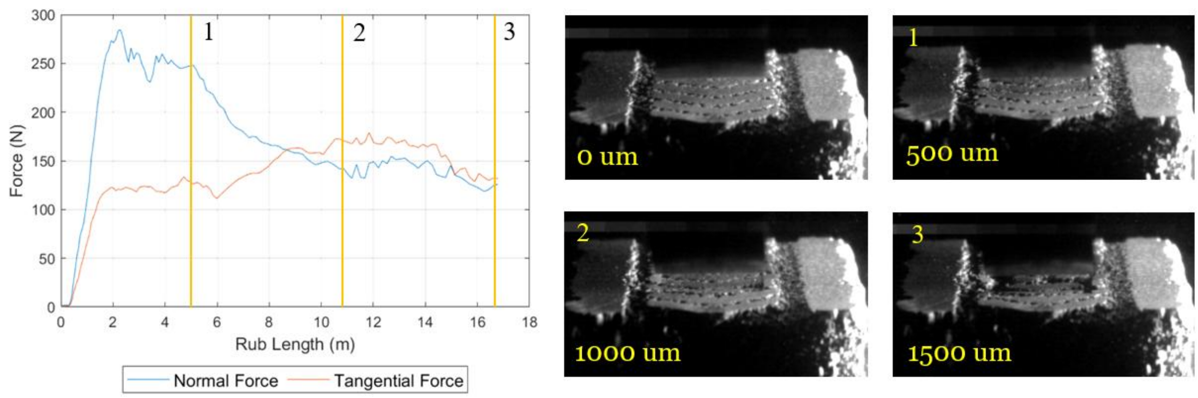

Figure 91. Progression of rub at 1500 μm depth for Type D at 2 μm/pass showing the 3 stages of rub representative of the different incursion depths: 500 μm, 1000 μm, 1500 μm

The initial normal force peak suggests an initial stage of compaction where the foam and cap combination are in compliance which is confirmed from the high speed capture in Figure 91, this initial compliance allows the substrate to deform to conform in correlation with the blade path. It is interesting to see a tangential force progressive increase through the rub test, from the way the fault lines are arranged it is likely that as the abradable has reached the maximum amount of compaction. Where the cap and foam combination has reached the compaction limit a rise in tangential force is expected as there will be an increase in surface resistance to rub. During the mid to late stages of rub it can be seen that the material surface begins to break and crumble damaging the material subsurface and causing eventual delamination of several areas.

From these 4 tests at the fast incursion rate it is seen that local areas of structural weakness incorporated into the design of the surface coating cap allows the location of fractures to be controlled across fault lines in the near surface and subsurface of the substrate. The two fault lines across the sides parallel to the direction of rub are to help eliminate edge tearing, generally seen across all the samples edge tearing is still a mechanism that exists and has not been fully eliminated.

Table 10. Fast incursion rate summary to showing how each design performed against certain criteria showcasing post-test rub surfaces

Legend
- 🟢 Well Cut
- 🟡 Adhesive Transfer
- 🟠 Little Compaction
- 🔵 Large Compaction
- 🟣 Edge Tearing
- ⚫ Minor Rupture
- 🔴 Major Rupture

Mesh Patterned Foam		
Foam Type	**Incursion Rate**	**Abradable Surface**
	2 µm/pass	
A	🟡 🟣 🔵 ⚫	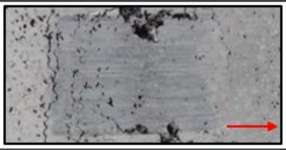
B	🟢 🟣 ⚫	
C	🟢 🟣 🔵 ⚫	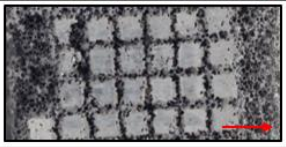
D	🟠 🟣 🔴	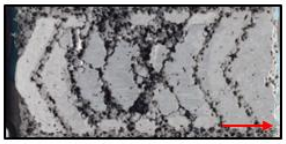

Table 10 shows a summary of how well these patterned foams performed against the aforementioned criteria as well as a comparison of rub surfaces post-test for each design. Type C has outperformed the others by retaining the near surface and subsurface coating material whilst also eliminating edge tearing from occurring during the test. Metallic foam substrate abradables are typically assessed on how well the abradable is cut, amount of compaction, extent to which edge tearing exists as well as quantity of rupture in the abradable rub surface. Previous tests on honeycomb structures similarly show some surface compaction, the low rub forces correlate with this study where the abradable manages to distribute the load and comply to the rub [31].

8.2.2 Tests at 1 µm/pass

As seen from Chapter 7 and the capped foam abradable substrates inability to actuate a compaction mechanism at the lower incursion rates of 0.2 and 0.02 µm/pass. From the tests performed at 2 µm/pass it can be identified that the best performing substrates were the tile patterns in Type B and C. As these were the best performing they have been taken to be tested at 1 μm/pass in order to check whether at the slightly slower incursion rate the cap and foam compliance and actuation of compaction mechanisms is possible.

Figure 92 shows the results of Type B at an incursion rate of 1 μm/pass, its can clearly be seen from the rub surface in 92A that some rupture event has occurred during rub leading to the subsurface fracture and material loss losing some of the surface tile structures.

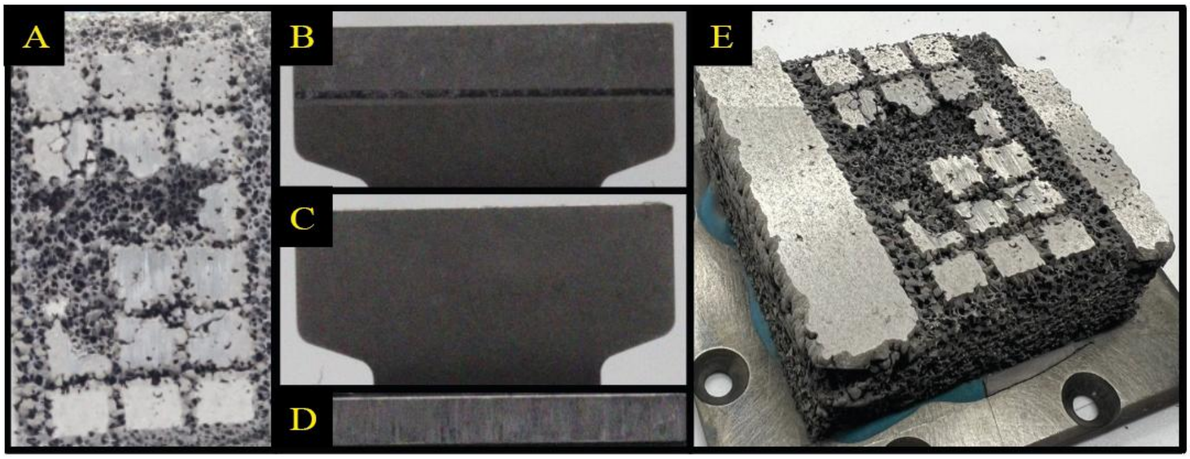

Figure 92. Type B at 1500 μm incursion depth and 1 μm/pass incursion rate: A) Rub Surface, B) Leading Blade Edge, C) Trailing Blade Edge, D) Blade Tip, E) Rub Surface

From the rub surface (92A&E) where the surface has been retained, some compliance and compaction can be seen to have occurred during the test. Whether or not this is compaction or cutting cannot yet be determined. At the lower incursion rates it is expected to generally see more subtle damages to the blade however Figure 92B shows that the blade images have little to no adhesion or wear to imply that the cap and foam combination has been compliant to prevent this.

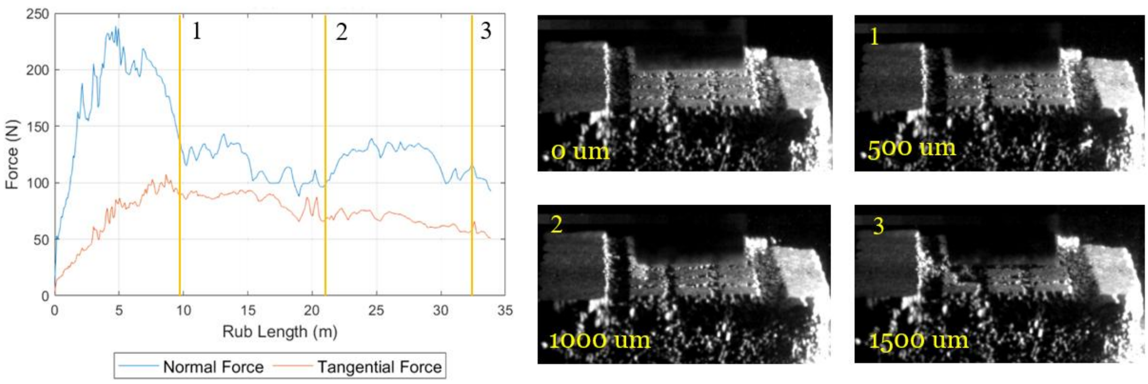

Figure 93. Progression of rub at 1500 μm depth for Type B at 1 μm/pass showing the 3 stages of rub representative of the different incursion depths: 500 μm, 1000 μm, 1500 μm

The force measurements recorded in Figure 93 show that there is an initial force peak at the early stages of the rub. This normal force peaks at a maximum just below 250 N, whereas at the faster incursion rate this normal force peaks above 250 N, it is expected that at a slower incursion rate the normal force will be smaller however in terms of behaviour the rub progression shows initial compaction stages where the rub surface seems to deform.

Type C tested at the fast incursion rate seems to have performed the best and so should show promise when testing at a slightly reduced incursion rate of 1 μm/pass. Figure 94 shows the results for Type C where it shows that the rub surface has deformed compacting the subsurface metallic ligands however there is also some material loss.

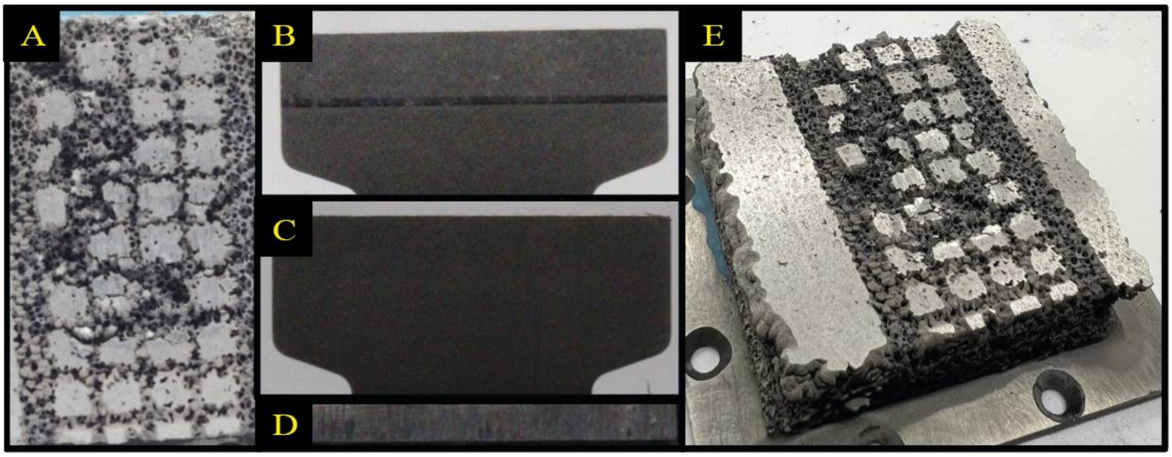

Figure 94. Type C at 1500 μm incursion depth and 1 μm/pass incursion rate: A) Rub Surface, B) Leading Blade Edge, C) Trailing Blade Edge, D) Blade Tip, E) Rub Surface

The abradable surface in 94A shows three regions where the cap and foam combination has failed and crumbled. The foam shows a general compliance where the bulk rub surface has compacted whereas localities of fracture occur. At the reduced incursion rate there are more passes of the blade and it can be likely that some low cycle fatigue has caused underlying ligament structures to fail and break releasing the material as large debris fragments.

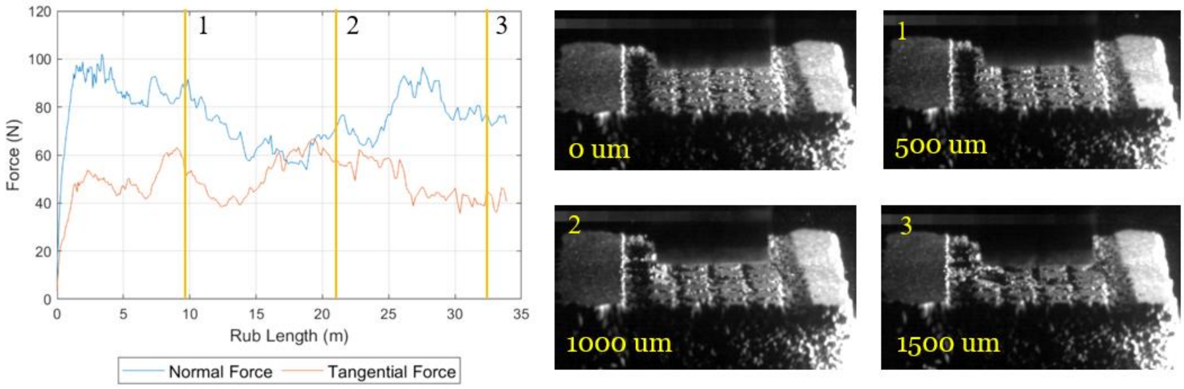

Figure 95. Progression of rub at 1500 μm depth for Type C at 1 μm/pass showing the 3 stages of rub representative of the different incursion depths: 500 μm, 1000 μm, 1500 μm

From the forces in combination with post-test surface images, it is clear that compaction of the foam and cap can be achieved at lower forces. The rub progression clearly shows initial stages of compaction where deformation of the abradable substrate seems apparent. In this instance there is still a normal force peak which is usually representative of this mechanism however significantly lower than at the higher incursion rate. Where areas fracture and deform an uneven rub surface can develop, through which it is likely that where the forces start to creep up in the mid to latter stages caused by this.

Table 11. Mid incursion rate of 1 µm/pass summary to showing how each design performed against certain criteria showcasing post-test rub surfaces

Legend
- 🟢 Well Cut
- 🟡 Adhesive Transfer
- 🟠 Little Compaction
- 🔵 Large Compaction
- 🟣 Edge Tearing
- ⚫ Minor Rupture
- 🔴 Major Rupture

Mesh Patterned Foam		
Foam Type	**Incursion Rate** **1 µm/pass**	**Abradable Surface**
B	🟠 🟣 🔴	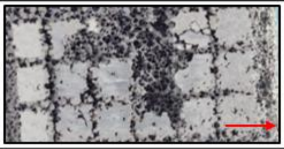
C	🟢 🟣 🟠 ⚫	

At the incursion rate of 1 µm/pass, Table 11 shows the summary where Type C has performed better than Type B. It can be seen that even though the smaller tile structure in Type C has also shown signs of material rupture due to the nature of the smaller surface area of tiles not as much material is lost as oppose to Type B where when tiles delaminate a larger surface area of the rub is also removed.

8.2.3 Tests at 0.2 µm/pass

Seen from the above tests Type C has performed the best where the surface and subsurface compliance has allowed for a compaction in combination with the absence of local fracture as well as edge tearing phenomenon with no significant loss of material previously encountered with many cap and foam combination substrates.

Figure 96 shows the results of Type C when tested at a lower incursion rate of 0.2 µm/pass, this is to see whether at the slower incursion rates where the actuation force is reduced if the foam and cap combination are still compliant to allow a compaction mechanism to occur.

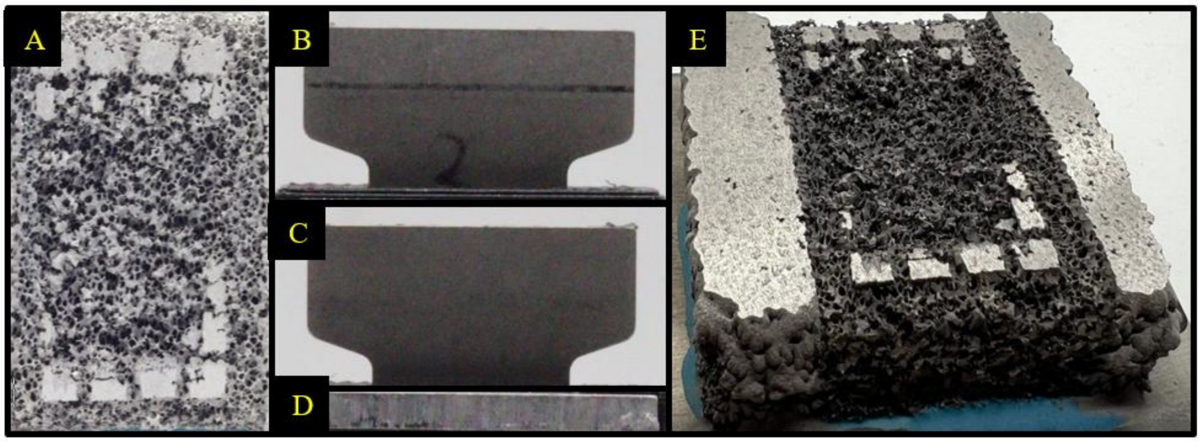

Figure 96. Type C at 0.2 µm/pass incursion rate: A) Rub Surface, B) Leading Blade Edge, C) Trailing Blade Edge, D) Blade Tip, E) Rub Surface

The result for the in Figure 96 shows the abradable cap has burst and delaminated from the underlying foam where subsurface damage has torn ligaments leading to subsequent material loss. Wherever material loss from the subsurface is seen it is likely to lead to lower normal forces and little to no deformation of the cap and foam. The force measurements in Figure 97 confirm the low normal forces generally seen with such behaviour of the abradable. Similarly to the other abradable patterned samples the blade (Figure 96D) shows no sign of wear or damage, additionally there is typically no adhesion to the blade tip surface.

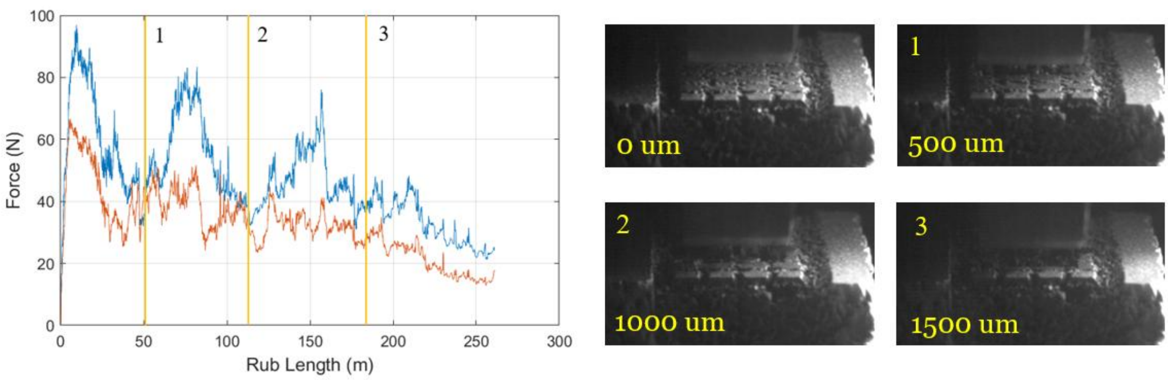

Figure 97. Progression of rub at 1500 µm depth for Type D at 2 µm/pass showing the 3 stages of rub representative of the different incursion depths: 500 µm, 1000 µm, 1500 µm

The results in Figure 97 show the rub progression, this highlights the key stages of rub to identify any key rub characteristics that occur. It should be noted that during the early stages of rub, the subsurface material as a combination of foam and cap already starts to exhibit cracking and fracture. This propagates as the depth of rub increases until the end of the test.

8.2.4 Testing Summary

It is apparent across these tests that the smaller tile samples in Type C is the most favourable to allow an excellent compaction mechanism of the foam and cap combination keeping the normal and tangential forces low even at the fast incursion rate. The larger tiles of Type B do show some good compaction mechanism where there is compliance of the foam and cap however at the slower incursion rates this seems to fail resulting in larger amounts of material loss where singular tiles are delaminated. It would seem that these may be a result of a lower fatigue life. Types A and D show early sign of edge tearing where a separation at the blade edge causes rupture events which result in localised ligand failure and ultimately material delamination.

The cap and foam combination in Type A also previously tested in Chapter 7 is commonly seen to have larger normal forces, this being said typically an initial normal force peak in the very early stages or rub occurs where a large initial bulk compaction seems to take place. Similarly to tests in Chapter 7 the locations of where failure occurs is sporadic and hard to control, it is also hard to predict the amount of surface damage that can occur between tests based upon the local fracture and failure in the material subsurface. For the reason fault lines are introduced into the rub surface coating to allow certain areas to deform and fracture whilst also allowing compaction and deformation of the cap and foam in compliance to the rub event.

Type D shows in comparison to the other patterns more surface damage and localised fracture which has led to material loss as large debris fragments which have delaminated from the rub surface. The forces however in contrast are significantly lower than those seen for Type A where the initial stages of rub also show compaction and deformation of the rub surface.

Moving on to Type B and C, both patterns worked in actuating a compaction mechanism at a reduced force. This is more so for Type C where the pattern design is similar however the tiles are smaller of a higher density in comparison to Type B. It is likely that the behaviour seen after rub events is linked to the global stiffness of the foam and cap combination. Regarding Type C the fault lines are located such that there is less bulk material and more separation between tiles which results in a lower global stiffness and more durability in the substrate surface.

The forces at the high incursion rate of 2 μm/pass confirm this where the lower global stiffness of Type C allows for a compaction mechanism at significantly lower forces with less surface and subsurface damage to the substrate. When in comparison to Type B the larger global stiffness means a higher force in the initial compaction phase as well as material loss as the test progresses.

At a reduced incursion rate of 1 μm/pass Type B and C both show signs of material compliance and compaction during the rub however there are some key differences. Similarly to the high incursion rate both show compliance and Type C is able to actuate the compaction mechanism with a reduced actuation force. With this reduction in incursion rate however, there can be seen to be some low cycle fatigue failures which arise as there is an increase in the number of contacts between abradable substrate and blade for a given incursion depth. For Type B this is more catastrophic to the surface with more subsurface and surface damage, this is likely to be a result of the higher global stiffness and larger tile sizing which means that even if small subsurface fracture occurs this will likely lead to tile delamination. Additionally, this is the case for Type C however since the tiles are smaller the surface material loss isn't as tragic.

Taking Type C forward to the lower incursion rate of 0.2 μm/pass it clearly does not actuate any compliance of the foam, from the forces in Figure 100 it looks like there is a periodic behaviour likely to be a compaction release mechanism. Surface compaction takes place however this also induces subsurface damage from the low cycle fatigue of blade to substrate contact. This is prominent from the rub progression that the subsurface damage occurs even from the initial stages of rub and is seen to rupture, as the test progresses and the rub length increases further material loss occurs with little to no compaction. Similarly with abradable capped foams at the lower incursion rates this can also be seen where there is mostly cap and subsurface ligand removal.

8.3 Discussion

The amount of compaction and compliance which takes place during the test is difficult to quantify and thus more analysis is required in order to justify whether the behaviours hypothesised in the results are actually evident to occur. The performance of these capped foam substrates can be linked to two principles which is compliance of the cap and foam combination layer as well as the edge tearing. A common technique used for analysing internal structure is sectioning, for tests at the high incursion rate of 2 µm/pass the capped foam substrates are vacuum impregnated to retain the metallic foam structure with minimal structural damage. The combination of epoxy and black dye help mask underlying layers which would be seen if a clear resin is used. The 2 µm/pass condition is used across Types A, B and C to investigate how the cutting and compaction identified from the sections is linked to compliance of the foam visually in combination with the forces.

Figure 98. Type A at the fast incursion rate of 2 µm/pass showing A) Location of section and B) Sectioned face

Figure 98 shows Type A post-test where it shows a cross section of the foam structure along the centre of rub. Similarly to previous capped foam test it can be seen from Figure 98 that the surface shows signs of compaction where the foam and cap combination deform and conform to the blade path. It is clear that there is a compaction zone in the near subsurface beneath the rub surface, comparing the cap and foam thickness combination across the entire section, visually it seems that there is little difference in thickness which implies that there is little to no cutting during the rub test.

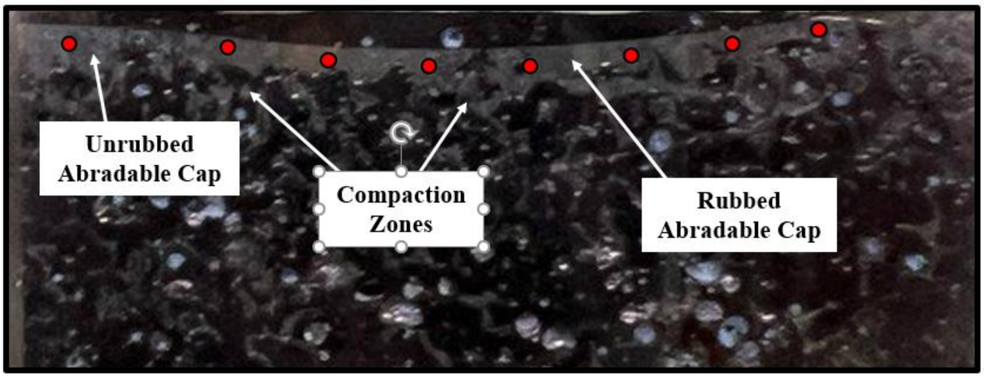

Figure 99. Thickness measurement points across the section of Type A under the fast incursion rate condition of 2 µm/pass to assess extent of cutting from the post-test structure – highlighting compaction zones, rubbed and unrubbed areas

Figure 99 shows the points at which depth measurements are taken across the cap thickness, it is seen that variations arise due to the placement of ligaments, additionally the amount of spray penetration has some inconsistencies, these inconsistencies however do not directly influence the cap measurements. On average the rub zone has a slightly smaller cap thickness where it can be seen some cutting has removed surface material, points have been measured across the rub and compared to the unrubbed regions of the sample.

Along the centre regions of rub it is measured to be 1267 µm, this is expected to be the location with the most material loss. Along other parts of the rub it is measured to be 1560 µm with a small change in thickness compared to the centre point of rub. The unrubbed section of the substrate cap measures to be on average 2010 µm across a few points, a maximum thickness difference of 743 µm and minimum thickness difference of 450 µm across the rub. This difference in thickness is a result of cutting between blade and abradable contact, where there isn't full compliance of the foam and cap substrate a compaction mechanism cannot be actuated.

Where there is less change in cap thickness along the rub, there is likely to be a compactive zone of ligands beneath the subsurface. This is where metallic ligands have fractured locally, as described previously in Chapter 7, the energy from contact is often translated through localised fracture of the subsurface ligaments to create a compliant compaction layer. Whilst a compaction mechanism here has been ineffective to eliminate cutting effects, it should be highlighted that the discontinuity (admittedly not perfectly aligned to the blade) has reduced edge strain and hence rupture of the surface.

Additionally, moving onto Type B with the larger tile tracks, the results show that deformation of the surface occurs however how much compliance can be achieved through sectioning. Furthermore, once again at the edge discontinuity has reduced the extent to which rupture occurs, this is indeed the case for all pattern types. Figure 100 shows the cross section along the rub showing the internal structure of the abradable post-test where 100A shows the positioning of the cut along the rub corresponding to 100B showing the sectioned surface.

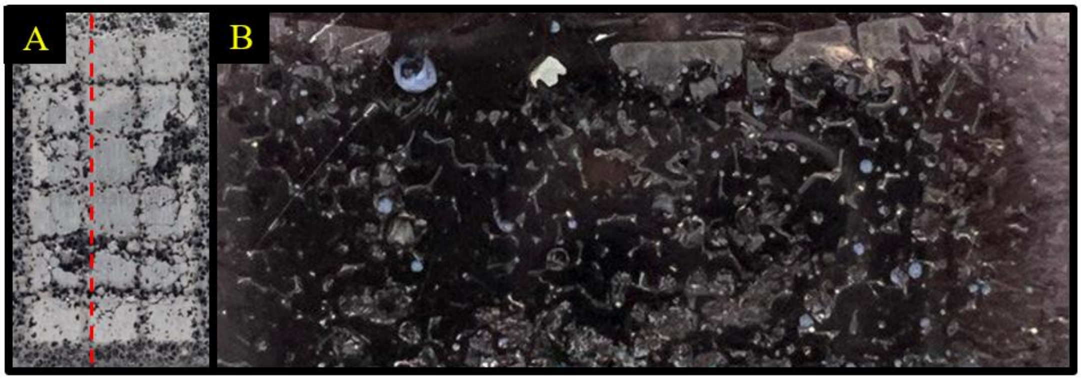

Figure 100. Type B at the fast incursion rate of 2 µm/pass showing A) Location of section and B) Sectioned face

In this instance it is also clear that the surface shows compliance where deformation has occurred, visibly the difference in cap thickness along the rub section seems minimal which is likely to suggest less cutting of the abradable surface and more compliance and compaction of the foam and cap combination. The compaction zones along the near subsurface also reinforce the point that there is more compliance, in addition forces are significantly smaller in comparison with Type A where there are no fault lines within the rub surface. The tile structures in the cap surface shows separation between tiles, this however does not to compromise the compaction mechanism but determine how compliance is achieved.

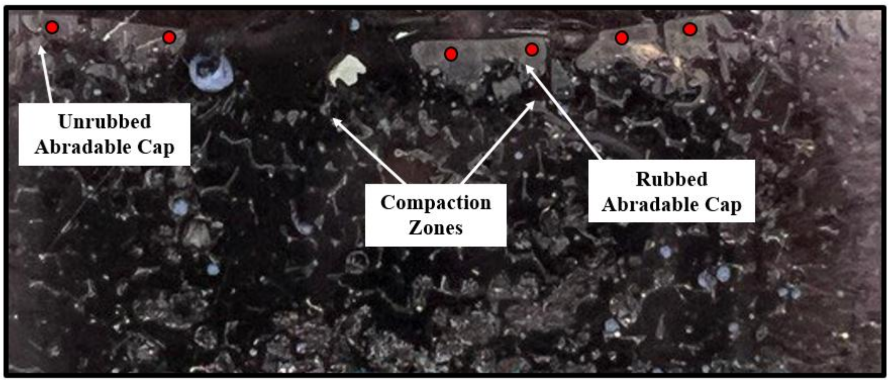

Figure 101. Thickness measurement points across the section of Type B under the fast incursion rate condition of 2 µm/pass to assess extent of cutting from the post-test structure – highlighting compaction zones, rubbed and unrubbed areas

Measuring cap thickness shows that there is little difference between the rubbed and unrubbed surface, the thickness measured from the tiles is average at 1855 µm in comparison to 2096 µm where the sample is hasn't rubbed as a control.

In comparison to Type A there is a significant difference in measured cap thickness where Type B shows a smaller change in thickness to suggest less cutting. The cross section in B shows larger compactive zones in the near subsurface, this in combination with a smaller change in cap thickness indicates more abradable compliance and subsequently less cutting between blade and abradable.

Finally, Type C which has performed the best is sectioned to further analyse the cap thickness of the abradable substrate. Type C showed the most compliance globally from the entire rub surface, the low forces in combination with compaction of the abradable is likely to show that there will be small differences in the cap thickness even at the deepest part of rub. Figure 102B shows the section where visually there is little difference in overall thickness of abradable substrate cap.

Figure 102. Type C at the fast incursion rate of 2 µm/pass showing A) Location of section and B) Sectioned face

For the smaller tile pattern in Type C it can clearly be depicted from Figure 102B that the surface has compacted in compliance with contact with the blade. Compaction zones seen from the section (102B) are located directly beneath the tile separations where localised regions underneath the subsurface are able to fracture and compact. In this instance at the leading end of the rub surface there is a dense compaction zone which is not seen at the trailing end of the rub surface, both shown in Figure 103.

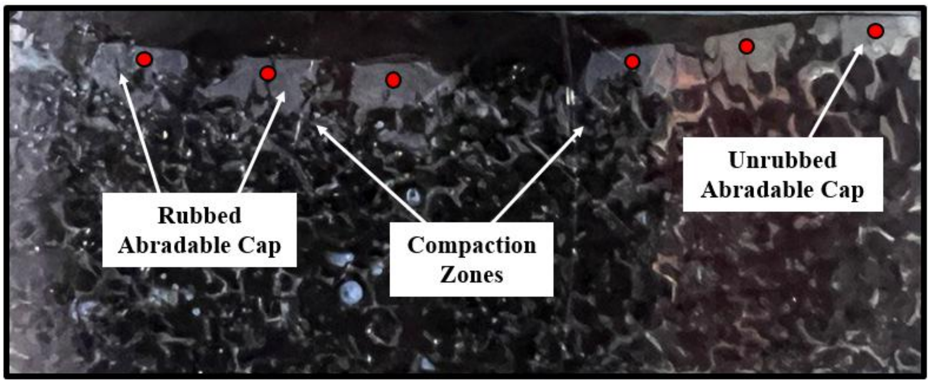

Figure 103. Thickness measurement points across the section of Type B under the fast incursion rate condition of 2 µm/pass to assess extent of cutting from the post-test structure – highlighting compaction zones, rubbed and unrubbed areas

Measuring the average cap thickness across a few positions of the rub surface, it shows that at the deepest part of rub it measures 1953 μm in comparison to 2057 μm which is measured at a non-rubbed area, similarly there is minimal difference between the two. As predicted the lower forces and compliance of the surface and subsurface of the abradable is likely to show very small amounts of cutting during rub tests, this is reinforced by the dissimilar cap thickness measured from the locations in Figure 103.

Table 12. Comparison of cap thickness across Types A, B and C showing rubbed and unrubbed measurements

Mesh Type	Blade Delta (μm)	Depth of Rub (μm)	Compaction (%)	Cap Thickness Measurement (μm)		
				Rubbed	Unrubbed	Δ
Type A	0.1	1000	25.7	1267	2010	743
Type B	0.1	1000	75.9	1855	2096	241
Type C	0.1	1000	89.6	1953	2057	104

It should be highlighted that a more compliant cap leads to more compaction, Table 12 highlights this point where it shows the change in cap thickness between the three sample types sectioned and it indicates that Type C which shows the most compliance has the smallest change in thickness to suggest the most compaction. Furthermore, from the sectioned images it is clear that for abradable Type C underneath the cap in the near subsurface the compactive zones are larger with more ligand fracture and overall compliance. Conversely abradable Type A has the least compaction zones with less localised ligand fracture in the near subsurface, subsequently this test also showed the least compliance with more surface cutting. The degree to which compaction occurs is further highlighted, more fault lines within the surface will result in more surface compaction and less material loss from the rub. Type A with two fault lines along the blade edges shows the abradable is susceptible to more material loss and less compaction.

Seen in previous chapters, failure occurs in the form of fracture and material loss where the sample is too globally stiff since the activation energy input for a given test reduces with a lower incursion rate. The more compliant abradables survive the lower incursion rates, it is evident from these tests and previous tests in Chapter 7 that the lower incursion rates of 0.2 μm/pass have failed with catastrophic damage to the cap and foam substrate combination.

These tests show however that an edge discontinuity introduced significantly reduces rupture at these locations which showed highly problematic in the previous chapters.

8.4 Conclusion

From a comparison between the measured cap thicknesses from sectioned samples for Types A, B and C, it shows that the amount of cutting during the rub events can be related to the surface pattern. Type A shows a smaller measured thickness where there are no tile or patterns along the rub surface, as tile patterns are introduced with fault lines incorporated into the surface cap structure in Type B the compliance of the foam allows for less cutting with a force reduction which leads to more compaction in the near subsurface. As further highlighted from Type C, the rub surface shows an even smaller change in cap thickness even considering the deepest point of rub at the centre position of the section. This in combination with the significantly lower forces reinforces the point that with a reduction in tile size and increase in tile quantity over the same rub area suggests additional abradable substrate compliance with even less cutting.

Chapter 9

Conclusion and Future Work

9.1 Open Cell Foams

- Localised ligand fracture and breakage in the surface causes significant amounts of damage to both the abradable and blade.
- Failure occurs earlier in the test for the larger nominal pore size open cell foams, this causes more damage to the blade and abradable.

9.2 Filled Metallic Foams

- Resin filled polyester foams cut extremely well with the main limitation of operating temperature which can prove ineffective for compressor stage sealing
- At the lower incursion rate of 0.02 μm/pass ligand pull out is phenomenon commonly seen where the metal ligaments within the foam and filler substrate are removed during the test, this leaves open pores within the rub surface.
- At the higher incursion rate of 2 μm/pass the cutting performance of the filled foams is excellent, the mechanism actuated is load transfer to allow energy shock absorption additionally providing outstanding energy dissipation.
- The performance of filled foams is dependent upon the surface strain rate, main factors affect the strain rate include incursion rate, filler density and thermal exposure. Increased thermal exposure is likely to increase the surface strain rate, whereas, a slower incursion rate and smaller filler density increase the surface strain rate.
- Filler density of resin is linked to the glass fibre quantity, 20% glass fibre quantity cuts better in comparison to the 10% glass fibre. After thermal exposure, the polyester phase of the resin degrades – the glass fibre proportion increases the surface hardness and brittle attributes leading to better cutting but also thermal smearing at the elevated temperature.

9.3 Capped Metallic Foams

- Initial tests with full cap foams show that the cap and metallic foam structure act as two different bodies, energy from the cap is not able to dissipate through the foam and thus is stored until the cap has reached its limit. This leads to a result where the cap explodes and bursts causing catastrophic damage to the abradable.
- Samples are ground back to a hybrid layer where the metallic foam ligands are exposed on the surface held in place by the Metco 320 cap, tests show that a compaction mechanism occurs however this is only the case at the high incursion rates.
- At the lower incursion rates a compaction mechanism isn’t present and there is no compliance by the abradable cap and foam combination thus leading to failure in the surface and near subsurface where localised ligands fracture and result in surface delamination.
- Compliance of the foam and cap is often seen to occur at the higher incursion rates. The larger impact forces at the higher incursion rates allows for more energy per strike to activate material compaction and overall more compliance of the abradable.
- Smaller pore size performs more poorly in comparison to a coarser foam size, the smaller ligands upon impact tend to fracture and deform more easily leading to a fracture and delamination mechanism.
- Additionally edge tearing plays a huge factor in how the abradable substrate performs, where there is a separation from the compliance of the sample to where it is uncut a fault line starts to form where localised fracture of ligands occurs and eventual compaction and compliance removes large quantities of material. More evident when there is a harder cap surface.
- The softer cap allows for more surface compliance which is supported by the difference in cap material lost during the rub event. Additionally visually the harder cap shows a thinner top cap post rub where more cutting and less compliance is achieved.

9.4 Patterned Capped Metallic Foams

- Mesh patterns are masked over metallic foam substrates to achieve areas of less in fill and coating upon the spraying process. Fault lines are introduced to allow more compliance of the cap and foam combination these are to control the fracture locations and improve compliance of the foam and cap.

- Tile structures are excellent at showing compliance where the fracture and compaction is controlled and located where the fault lines exist. This allows for actuation of a compaction mechanism and better compliance of the foam. The smaller tile pattern shows more compaction zones and thus more compliance of the rub surface and near subsurface.
- Fracture of metal ligands during testing is imminent however the location can be controlled through the fault lines. Where edge tearing occurs the discontinuity along the blade path helps to eliminate the failure along these points previously seen to actuate more material loss during rub.
- The activation energy is reduced and the samples can show compliance at the faster and mid incursion rates however when moving towards the lower incursion rate of 0.2 μm/pass the substrate shows similar behaviour to that seen in the previous chapter where compliance is no longer achieved and local fracture occurs upon blade contact propagating from the initial stages of rub.

9.5 Future Work

- Foams performance is linked to the global stiffness of the metallic foam substrate, it should allow for some ductile behaviour where compaction can occur and a compliance is necessary to create a necessary cut. Additionally more testing should be carried out surrounding the metallic foam deformation properties and how global stiffness can be altered.
- In order for compliance of the rub to be achieved for patterned capped metallic foams tiles have shown promise where compliance can be achieved with little to no cutting, challenges arise where the slower incursion rates cannot be achieved. There is further work surrounding the tile size where a limitation lies within the spraying process and the resolution and ability to spray to such precision.

References

[1] B. Lattime, "Turbine Current Engine Clearance Control Systems : Practices and Future Directions," no. September, 2002.

[2] L. Pallett, G. Pattinson, and M. Hancock, "Requirements for Future Compressor Lining Material," vol. 5, 2020.

[3] "Investigation And Characterisation Of The Wear. Nicola Fois PhD Thesis"

[4] M. Watson and M. Marshall, "Wear mechanisms at the blade tip seal interface," *Wear*, vol. 404–405, no. June 2017, pp. 176–193, 2018, doi: 10.1016/j.wear.2018.03.009.

[5] R. E. Johnston and W. J. Evans, "Freestanding abradable coating manufacture and tensile test development," *Surf. Coatings Technol.*, vol. 202, no. 4–7, pp. 725–729, 2007, doi: 10.1016/j.surfcoat.2007.05.082.

[6] S. Shabbir and S. Garvey, "Aerospace Sealing Technology for Maintenance , Repair and Overhaul of engines : a review," no. August 2019, 2020.

[7] H. Xuan, N. Zhang, B. Lu, L. Cheng, And W. Hong, "Investigation of high-speed abrasion behavior of an abradable seal rubber in aero-engine fan application," *Chinese J. Aeronaut.*, vol. 30, no. 4, pp. 1615–1623, 2017, doi: 10.1016/j.cja.2017.02.019.

[8] R. E. Chupp, R. C. Hendricks, S. B. Lattime, and B. M. Steinetz, "Sealing in turbomachinery," *J. Propuls. Power*, vol. 22, no. 2, pp. 313–349, 2006, doi: 10.2514/1.17778.

[9] R. E. Chupp, R. C. Hendricks, S. B. Lattime, and B. M. Steinetz, "Sealing in turbomachinery," *J. Propuls. Power*, vol. 22, no. 2, pp. 313–349, 2006, doi: 10.2514/1.17778.

[10] X. Yan, X. Dai, K. Zhang, J. Li, and K. He, "Effect of teeth bending and mushrooming damages on leakage performance of a labyrinth seal," *J. Mech. Sci. Technol.*, vol. 32, no. 10, pp. 4697–4709, 2018, doi: 10.1007/s12206-018-0917-y.

[11] S. B. Lattime and B. M. Steinetz, "Turbine engine clearance control systems: Current practices and future directions," *38th AIAA/ASME/SAE/ASEE Jt. Propuls. Conf. Exhib.*, no. September 2002, 2002, doi: 10.2514/6.2002-3790.

[12] E. Scrinzi, I. Giovannetti, N. Sheng, and L. Leblanc, "Tbts2013-2065 Development of New Abradable / Abrasive Sealing Systems for," pp. 1–10, 2018.

[13] S. Wilson, "Overview of Sulzer Metco Compressor and Turbine Abradable Technology," 2011.

[14] M. W. Wiseman, "An Investigation of Life Extending Control Techniques for Gas Turbine Engines," *Proc. Am. Control Conf.*, 2001.

[15] N. Fois, M. Watson, and M. B. Marshall, "The influence of material properties on the wear of abradable materials," *Proc. Inst. Mech. Eng. Part J J. Eng. Tribol.*, vol. 231, no. 2, pp. 240–253, 2017, doi: 10.1177/1350650116649528.

[16] X. Ma and A. Matthews, "Evaluation of abradable seal coating mechanical properties," *WEA*, vol. 267, no. 9–10, pp. 1501–1510, 2009, doi: 10.1016/j.wear.2009.03.044.

[17] D. Sporer and A. Refke, "Processing and Properties of Advanced Ceramic Abradable Coatings," *Solutions*, pp. 495–500, 2007.

[18] E. Novinski, J. Harrington, J. Klein, E. Novinski, J. Harrington, and J. K. Modified, "Modified zirconia abradable seal coating for high temperature gas turbine applications To cite this version : HAL Id : hal-01553705," pp. 0–9, 2017.

[19] F. Scientific *et al.*, "Final Scientific/Technical Report Reporting Period Start Date: October 1," 2019.

[20] H. I. Faraoun *et al.*, "Improvement of thermally sprayed abradable coating by microstructure control," *Surf. Coatings Technol.*, vol. 201, no. 6, pp. 2303–2312, 2006, doi: 10.1016/j.surfcoat.2006.03.047.

[21] X. Zhao, C. Li, H. Jiang, S. Li, and X. Han, "Mechanistic Study on the Influence of Hydrogen Fuel in High-Velocity Oxygen-Fuel (HVOF) Thermal Spraying Process," *Jom*, vol. 76, no. 1, pp. 57–70, 2024, doi: 10.1007/s11837-023-06254-y.

[22] S. Wilson, "Thermally sprayed abradable coating technology for sealing in gas turbines," *Futur. gas turbine Technol. 6th Int. Conf.*, pp. 1–9, 2012.

[23] C. P. Bergmann and S. Alessioomalandruccolo, *Topics in Mining, Metallurgy and Materials Engineering Series Editor: Aerospace Alloys*. .
[24] R. Rajendran, “Gas turbine coatings - An overview,” *Eng. Fail. Anal.*, vol. 26, pp. 355–369, 2012, doi: 10.1016/j.engfailanal.2012.07.007.
[25] K. Oh, E. Lee, J. S. Bae, M. Jang, and R. Poss, “Large scale production and applications of alloy metal foam,” pp. 1–6, 2010.
[26] B. G. Walther *et al.*, “REVIEWS A New Class of High Temperature and Corrosion Resistant Nickel-Based Open-Cell Foams **,” no. 9, pp. 803–811, 2008, doi: 10.1002/adem.200800088.
[27] B. Zhang and M. Marshall, “Investigating material removal mechanism of Al-Si base abradable coating in labyrinth seal system,” *Wear*, vol. 426–427, no. January, pp. 239–249, 2019, doi: 10.1016/j.wear.2019.01.034.
[28] M. Watson and M. Marshall, “Wear mechanisms at the blade tip seal interface,” *Wear*, vol. 404–405, no. February, pp. 176–193, 2018, doi: 10.1016/j.wear.2018.03.009.
[29] N. Fois, J. Stringer, and M. B. Marshall, “Adhesive transfer in aero-engine abradable linings contact,” *Wear*, vol. 304, no. 1–2, pp. 202–210, 2013, doi: 10.1016/j.wear.2013.04.033.
[30] E. Rahimov, M. Watson, A. Hadjisoteriou, and M. Marshall, “Investigation of wear mechanisms in AlSi-polyester abradable - Ti(6Al4V) blade contacts using stroboscopic imaging,” *Wear*, vol. 494–495, no. December 2021, p. 204207, 2022, doi: 10.1016/j.wear.2021.204207.
[31] B. Zhang and M. Marshall, “Investigating the application of a honeycomb abradable lining in the turbine stage of an aero-engine,” *Tribol. Int.*, vol. 125, no. April, pp. 66–74, 2018, doi: 10.1016/j.triboint.2018.04.013.
[32] N. McCormick and J. Lord, “Digital image correlation,” *Mater. Today*, vol. 13, no. 12, pp. 52–54, 2010, doi: 10.1016/S1369-7021(10)70235-2.
[33] D. P. Mondal, M. D. Goel, and S. Das, “Effect of strain rate and relative density on compressive deformation behaviour of closed cell aluminum – fly ash composite foam,” *Mater. Des.*, vol. 30, no. 4, pp. 1268–1274, 2009, doi: 10.1016/j.matdes.2008.06.059.
[34] Pıhtılı Hasim and Tosun Nihat, “Investigation of the wear behaviour of a glass-fiber-reinforced composite and plain polyester resin,” *Compos. Sci. Technol.*, vol. 62, pp. 367–370, 2002.
[35] M. S. EL-Wazery, M. I. EL-Elamy, and S. H. Zoalfakar, “Mechanical properties of glass fiber reinforced polyester composites,” *Int. J. Appl. Sci. Eng.*, vol. 14, no. 3, pp. 121–131, 2017, doi: 10.6703/IJASE.2017.14(3).121.
[36] B. Zhang and M. Marshall, “Investigating material removal mechanism of Al-Si base abradable coating in labyrinth seal system,” *Wear*, vol. 426–427, no. December 2018, pp. 239–249, 2019, doi: 10.1016/j.wear.2019.01.034.
[37] A. Avci, H. Arikan, and A. Akdemir, “Fracture behavior of glass fiber reinforced polymer composite,” *Cem. Concr. Res.*, vol. 34, no. 3, pp. 429–434, 2004, doi: 10.1016/j.cemconres.2003.08.027.
[38] X. Ramis and J. M. Salla, “Time-temperature transformation (TTT) cure diagram of an unsaturated polyester resin,” *J. Polym. Sci. Part B Polym. Phys.*, vol. 35, no. 2, pp. 371–388, 1997, doi: 10.1002/(SICI)1099-0488(19970130)35:2<371::AID-POLB13>3.0.CO;2-F.
[39] K. Viswanathan and S. Chandrasekar, “Fifty years of Schallamach waves: from rubber friction to nanoscale fracture,” *Philos. Trans. R. Soc. A Math. Phys. Eng. Sci.*, vol. 380, no. 2232, 2022, doi: 10.1098/rsta.2021.0339.
[40] I. Mouallif *et al.*, “Degradation of dynamic mechanical properties of glass fiber reinforced polyester composite pipes after immersion in various temperatures,” *J. Compos. Mater.*, vol. 48, no. 24, pp. 3025–3034, 2014, doi: 10.1177/0021998313504605.
[41] S. Belaid, S. F. Chabira, P. Balland, M. Sebaa, and S. Belhouideg, “Thermal aging effect on the mechanical properties of polyester fiberglass composites,” *J. Mater. Environ. Sci.*, vol. 6, no. 10, pp. 2795–2803, 2015.
[42] L. B. E. N. Ayed *et al.*, “Science Arts & Métiers (SAM) Thermal oxidation of vinyl ester and unsaturated polyester resins,” vol. 62, pp. 75–86, 2014.
[43] M. Vesenjak, L. Krstulović-Opara, Z. Ren, A. Öchsner, and Ž. Domazet, “Experimental study of open-cell cellular structures with elastic filler material,” *Exp. Mech.*, vol. 49, no. 4, pp. 501–509, 2009, doi: 10.1007/s11340-008-9183-8.

[44] H. Pihtili and N. Tosun, "Investigation of the wear behaviour of a glass-fibre-reinforced composite and plain polyester resin," *Compos. Sci. Technol.*, vol. 62, no. 3, pp. 367–370, 2002, doi: 10.1016/S0266-3538(01)00196-8.

[45] Y. Q. Tong, L. Chen, and G. J. Yang, "Excellently abradable seal coating with spherical closed-pore for next-generation aero-engine application," *Mater. Lett.*, vol. 307, no. August 2021, p. 131024, 2022, doi: 10.1016/j.matlet.2021.131024.

[46] M. O. Borel, A. R. Nicoll, H. W. Schläpfer, and R. K. Schmid, "The wear mechanisms occurring in abradable seals of gas turbines," *Surf. Coatings Technol.*, vol. 39–40, no. C, pp. 117–126, 1989, doi: 10.1016/0257-8972(89)90046-7.

[47] A. Liu, M. Marshall, E. Rahimov, and J. Panizo, "Investigation of wear mechanics and behaviour of NiCr metallic foam abradables," *Proc. Inst. Mech. Eng. Part C J. Mech. Eng. Sci.*, vol. 236, no. 9, pp. 4962–4972, 2022, doi: 10.1177/09544062211055341.

[48] M. B. Tischler, T. Berger, C. M. Ivler, M. H. Mansur, K. K. Cheung, and J. Y. Soong, *Aircraft Engine Controls: Design, System Analysis, and Health Monitoring*. 2017.